Bailey, D.A. (2005) The effect of damage on the energy absorption potential of composite structures. PhD thesis, University of Nottingham.

# University of Nottingham

## School of Mechanical, Materials, Manufacturing Engineering and Management

*The Effect of Damage on the Energy Absorption Potential of Composite Structures*

**D.A.Bailey**

*B.Eng(Hons)*

Thesis submitted to the University of Nottingham
for the degree of Doctor of Philosophy

June 2005

## Abstract

This thesis describes work undertaken to investigate the effects of damage on the energy absorption potential of composite tubes. Tubes of various geometries and manufactured from either continuous filament random mat (CoFRM) or glass braid and polyester resin were subjected to various types of damage before testing. Damage types consisted of drilled holes, to simulate the use of drilling components for the need of assembly, impacts, to simulate damage that may occur through tool drops or items being kicked up during use and PET inserts to simulate delamination.

Large glass CoFRM/polyester tubes with an outer diameter of 89.1mm and varying wall thicknesses were crushed quasi-statically at a speed of 5mm/min. Small CoFRM and braided glass/polyester tubes with an outer diameter of 38.1mm and a 2mm wall thickness were tested quasi statically and dynamically at a speed of 5m/s. Tubes were tested undamaged and containing various sizes of holes, simulated delamination and impacts. Specific energy absorptions (SEA) and failure modes were compared.

Threshold values of damage size have been found for each tube and test type, above which unstable failures and subsequent unpredictable reductions in energy absorptions occur. The small CoFRM tubes showed a decrease in SEA as the test rate increased and this was attributed to the rate dependency of the resin, causing greater fragmentation allowing fibres to bend more easily and without fracturing. The braided small tubes showed an increase in SEA as the test rate increased due to a change in the mode of failure attributed to a higher compressive strength at the increased rate.

Relatively small hole sizes and impacts, of 5mm and 1.5J-3J, were seen to reduce the energy absorption of the materials tested at quasi-static test speeds. However, an increase in damage tolerance was identified as test rate increased and this was attributed to an increase in compressive strength and fracture toughness, and reduction in crush load, as the speed of test increased.

# Acknowledgements

The author would like to thank:

- His supervisor, Dr N.A.Warrior for his guidance and support throughout the course of this research and Dr G. Smith for her help during the first year of the project.
- The USCAR and the University of Nottingham for jointly funding this project.
- The School of Mechanical, Materials and Manufacturing Engineering for the use of the Faculty Workshop and other departmental facilities.
- The help and support given by the technical staff at the university, especially Roger Smith, Paul Johns, Dave Smith, Geoff Tomlinson, Ray Pickard and Tony Higgins.
- Richard Fernie and Mike Duckett for their assistance in the development and implementation of the high-speed tensile test rig.
- The rest of the Nottingham Composites Group, in particular Drs. Chris Curtis, Nuno Lourenço, Brendon Weager, Mike Ribeaux and Tom Turner, for their help and assistance.

A special thanks to my parents, Peter and Carole, my brother Paul and all my friends for their love, support and encouragement throughout my time at the University of Nottingham. I couldn't have done it without them.

*Contents*

# Glossary

| | |
|---|---|
| AS4 | A continuous carbon fibre roving manufactured by Hexcel Fibers (see www.hexcelfibers.com for data sheet). |
| Anisotropic | Having properties which vary with direction within a material. |
| Binder | A substance which provides cohesion between fibres within a preform. |
| CAI Tests | Compression After Impact Tests |
| CoFRM | Continuous Filament Random Mat. |
| Cure | Polymerisation of a resin – changing from liquid to solid. |
| E-glass | Electrical glass, the most commonly used glass fibre. |
| Filament | A single fibre. |
| Filament Winding | An FRP manufacturing technique, involving wrapping dry or impregnated fibres around a mandrel. |
| HSS | High Speed Steel. |
| HTA | A continuous carbon fibre roving manufactured by Tenax Fibers (see www.tenax-fibers.com for data sheet). |
| IM7 | A continuous carbon fibre roving manufactured by Hexcel Fibers (see www.hexcelfibers.com for data sheet). |
| Impactor | Steel item attached to a drop tower for the crush of composite structures. |
| IMS | A continuous carbon fibre roving with increased tensile strength and modulus compared to HTA fibres. Manufactured by Tenax Fibers (see www.tenax-fibers.com for data sheet). |
| Isotropic | Having properties which do not vary with direction within a material. |

| | |
|---|---|
| Kevlar | Trademark for an aramid yarn produced by DuPont Ltd. |
| Matrix | Resin. |
| Melinex | Trademark for a PET polyester film supplied by GPS polyester converters. |
| PEEK | Polyetheretherketone (a thermoplastic polymer). |
| Platen | Flat plate used for the crush of composite structures. |
| Preform | An arrangement of dry fibres in the shape of a mould cavity. |
| Pre-preg | Fibres pre-impregnated with part-cured resin. |
| Pressure Pot | A device used to supply resin to a mould under pressure. |
| Reinforcement | Fibres used to provide strength in a composite. |
| RTM | Resin Transfer Moulding |
| SEA | Specific Energy Absorption |
| SEM | Scanning Electron Microscope |
| Thermoplastic | A polymeric material which is softened by the application of heat and hardened by cooling in a reversible process. |
| Thermoset | A polymeric material which is hardened by an irreversible chemical reaction. |
| Tow | An assembly of fibre filaments. |
| UCS | Ultimate Compressive Stress. |
| UD | Unidirectional. |
| Unifilo | Trade name for continuous filament random mat manufactured by Vetrotex Ltd. |
| UTS | Ultimate Tensile Stress. |
| Wet-out | Contact between fibre surface and matrix after polymerisation. |

*Parentheses*

[ ]                       Fibre lay-up details.

[ ]                       Reference Number    (References listed in order of appearance at the end of each chapter.)

*Nomenclature*

| | | *S.I. Units* |
|---|---|---|
| a | Acceleration | $m/s^2$ |
| A | Cross-sectional area | $m^2$ |
| d | Diameter of hole | m |
| D | Diameter | m |
| E | Elastic Modulus | Pa |
| F | Force | N |
| g | Acceleration due to gravity | $m/s^2$ |
| $G_c$ | Fracture energy | $kJ/m^2$ |
| $K_c$ | Fracture Toughness | $MPa/m^2$ |
| $K_T$ | Stress Concentration Factor | no units |
| m | mass | kg |
| r | Radius of hole | m |
| t | Tube wall thickness | m |
| v | Velocity | m/s |
| $\nu$ | Poisson's ratio | no units |
| $\sigma$ | Stress | Pa |

# 1.0 Introduction

Safety is a major factor in automotive vehicle design. By law, new cars must pass safety tests before being released for sale and legislation provides a minimum statutory standard. NCAP (New Car Assessment Programme) tests were introduced in the United States in 1986 and Europe in 1997 [1] and their aim is to encourage manufacturers to exceed these minimum requirements. Safety ratings of new cars are assessed by means of a front impact test, side impact test, pedestrian impact test and pole test giving an overall star rating. NCAP results enable motoring consumers to obtain reliable and accurate comparative information regarding safety performance, which has become a key element in their purchasing decision. Improving safety is not only expensive, due to increased research and development costs, but can also increase overall vehicle weight. For example, a 1.4litre Peugeot 205 manufactured in 1988 weighed 815kg [2], whilst its equivalent model, the 206, introduced in 2000, weighed 950kg [2]. In the latter, a 4 out of 5 star EuroNCAP rating for frontal and side impact was achieved but at a 16% increase in overall weight.

In the event of an accident, maximum energy has to be absorbed if drivers and passengers are to be protected effectively. To illustrate, for a 1 tonne car travelling at 70mph, the kinetic energy of the vehicle would be 450kJ. The energy absorption process should occur as smoothly as possible to minimize the accelerations to which the passengers are subjected. A load-displacement curve from an ideal energy absorber is shown in Figure 1-1. The total energy absorbed is equal to the area under the curve.
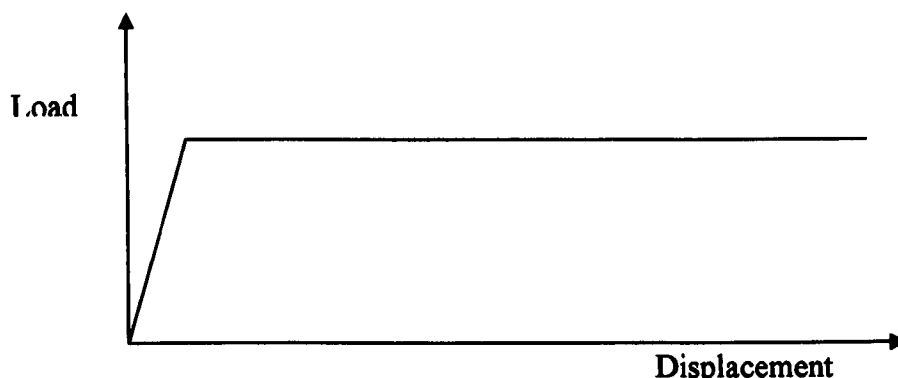


**Figure 1-1 – Load-Displacement curve for an ideal energy absorber**

The main aim of an ideal energy absorber is to reduce the disparities between final levels of deceleration and force by increasing the energy absorption capacities.

Commonly used energy absorbers in the automotive industry are manufactured from steel, which are used as crumple zones in the front and rear of vehicles. Their aim is to absorb energy in the event of an accident. However, they predominantly fail in a folding manner, due to buckling and an oscillating load-displacement curve like that in Figure 1-2 is produced.
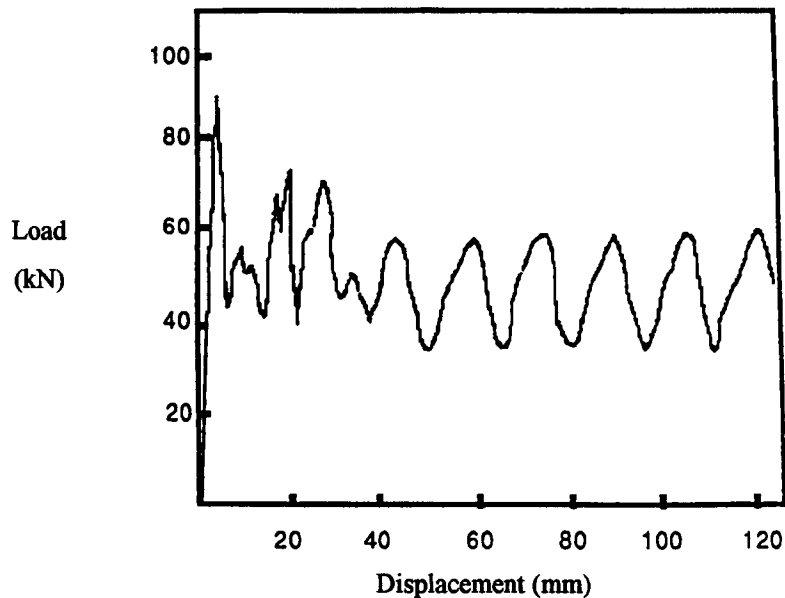


**Figure 1-2 – Typical load-displacement curve of a metallic structure failing by progressive folding [3]**

When a composite structure crushes, such as a glass/polyester tube, a load-displacement like the one shown in Figure 1-3 can be achieved. This is a much-improved interpretation of the ideal energy absorber, compared to the metallic structure, as the load level and subsequent energy absorption is more stable.

A composite material is a material up of at least two components. In many cases one of the materials will be strong and stiff, often elongated forming the fibre and is embedded in a softer material forming the matrix. Many materials are effectively composites, such as wood, steel reinforced concrete, bone or teeth. Frequently, composite materials show anisotropy as their mechanical properties vary significantly when measured in different directions. This anisotropy can be used to great advantage in the design of composite structures and offers considerable scope for integration between the processes of material specification and component design.
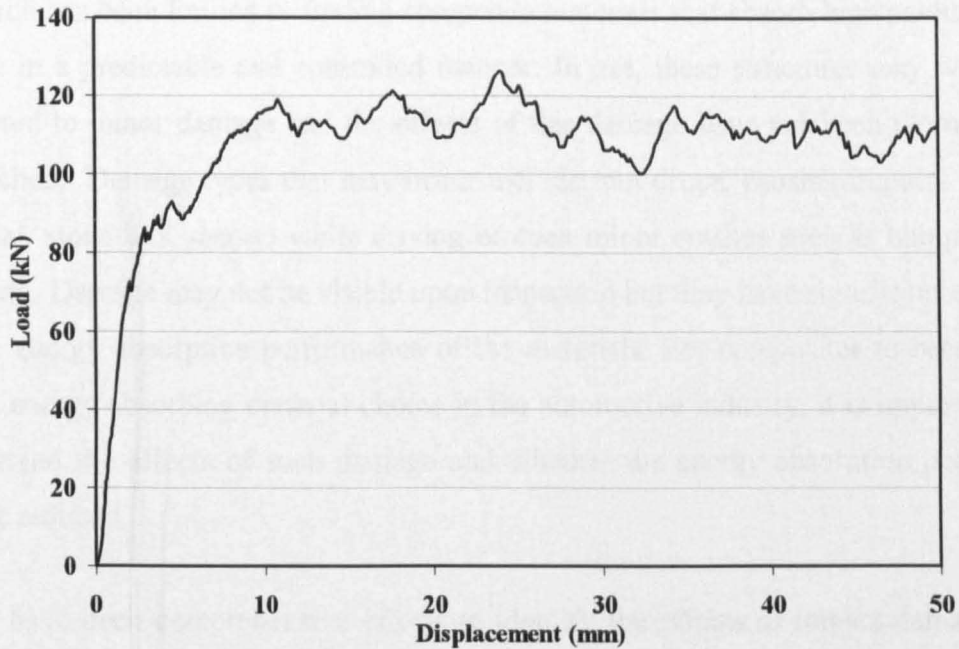
**Figure 1-3 – Typical load-displacement curve of an 89.1mm, 4mm wall thickness, CoFRM glass/polyester tube failing progressively by splaying [from preliminary tests, see Section 4.3]**

The major advantage of composites over other materials is their high specific strengths, which can be up to 4 times that of steel or aluminium. The main disadvantage is cost, as the raw materials and the design and manufacturing of parts are more expensive than for metals. As a result, composites have generally been found in low volume production applications such as Formula 1. However, due to ongoing research into cost reduction of manufacturing, the use of composites is becoming more widespread. Recent applications of composites within the automotive industry include a carbon 'A' pillar used in the Aston Martin Vanquish (2001) and crash structures at the front and rear of the Lotus Elise (1996), which are adhesively bonded to an aluminium chassis.

When comparing the performance of energy absorbers, the most useful property is the energy absorbed per unit mass. This is known as the specific energy absorption (SEA). Typical values for steel are around 35kJ/kg [4], whilst composite materials have been measured up to 227kJ/kg [5]. This illustrates that when considering energy absorption, a composite structure can be much lighter than an equivalent steel component whilst still achieving the same level of performance.

Research has been limited to finding composite materials that absorb high amounts of energy in a predictable and controlled manner. In use, these structures may well be subjected to minor damage and the effects of this damage have not been thoroughly researched. Damage types that may occur include tool drops, causing impacts in the material, stone hits, caused while driving or even minor crashes such as bumps in a car park. Damage may not be visible upon inspection but may have significant effects on the energy absorption performance of the materials. For composites to become a viable energy absorbing material choice in the automotive industry, it is important to understand the effects of such damage and whether the energy absorption potential will be reduced.

There have been comprehensive efforts to identify the effects of impact damage on the mechanical properties of composites [6]. However, other than Karbhari [7] who showed that impact damage could reduce the energy absorption of a braided composite tube, little work has been done on the effects that prior damage can have on energy absorption.

Preliminary tests conducted by the author at Nottingham (1999) have shown that drilling a 10mm hole through a composite tube, 89.1mm in diameter with a 4mm wall thickness, caused significant reductions to the energy absorption potential of the material. Figure 1-4 shows the load-displacement curve for an undamaged tube and one containing a 10mm drilled hole. During testing of the sample containing a hole, cracks were seen to propagate from the hole and drop in load, and thereby energy absorption, were observed.

The objective of this thesis is to provide an understanding of the effects of a range of defects and damage types on the mode of failure and consequent energy absorption characteristics of tubes manufactured from glass fibre reinforced polymer composites. In order to achieve this objective, tube geometry, material type and test rate will be varied. Damage thresholds based upon SEA criteria will be established. Stress concentration factors will be calculated for the induced damage in an attempt to generalise the findings from these experimental tests.
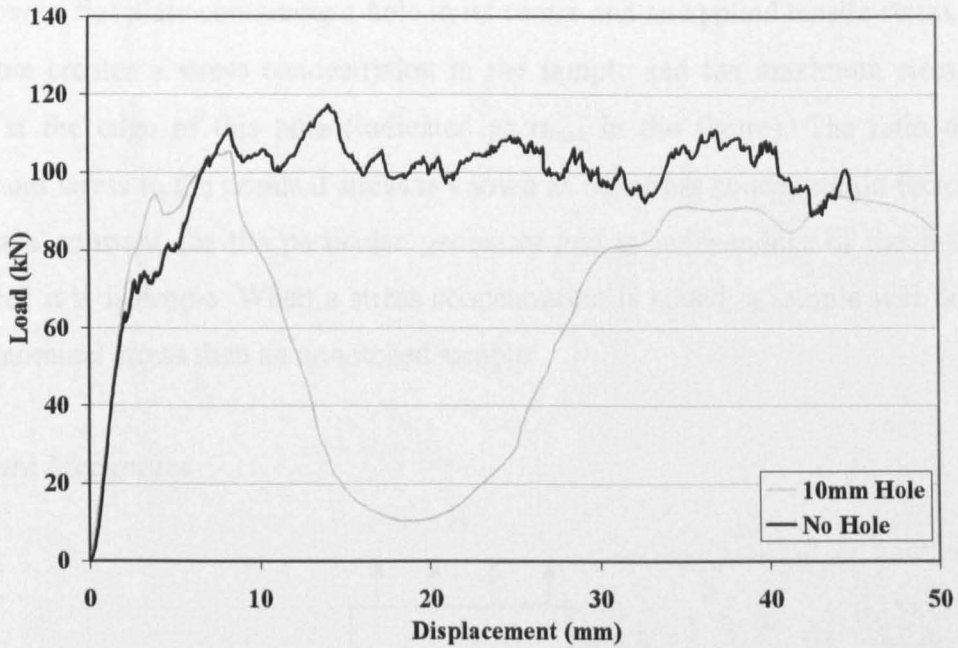
**Figure 1-4 – Load-displacement curves of an undamaged 89mm diameter, 4mm wall thickness glass CoFRM/polyester tube and one containing a 10mm drilled hole**

**[from preliminary tests, see Section 4.3]**

## 1.1 Background Theory

### *Flat Plate Under Axial Tension*

When a structure is subjected to a load in tension, it will fail when the tensile strength of the material is reached.



(a) Unnotched Sample    (b) Sample containing a hole
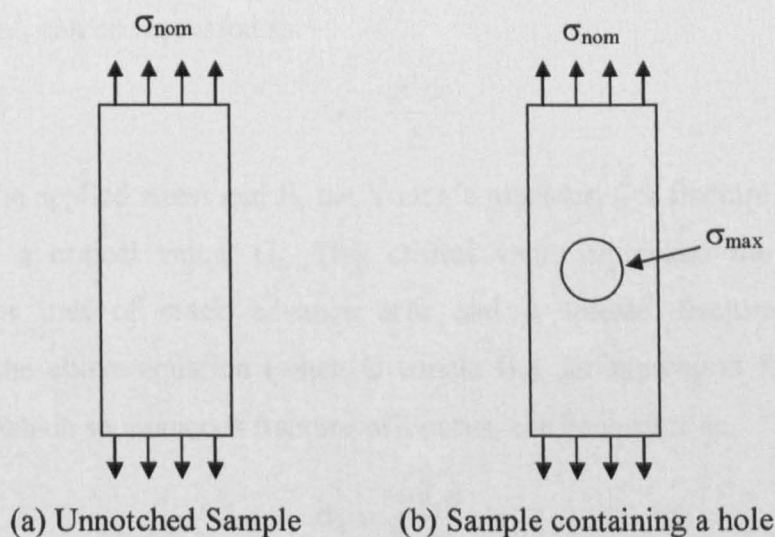
**Figure 1-5 – Schematics of an unnotched flat plate and one containing a hole in tension**

Figure 1-5 (a) shows a flat plate with a tensile stress, $\sigma_{nom}$, applied. Failure will occur if this applied stress reaches the ultimate tensile stress of the material, $\sigma_{UT}$. Figure 1-5

(b) shows a flat plate containing a hole in its centre and an applied tensile stress, $\sigma_{nom}$. The hole creates a stress concentration in the sample and the maximum stress will occur at the edge of this hole (indicated as $\sigma_{max}$ in the figure). The ratio of this maximum stress to the nominal stress is known as the stress concentration factor, $K_T$. This is a constant for the particular geometry and is independent of the material, provided it is isotropic. When a stress concentration is added, a sample will fail at a lower nominal stress than an unnotched sample.

### Fracture Mechanics
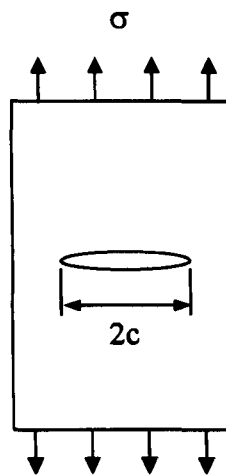


**Figure 1-6 – Schematic of a flat plate containing a crack, under tension**

For a sample with a pre-existing crack, of length 2c (Figure 1-6), the energy release rate, G, in J/m$^2$, can be expressed as:

$$G = \frac{\sigma^2 \pi c}{E}$$

Where $\sigma$ is the applied stress and E, the Young's modulus. For fracture to occur, this must exceed a critical value, $G_c$. This critical value represents the total energy absorbed, per unit of crack advance area and is termed fracture energy. By rearranging the above equation (when G equals $G_c$), an expression for the critical stress, $\sigma_c$, at which spontaneous fracture will occur, can be written as:

$$\sigma_c = \sqrt{\frac{G_c E}{\pi c}}$$

The stress intensity factor, K, defines the magnitude of the elastic stress field in the vicinity of the crack tip and can be expressed as:

$$K = \sigma \sqrt{\pi c}$$

The entire stress field is characterised and a critical value of this stress intensity factor, $K_c$, can be identified for the case when G equals $G_c$ and spontaneous fracture occurs:

$$K_c = \sigma_c \sqrt{\pi c} = \sqrt{EG_c}$$

This critical stress intensity factor is often known as fracture toughness. In the context of this study, the fracture toughness can be seen as a property that may significantly affect the damage tolerance of the tubes.

### Cylinder Under Axial Compression

Cylindrical samples (tubes) tested in this study are placed under axial compression as shown in Figure 1-7.
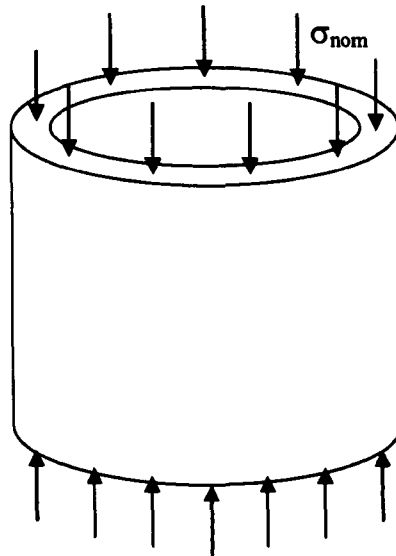


**Figure 1-7 – Schematic of a cylinder under axial compression**

Failure of the sample will occur when the applied stress, $\sigma_{nom}$, reaches the ultimate compressive stress of the material, $\sigma_{UC}$. However, a trigger, in the form of a 45° bevel at one end of the tube was used. This produces a stress concentration caused by the reduction in cross-sectional area. As samples crush, load increases until a steady state load is achieved and a splaying mode of failure observed (see section 2.2.1). If the maximum stress in the sample at this steady crush load is less than $\sigma_{UC}$, then samples will continue to crush and a load-displacement curve like that in Figure 1-3 can be achieved.

Samples containing induced damage will have an added stress concentration. The maximum stress will occur at this damage point and will be equal to the applied stress

multiplied by a factor, $K_T$. $K_T$ is defined as the ratio of maximum stress ($\sigma_m$) to the nominal stress ($\sigma$) and is shown in equation (1-1).

$$K_T = \frac{\sigma_m}{\sigma}$$

(1-1)

Fast fracture, originating at the damage area will occur if this maximum stress is greater than $\sigma_{UC}$. The subsequent load displacement curve produced would be similar to that of the sample containing a 10mm hole in Figure 1-4. The load level and subsequent specific energy absorption are reduced due to the loss of a steady crush.

Within this study threshold levels of damage, where the maximum stress is lower than that required for fast fracture to occur, are to be found. In an attempt to generalise these thresholds, $K_T$ values will be calculated.

## 1.2 Chapter 1 References

[1] http://www.euroncap.com

[2] From manufacturer's data.

[3] Hull D, A Unified Approach to Progressive Crushing of Fibre-Reinforced Composite Tubes, Composites Science and Technology, Vol.40, pp377-421, 1991.

[4] Thornton PH and Magee CL, The interplay of geometric and materials variables in energy absorption, Journal of Engineering Materials and Technology, Transactions of the ASME, Vol.99, pp114-120, April 1977.

[5] Ramakrishna S, Hamada H, Maekawa Z and Sato H, Energy Absorption Behaviour of Carbon Fibre Reinforced Thermoplastic Composite Tubes, Journal of Thermoplastic Composite Materials, Vol.8, pp323-344, 1995.

[6] Abrate S, Impact on Composite Structures, Cambridge University Press, Cambridge, 1998.

[7] Karbhari VM, Haller JE, Falzon PK, Herszberg I, Post-impact crush of hybrid braided composite tubes, International Journal of Impact Engineering, Vol. 22, pp419-433, 1999.

# 2.0 Literature Review

This section looks the failure modes associated with composite tube crush. The effect of materials, geometry and test conditions on the energy absorption potential will then be discussed. Finally, the effect of damage on the impact performance of composite materials will be considered.

## 2.1 Failure Modes Associated With Composite Tube Crushes

During the axial compression of tubular composite structures two types of failure are observed: progressive (or stable), and catastrophic (or unstable). Four modes of progressive crushing were identified and described by Farley and Jones [1][2][3][4]. These were splaying or lamina bending, fragmentation or transverse shearing, local buckling and brittle fracturing.

### 2.1.1 Splaying or Lamina Bending

In this mode of crush a complex "crush zone" is formed at the end of the structure containing a stress concentrator and progresses along its length. Figure 2-1 shows a schematic of the formation of this crush zone for a composite tube with a 45° chamfer (the stress concentrator). As the crush zone progresses down the structure the laminae bend and split into smaller sections called fronds, and a large central wall crack is produced. The principal energy absorptions are from the crack growth and friction. The central wall cracks observed are similar to those in the fragmentation failure mode (see next section) but are usually at least one order of magnitude greater in length [1][2][3][4]. Figure 2-1 shows a representation of the characteristics of the splaying failure mode.
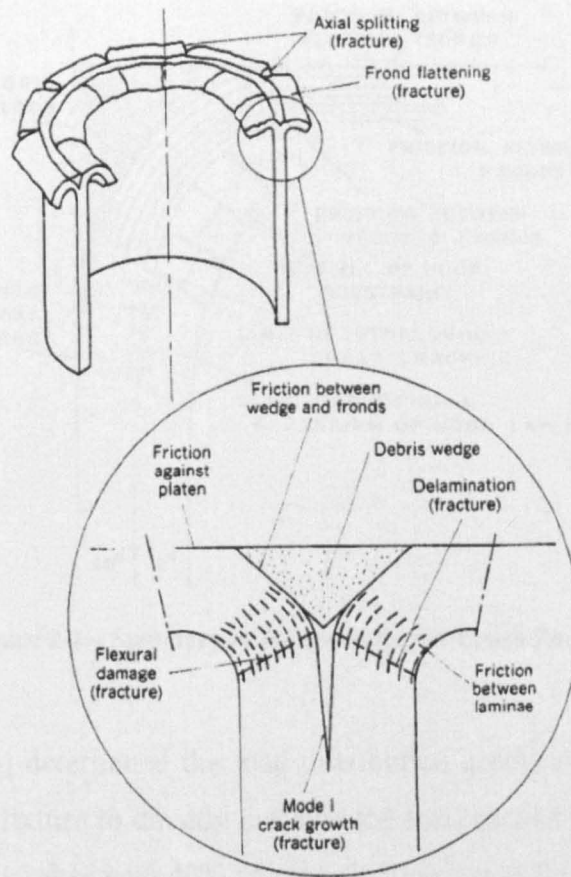
**Figure 2-1 – Characteristics of the Splaying Failure Mode [6]**

Hull [5] identified the following forces acting in the crush zone and these are shown in Figure 2-2:

- Compressive forces acting at the platen on the fronds and debris wedge.
- Friction at the platen owing to the sliding of the splayed fronds across the platen surface as crushing proceeds.
- Friction between the debris wedge and fronds.
- Friction between the adjacent laminae in the fronds as they bend through different radii of curvature.
- Hoop constraints resulting from crack opening along the centre of the wall of the tube.
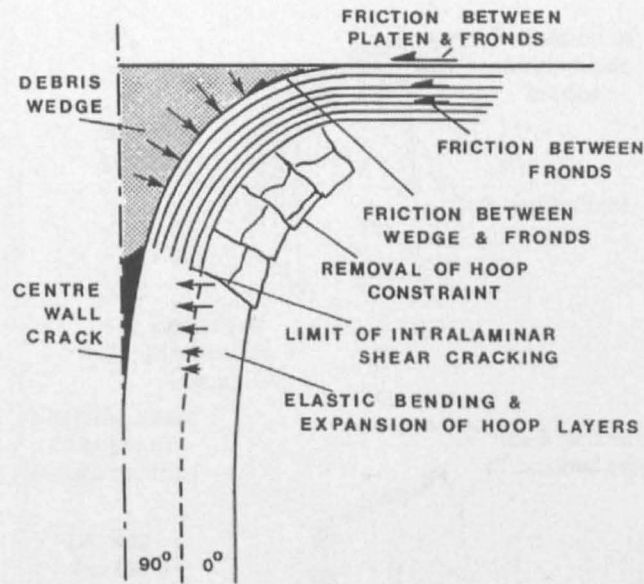
**Figure 2-2 – Summary of Forces Acting in Crush Zone [5]**

Fairfull and Hull [6] determined the load distribution across the crush zone using a custom-built platen fixture to directly measure the load carried by each of the fronds. For glass cloth/epoxy tubes with 40% volume fraction it was found that the proportion of load supported by the internal fronds, debris wedge and external fronds was 13%, 67% and 20% respectively.

### 2.1.2 Fragmentation or Transverse Shearing

A schematic of the fragmentation crushing mode is shown in Figure 2-3. Shear cracks form during crush, producing rings of material to the inside and outside of the tube. These rings then fail in compression to the inside and tension to the outside of the tube forming shorter segments.

Farley reported that the energy absorption in this mode is dominated by interlaminar crack growth and lamina bundle fracture [7]. Interlaminar crack growth is controlled by the mechanical properties of the matrix and fibres and the orientation of the laminate.

This failure mode is observed when structures are manufactured using brittle fibres, especially when the resin toughness is low and tensile strength high.

Farley [2] also reported that the following conditions must be met for local buckling to occur in brittle composites:

- The fibre Young's modulus is low compared with the strength of the matrix;
- The matrix has a large failure strain (i.e. is tough);
- The matrix failure strain exceeds fibre strain.

Farley also states that crushing failure in a manner associated with Kevlar (an axial fibre with a large failure strain) will occasionally exhibit a local buckling failure.

### 2.1.4 Other Failure Modes

Farley [4] also analysed a fourth progressive crush mode; brittle fracture which is a combination of the transverse shearing and lamina bending failure modes. Lamina bundles in brittle materials have a large bending radius in comparison to the case of the transverse shearing mode.



**Figure 2-3 – Characteristics of the Fragmentation Crushing Mode [4]**

### 2.1.3 Local Buckling leading to Progressive Folding

The characteristics of the local buckling mode are shown in Figure 2-4. This is a failure seen most commonly in ductile metals but is also exhibited by brittle and ductile fibre-reinforced composites [2].
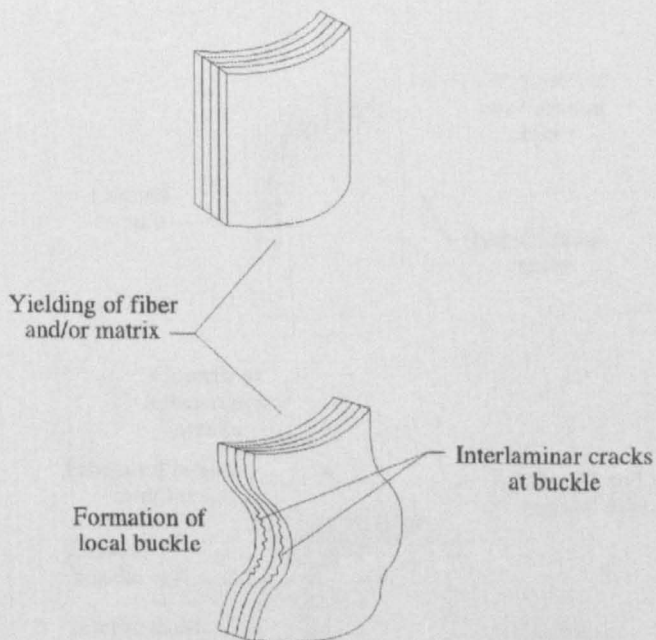


**Figure 2-4 – Characteristics of the Local Buckling Mode [4]**

Farley [2] also reported that the following conditions need to be met for local buckling to occur in brittle composites:

- The interlaminar stresses are small compared with the strength of the matrix.
- The matrix has a higher strain to failure than the fibres.
- The matrix exhibits yielding under high stresses.

Farley also stated that it is the ductile composites, such as those based upon Kevlar® (an aramid fibre produced by DuPont Ltd) fibres that more commonly exhibit a local buckling failure.

## 2.1.4 Other Failure Modes

Farley [4] also discussed a fourth progressive crush mode, a brittle fracture which is a combination of the transverse shearing and lamina bending failure modes. Lamina bundles in brittle fracturing exhibit some bending and can fracture near the base of the lamina bundle. When a lamina bundle fractures, the load is redistributed within the specimen, and the cyclic process of crack growth and lamina bundle bending and fracturing is repeated. The characteristics of the brittle crushing mode are shown in Figure 2-5.
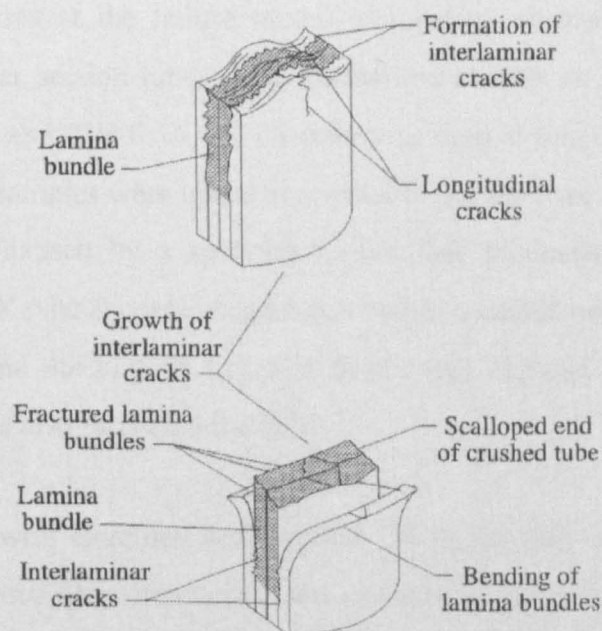


Figure 2-5 – Characteristics of the brittle fracturing crushing mode [4]

## 2.2 The Effect of Materials, Geometries and Test Conditions on the Energy Absorption of Composite Materials

Research carried out on various composite structures, such as tubes and cones, have been well documented in the literature. This section provides an overview of the effect on the energy absorbing capabilities of composites of material type, geometry and test conditions.

### 2.2.1 Fibres

The most commonly used and well-documented reinforcements are carbon, glass and Kevlar®. When comparing specific energy absorption it is generally accepted that structures containing carbon reinforcement are more effective energy absorbers than those containing glass reinforcement, which in turn are more effective than Kevlar® structures. Carbon and glass reinforced samples generally fail by splaying and the greater mechanical properties of carbon lead to larger SEAs. Kevlar® reinforced tubes are often associated with a buckling failure mode and this leads to lower SEAs than carbon or glass samples. Hybrid structures have also been studied, where mixtures of these different reinforcement types have been used to tailor properties. The energy absorption capabilities of these fibres is discussed and compared here.

Thornton et al [8][9], tested tubes made from E-glass, Thornel 300 carbon and Kevlar® fibres, looking at the failure modes and energy absorptions. Cylindrical, square and rectangular section tubes were manufactured with an epoxy matrix and fibre lay-ups of ±45° and 0°/90°. A 45° chamfer was used at one end of the tubes to initiate crush and all samples were tested at a speed of 0.21mm/sec. Tubes made from glass and carbon collapsed by a splaying failure that produced SEAs of around 60kJ/kg whereas the Kevlar® containing tubes, tended to buckle unstably and so gave lower SEAs of around 40kJ/kg. It was also found that changes to the lay-up that increased the modulus also increased the SEA.

PEEK matrix tubes with Hercules AS-4 carbon, Hercules IM7 carbon or OCF S2 glass prepregs in various fibre orientations were studied by Hamada and Ramakrishna [10]. The tubes were manufactured with layups of 0°, ±5°, ±10°, ±15°, ±20° and ±30°. Specimens were 55mm in outer diameter with a 2.65mm wall thickness and were

tested at a constant crosshead speed of 1mm/min. It was found that the ±30° orientations of all fibre types and the S4 with ±25° orientation produced a catastrophic failure in the tubes. All the other specimens failed progressively in splaying mode. The AS4 tubes produced a maximum SEA of 226.8kJ/kg for the ±15° samples with energy absorptions dropping by up to 20% with changes to the fibre architecture. The IM7 tubes saw a maximum SEA in the ±10° samples of 209kJ/kg and drops in SEA of up to 15% as the fibre angle was increased or decreased. The S2 tubes produced a maximum SEA of 190.6kJ/kg in the ±10° samples. The SEA increased with increasing fibre angle up to 10 ° then dropped off with further increases of angle to 20°. Overall the fibre orientations affected the SEAs but the carbon samples displayed around 20% higher SEAs than the glass. It was also found that the AS4 tubes absorbed around 10% more energy than the IM7 tubes.

Farley [11] compared high and low strain to failure carbon prepregs, Hercules AS-4 fibres with a strain to failure of 0.015 and Thornel 300 (T300) fibres with a strain to failure of 0.012, in low (0.010) and high (0.020) strain to failure epoxies. It was found that the high strain to failure carbon and epoxy gave higher SEAs than the other material combinations. Overall the AS-4 fibres exhibited 12-28% higher energy absorption than the T300 fibres, dependent on fibre orientation. It was also found that the higher strain to failure matrix improved the performance of both the AS-4 and T300 fibres. Further work [12] using high strain Hercules AS-6 carbon prepregs with a high strain epoxy did not follow this trend, as the failure mode changed from splaying to fragmentation, reducing the energy absorption. Farley [4] also crushed tubes manufactured from E-glass, T300, AS4, AS6, P55 and P75 carbon fibres in an epoxy matrix. No obvious relationships were found between the fibre modulus and the SEA. As the modulus of the fibres increased from 75GPa to 210GPa an increase in SEA was observed, and this increase was attributed to the greater force needed to bend the lamina bundles. These tubes all failed by splaying, but for fibres with a modulus above 210GPa the failure mode changed to fragmentation, where lamina bundles exhibit less bending, can fracture near the base, and the SEA decreased.

Based on the above work, Farley [12] tried to correlate fibre modulus with specific energy absorption. It was concluded that the SEA was more significantly affected by the strain to failure than the modulus.

Chiu et al [13] crushed 3-D carbon/epoxy and Kevlar®/epoxy braided composite square tubes at a rate of 0.21cm/sec. Figure 2-6 shows a schematic of the 3D braid architecture used in manufacture.
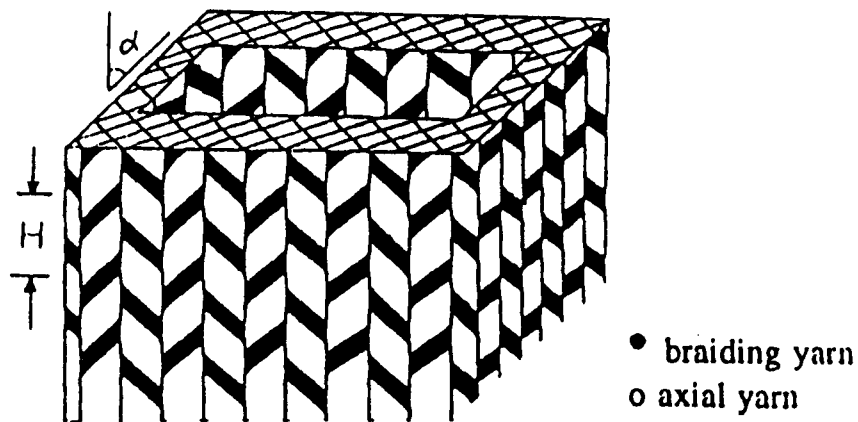


**Figure 2-6 – Schematic of the 3D braided tubes tested by Chiu et al [13]**

The carbon tubes splayed before bending to final failure while the Kevlar® tubes exhibited a progressive folding crush. The SEAs were found to be higher for the carbon tubes (54.2kJ/kg) than the Kevlar® tubes (25.6kJ/kg), however, the Kevlar® tubes demonstrated good post-crush structural integrity. It was concluded that in 3-D braided composite tubes, the axial yarns contribute most to energy absorption and the braiding yarns determine the crushing failure mode.

Duckett [14] crushed glass CoFRM/polyester and braided carbon/vinylester tubes with ±30°, ±45° and ±60° fibre lay-ups. Circular and square sectioned tubes were tested, and wall thickness was varied. Tests were conducted at 0.5mm/min. The glass/polyester tubes produced an SEA of 60.7kJ/kg and the highest SEA seen in the braided carbon tubes was 60.4kJ/kg for the ±60° samples. For these braided samples it was shown that samples with more axially aligned fibres produced higher SEAs with the ±30° samples producing energy absorptions as low as 26.5kJ/kg. Square section tubes were shown to absorb less energy than circular sections and this was attributed

to changes in crush mode, with premature failure observed around the corners of the square tubes.

Several authors have also tried combining reinforcements to improve the energy absorbing potential of tubes. This process is known as hybridisation and is reviewed below.

Farley [15] crushed carbon/Kevlar®, carbon/glass and glass/Kevlar® hybrid tubes, comparing the results with those from tubes made with a single material. The tubes were manufactured with fibre layups of [±45°] and [0/±θ] with θ ranging between 15° and 90°. Tests were conducted at 0.018cm/min until crushing was initiated and then increased to 0.076cm/min for the remainder of the crush. It was found that for θ of less than 45° the carbon tubes absorbed more energy (100kJ/kg) than either the Kevlar® or glass samples (30kJ/kg). For θ over 60° it was found that the energy absorption was similar for all materials with an SEA of around 50kJ/kg. When hybridisation took place the only samples which performed better than a single fibred sample were the carbon/Kevlar® and carbon/glass samples producing higher SEAs than the pure carbon sample.

The crush of triaxially braided, hybrid composite tubes were conducted by Karbhari et al [16][17]. The specimens were manufactured from glass, carbon, Kevlar® or a combination of the materials with biaxial [±45°] or triaxial [0°/±45°] fibre architecture (see Figure 2-7).



(a)



(b)
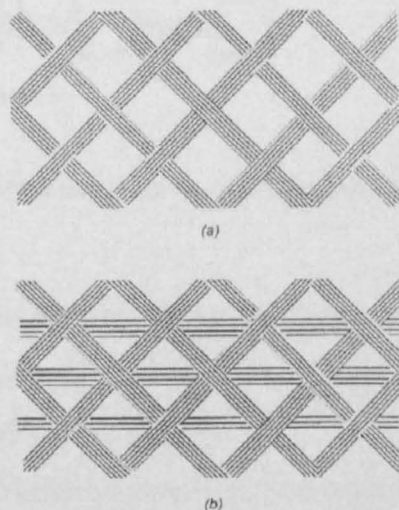
**Figure 2-7 – Schematic of braid architecture (a) biaxial (b) triaxial [17]**

Samples were tested at a rate of 25.4mm/min and tubes used a 45° chamfer as trigger. From 15 types of tube tested the highest three energy absorptions were recorded by the hybrid samples with the glass bias yarns and carbon axial fibres producing the highest SEA of 64.21kJ/kg. The lowest SEA was seen in the glass/Kevlar® biaxial samples, which produced an average SEA of just 30.70kJ/kg. The SEA values were sensitive to the number of plies used and it was shown for the Kevlar®/glass biaxial tubes with carbon axial fibres an increase in energy absorption of 48% was achieved by increasing the number of plies from two to three. In conclusion, it was stated that hybridisation in braided tubes can significantly affect the crush response. The optimum performance was achieved with a triaxial braid and the use of carbon axial fibres. Karbhari and Haller [18] also crushed hybrid composite structures in the form of a set of flange-connected tubes (see Figure 2-8).
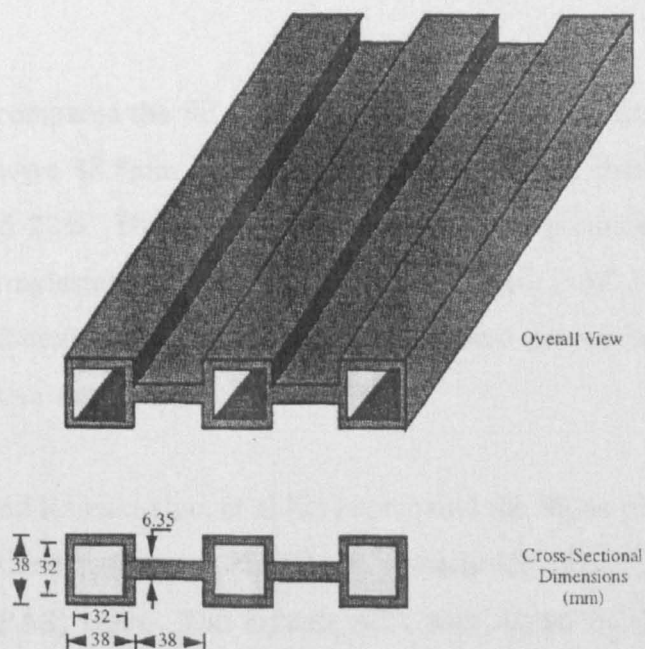


Figure 2-8 – Schematic of flanged tubes tested by Karbhari [18]

Samples manufactured from carbon, carbon/Kevlar® and Kevlar® in a vinylester resin were crushed at 1mm/sec. The best performance was seen from a carbon/Kevlar® structure orientated at ±45°.

It has been shown that more efficient structural components may be produced through hybridisation by tailoring sequences of damage mechanisms.

Chiu et al [19] crushed 2D triaxially braided carbon/Kevlar® tubes and six different hybrid structures were manufactured by varying the fibres used for the axial and bias yarns.

Three types of failure were observed. The tubes with carbon braiding failed by progressive splaying, the tubes with Kevlar® braiding failed by progressive folding and the tubes with carbon and Kevlar® braiding failed in a spiral curling mode. The highest SEA was recorded in the tubes containing carbon axial and braiding yarns where a value of 51.4kJ/kg was produced. The lowest energy absorption was seen in the tubes containing Kevlar® axial and braiding yarns where an SEA of 14.4kJ/kg was recorded.

A large difference in energy absorption has been identified between the splaying and folding failure modes and the importance of promoting a splaying failure mode to ensure high SEA levels has been shown.

### 2.2.2 Resin

Turner et al [23] compared the SEAs of glass CoFRM tubes in epoxy, vinylester and polyester. Tubes were 88.8mm in diameter, had a 4mm wall thickness and volume fraction of around 23%. The epoxy resin was found to produce the highest SEA (≈80kJ/kg), then vinylester (≈77kJ/kg) and finally polyester (≈58kJ/kg). The increases in SEA were attributed to an increase in all mechanical properties, in particular the ultimate compressive stress (UCS).

Satoh et al [20] and Ramakrishna et al [21] compared the SEAs of carbon reinforced tubes with polyetheretherketone (PEEK), polyetherimide (PEI), polymide (PI) and polyarylsulfone (PAS) resins. The highest SEA was shown by the PEEK tubes of 194.1kJ/kg, then the PEI tubes at 155.4kJ/kg, PI at 131.4kJ/kg and finally the PAS tubes at 121.8kJ/kg. The differences were attributed to the higher fracture toughness of PEEK. These tubes had a shorter wall centre wall crack, more frond splits and more fibre fractures than the other tubes. It was also found that the energy absorption showed a linear relationship with the mode I fracture toughness.

Hamada et al [22] compared axial compressive tests of carbon/epoxy and carbon/PEEK tubes made from unidirectional prepreg. Three fibre architectures were tested: 0°, ±30° and ±45°, for sets of tubes with or without a 45° chamfer. It was

found that progressive crushing was only established in the ±45° carbon/epoxy and 0° carbon/PEEK tubes and SEAs of 53kJ/kg and 180kJ/kg were calculated respectively. It was also noted that the epoxy tubes crushed with a large central wall crack, whereas the PEEK tubes crushed with a short central wall crack and small debris wedge.

From [20][21][22] it has been shown that a significant amount of energy is absorbed from fibre fractures and frond splits and this is a direct consequence of the observed shorter wall crack. The higher fracture toughness of the PEEK matrix has caused these shorter wall cracks and smaller debris wedges and hence, produced higher SEAs Fronds have to bend at a sharper radius of curvature and subsequently produce more cracks and higher numbers of fibre failures in compression and tension to the inside and outside of the fronds respectively.

### 2.2.3 Other Material Variables

*Volume Fraction*

Farley [4] compared carbon/epoxy tubes with fibre volume fractions between 40 and 55% and fibre architectures of [±45]$_6$, [0/±15]$_4$ and [0±75]$_4$. The [±45]$_6$ and [0/±15]$_4$ showed a decrease in SEA as the volume fraction increased over the range tested. This decrease was due to reduced interlaminar strength of the specimens. As the volume fraction increases the fibre spacing is reduced which results in higher interlaminar stresses and consequently, lower interlaminar strength. The samples had crushed by lamina bending or brittle fracture and the energy-absorption of these crush types is significantly influenced by the interlaminar strength of the material. The [0/75]$_4$ tubes exhibited a slight increase in SEA as fibre volume fraction increased and this was attributed to the increased laminate stiffness of the material.

Farley [12] also tested Kevlar®/epoxy tubes with volume fractions of between 46 and 70% and fibre architectures of [±45]$_6$, [0/±15]$_4$ and [0±75]$_4$. Increasing the volume fraction between 46 and 55% made negligible difference to the SEA as the crush mode remained unchanged. However, when increasing volume fractions from 55 to 70% the [±45]$_6$ and [0±75]$_4$ tubes saw a decrease in SEA of 10%. The reverse of this was seen in the [0/±15]$_4$ tubes which saw an increase in SEA of 10% over the same increase of volume fraction.

It has been shown here [4][12]that SEA can be affected by varying the fibre volume fraction. Depending on the materials and fibre lay-up, an increase in volume fraction can either increase or decrease the SEA. This is due to the failure mode of the tubes. The carbon/epoxy tubes that failed by lamina bending or brittle fracturing saw an increase in SEA as volume fraction increased due to an increased laminate stiffness. The Kevlar® tubes however failed by splaying and rely on axial fibres to absorb energy as fronds bend. Samples that contained no axial fibres or a higher percentage of transverse fibres ([±45]$_6$ and [0±75]$_4$ tubes) saw decreases in SEA as volume increased. Samples with more axially oriented fibres ([0/±15]$_4$ tubes) saw increases in SEA as volume fraction increased.

Ramakrishna and Hull [24] investigated the crush of knitted-carbon-fibre-fabric/epoxy tubes tested under axial compressive load. Monolayer tubes with a volume fraction of between 5.25% and 15.75% showed an increase in SEA as volume fraction increased from around 15kJ/kg to just over 20kJ/kg. Double layer tubes with volume fractions of between 10.5% and 30.5% showed a much larger increase in SEA of 20kJ/kg up to 60kJ/kg for the tubes with a 30.5% volume fraction. It was concluded that a volume fraction of above 15% was required to produce progressive crushing.

From the work discussed here on the effect of fibre volume fraction on energy absorption it has been shown that when a higher proportion of fibres are axially aligned an increase in SEA is seen. This is due to the fibres bearing the majority of load in these samples and hence when more are added an increase in energy absorption is produced. However, when the fibres play a reduced part in the energy absorption, i.e. when fewer axially aligned fibres are in the material, a reduction in SEA is seen as volume fraction increases. Farley [12] suggested that this was due to a reduction in interlaminar shear strength.

### 2.2.4 Specimen Geometries

*Cross-sectional Geometry*

The t/D ratio of tubes is the wall thickness divided by the outer diameter of the tube. Varying this ratio can provide different SEAs and failure modes for tubes manufactured from the same materials. Hamada and Ramakrishna [25] investigated

the effects of the t/D ratio on the energy absorption of carbon-fibre/PEEK composite tubes. They found that tubes with a smaller t/D ratio than 0.015 failed by brittle fracture mode and tubes with a higher t/D ratio than 0.015 failed progressively. They also found that the SEA was dependent on the absolute value of t rather than the t/D ratio, increasing t up to a certain value before falling again. The highest energy absorptions were displayed for tubes with a wall thickness between 2-3mm and the reductions in SEA for thinner and thicker walled samples were attributed to changes in the crush zone morphology. For thinner walled samples, the reduction was due to instability under axial load causing the brittle fracture mode of failure. For thicker walled tubes, longer and more frequent longitudinal cracks were seen. The reduction in SEA was attributed to these longer cracks as these would enable fronds to bend more easily.

Fairfull and Hull [26] investigated the effects of specimen geometries on the energy absorption of glass/epoxy tubes. They looked at tubes with diameters ranging from 16mm to 50mm and t/D ratios between 0.05 and 0.40. It was found that the energy absorption increased with decreasing D and that the optimum t/D ratio was 0.20. No reason was given as to why the SEA changed and it was concluded that there can be no universal relationship to predict the SEA of composite tubes.

Thornton [8, [9] investigated the energy absorption of circular, rectangular and square cross-sectioned tubes manufactured from glass, Kevlar® and carbon and with varying t/D ratios. They found that the circular tubes demonstrated stable crushes over the widest range of t/D ratios. They pointed out that as long as the tube dimensions are such that the tube crushes stably the SEA is essentially independent of geometry. This seems to contradict the findings of Fairfull and Ramakrishna discussed earlier. However, the variations in SEA were due to a change in failure mode when the geometry was varied. Thornton's work suggests that if the failure mode remains the same, then SEA will remain relatively unchanged.

Farley [27] conducted tests on carbon/epoxy and Kevlar®/epoxy tubes to examine the influence of specimen geometry on the energy absorption capability. Circular tubes with inside diameters varying between 1.27cm and 10.16cm were tested with D/t

ratios in the range 1.4 to 125.0, where D was the inner diameter and t the wall thickness. Reducing the D/t ratio increased the SEA and this was attributed to a reduction in interlaminar cracking in the crushed region of the tube. The Kevlar®/epoxy tubes were geometrically scaleable, whereas the carbon tubes were not. This meant that Kevlar® tubes with different diameters but the same D/t ratios achieved similar SEAs.

*Crush Initiation*

It is commonly accepted that some form of initiator is needed to start the progressive crush of tubes and the most widely used is a machined chamfer which is reliable and easy to apply. Several other forms of crush initiator have been used by various authors and are discussed along with the chamfer here.

Sigalas et al [29] conducted a study of chamfer-based trigger mechanisms of glass cloth/epoxy tubes with angles, φ, of between 10° and 90° (see Figure 2-9 to Figure 2-11). It was found from these tests that the early stages of the stable crushing process are dominated by the formation of wedges of crushed material and the subsequent generation of lateral cracks and small rings of material. It was found that the chamfer angle had no effect on the steady state crush zone or steady state crush load and no reason was given for this. However, there was a difference seen in formation of the crush zone with three distinct types for angles below 30°, between 30° and 80° and above 80°. These three modes are shown in Figure 2-9 to Figure 2-11.



**Figure 2-9 – Schematic representation of the initial crushing process for chamfer angles of less than 30° [29]**

P1
Chamfer
φ
50°
external
2.5mm
internal
a)
P2
bending
b)
P3
c)
P4
30° 30°
d)
P5
0.9
wedge
0.6
e)

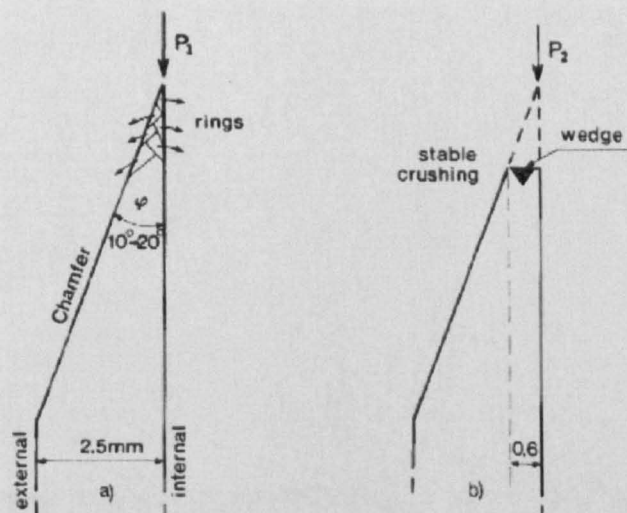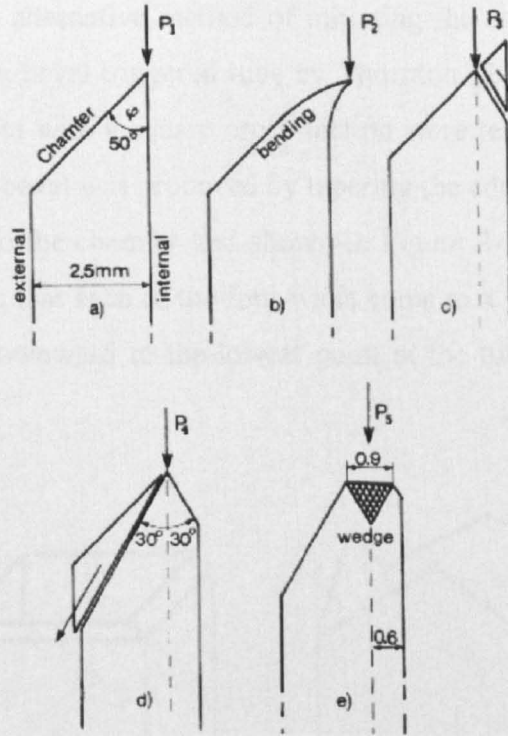

**Figure 2-10 - Schematic representation of the initial crushing process for chamfer angles of between 30° and 80° [29]**


P1
Chamfer
φ
80°
external
2.5mm
internal
a)
P2
main crack I
crack II
30°
b)
P3
crack III
0.6
c)
P4
30° 30°
0.6
d)
P5
0.9
wedge
0.6
e)

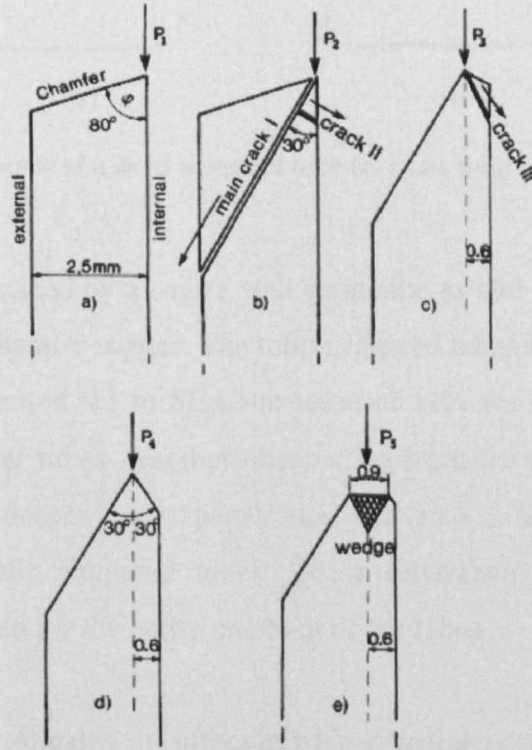

**Figure 2-11 – Schematic representation of the initial crushing process for chamfer angles of greater than 80° [29]**

The tulip trigger is an alternative method of initiating the crush of composite tubes and was compared to a bevel triggered tube by Thornton [30]. E-glass/polyester and E-glass/vinyl ester tubes with a square cross-section were tested with both the bevel and tulip triggers. The bevel was produced by tapering the edges of the tube to a point at the centre, similar to the chamfer and shown in Figure 2-12 (a). The geometry of the tulip trigger is such that each of the four walls come to a point at the centre of the wall and then slope downward to the lowest point at the tube corners, as shown in Figure 2-12 (b).



(a)                                    (b)
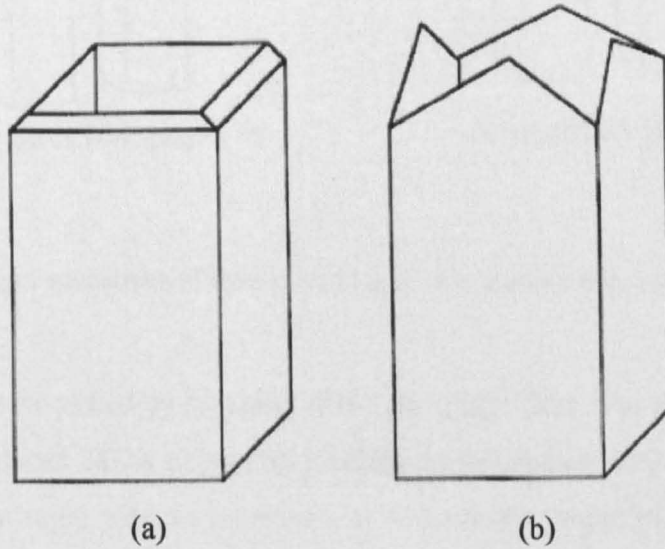
**Figure 2-12 – Schematic of a bevel triggered tube (a) and a tulip triggered tube (b) [30]**

The bevelled tubes crushed by a centre wall formation as had been seen with circular section tubes with a chamfer trigger. The tulip triggered tubes however, formed cracks throughout their walls and led to SEA increases of 31% for the polyester tubes and 90% for the vinyl ester tubes. Another observation from the tests was that the bevel triggered tubes had deeper crack penetration but also a larger distance between fractures than the tulip triggered tubes. These differences developed during the initiation and continued for the entire crushing of the tubes.

Jimenez et al [31] investigated the effect of trigger geometry on the energy absorption of glass/polyester box section and I section structures. Bevel and tulip triggers were compared for the box sections with bevel or tulip angles of 30°, 45° and 60°. The I

section samples were cut to a point in two different directions and again this point had angles of 30°, 45° and 60°. Figure 2-13 shows the trigger geometries of the samples.
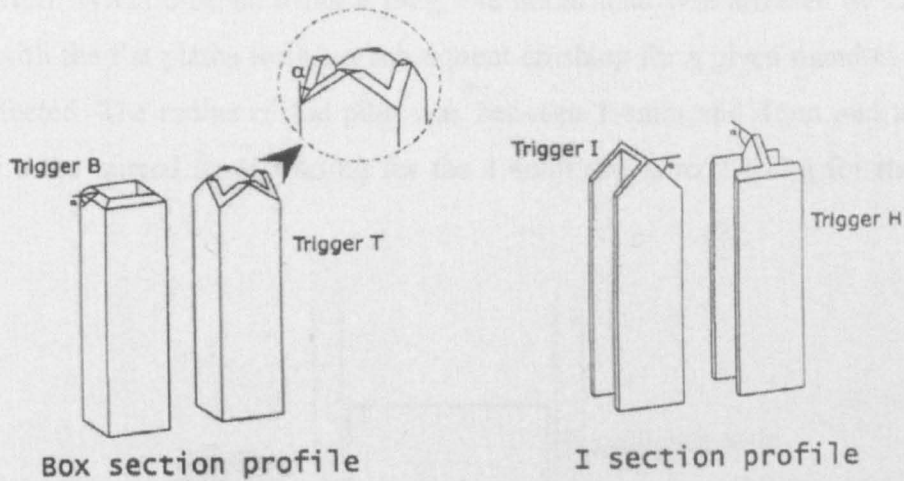


**Figure 2-13 – Trigger geometries of the box and I section specimens tested by Jimenez et al [31]**

The specimens were tested by crushing at 0.21mm/s for 9cm. For the box section the tulip trigger produced SEAs of around 43kJ/kg for all angles. The bevel trigger was more affected by angle with an increased SEA from just under 36kJ/kg for both the 30° and 45° samples to 44.8kJ/kg for the 60° angle. This was an increase of around 25% and showed the highest SEA of any of the samples tested. The I sections were unaffected by changes to trigger angle and produced SEAs between 37 and 39kJ/kg for all trigger types and angles.

Although the tulip trigger increased the energy absorption of square and rectangular section tubes it has yet to be proved for circular section tubes. This is due to the more complex manufacturing method involved in producing a cylindrical tube with a tulip trigger.

The last type of trigger discussed here is an internal mandrel, which fits within the internal wall of a chamfered tube and has a radius, R, at the edge that the tube crushes against (see Figure 2-14). Hull and Coppola [32] investigated the effects of chamfer angle and internal mandrel radius on the energy absorption of glass/vinyl ester circular tubes. Initially tubes were crushed with different chamfer angles on to a flat

platen as a comparison for the internal mandrel tests. It was found that the peak load before the onset of progressive crushing was influenced by this chamfer angle but the progressive crush load and SEA were unaffected and an average SEA of 61.4kJ/kg was achieved. When crushed using a plug, the initial load was affected by chamfer angle as with the flat platen tests but subsequent crushing for a given mandrel radius, was unaffected. The radius of the plug was between 1.4mm and 4mm and average SEAs for these ranged from 50kJ/kg for the 1.4mm radius to 27kJ/kg for the 4mm radius.
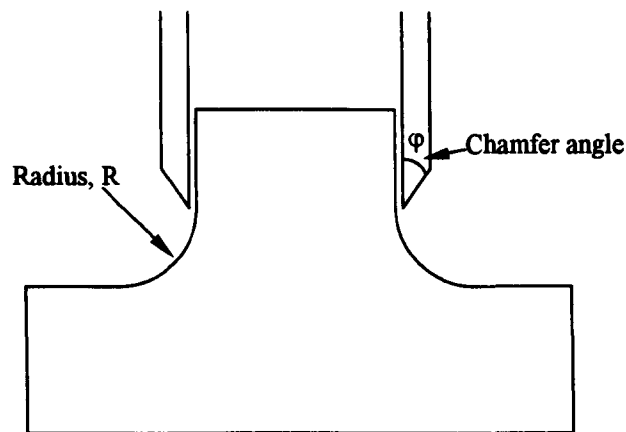


**Figure 2-14 – Internal mandrel used in tube crush tests conducted by Hull and Coppola [32]**

From the results seen here, the trigger mechanism has not been shown to significantly affect SEA. A 45° chamfer would be used for this study as it had been shown to produce successful results by Curtis [33], Duckett [14] and Fernie [34].

## 2.2.5 Test Conditions

### Rate Effects

The literature discussed previously has concentrated on the quasi-static testing of composites and has shown that specific energy absorptions of up to 227kJ/kg [21] can be achieved from circular tubes crushed axially. It is also important to consider how the test rate affects the mechanical properties of the material and the subsequent energy absorption.

### Mechanical Properties

Okoli [35] considered the effect of strain rate on the energy absorbed in woven glass/epoxy laminates. Tensile, shear and 3-point bend tests were conducted at

increasing rates of strain. Tensile specimens were tested at rates between 0.017 and 100 mm s$^{-1}$ and expended energy was seen to increase by 17% per decade increase in logarithmic strain. This increase was attributed to the failure modes of the specimens. At higher test speeds the matrix yielding increased, playing a greater part in the fracture process thus, more energy is expended during fracture. The shear tests were conducted at test speeds between 0.008 and 0.833 mm s$^{-1}$ and the shear energy to failure was found to increase by 5.9% per decade increase in logarithmic strain rate. Again the increase was attributed to greater matrix yielding at the higher test speeds resulting in fibre pull-out and an increased shear energy to failure. The 3-point bend tests were conducted at crosshead rates of between 0.017 and 8.35 mm s$^{-1}$ and the flexural energy to failure increased by 8.5% per decade increase in logarithmic strain rate.

Gilat et al [36] examined the strain rate behaviour of carbon/epoxy composites in tension. Quasi-static and intermediate strain rates of $5 \times 10^{-5}$ and 1 s$^{-1}$ were conducted on a hydraulic Instron test machine and high strain rate tests of approximately 400 to 600 s$^{-1}$ on a tensile split Hopkinson bar apparatus. Tests were carried out on pure resin samples and carbon/epoxy samples with layups of 90°, 10°, 45° and [±45°]s. The epoxy resin was toughened with unspecified thermoplastic components in order to improve its ductility. In all configurations tested, higher stiffness was observed with increasing strain rate. Only a small increase in the maximum stress was seen in the tests of pure resin, the 90° and 10° samples. A more significant effect of the strain rate was observed for the 45° and [±45°]s specimens. The highest strains, irrespective of strain rate were seen in the [±45°]s samples, implying that the sensitivity to strain rate was driven by the matrix properties.

Tensile tests at speeds between 0.017 and 2000 mm s$^{-1}$ were conducted by Okoli and Smith [37] to examine the effect of rate on the Poisson's ratio. The materials tested were glass/epoxy with a fibre layup of [0/90], 18 layers of glass and a volume fraction of 70%. Over the strain rates tested it was found that there was little variation in the Poisson's ratio with all tests producing a value of either 0.15 or 0.16. This was attributed to the presence of fibres in the composite.

Fernie [34] conducted in-plane testing of glass CoFRM/polyester and braided carbon/vinylester comparing the tensile and compressive, tensile and compressive failure stresses and moduli at test rates between 0.5mm/min and 7m/s. The glass/polyester samples showed increases of 115% and 44% in tensile failure stress and moduli respectively. Compressive failure stress and moduli were also shown to increase by 108% and 26%. The braided carbon samples with fibre lay-ups of ±30°, ±45° and ±60° were also found to have an increase in tensile and compressive properties as the test rate increased. Samples containing more axially aligned fibres (±30°) showed lower rate sensitivity. The effects of the test speed on the mechanical properties were attributed to rate sensitivity of the matrix.

*Energy Absorption*

Berry and Hull [38] crushed tubes manufactured from woven glass cloth and epoxy resin at speeds ranging from $1.67 \times 10^{-7}$ m/s to 10 m/s. They found that at all speeds the tubes crushed progressively and there was no change in the failure mode. However, as the speed of the crush increased the SEA was seen to increase proportionally with the crush speed from 33.5kJ/kg up to 74.9kJ/kg for the highest rates.

Farley [39] investigated the crush of carbon/epoxy and Kevlar®/epoxy tubes with ply orientations of $[0/\pm\theta]_2$ and $[\pm\theta]_3$ (where $\theta = 15°$, 45° and 75°) at speeds between 0.01m/sec and 12m/sec. The energy absorption of the $[0/\pm\theta]_2$ carbon specimens was not a function of the crushing speed and all specimens crushed in a brittle fracturing mode. The 0° plies had reduced the strain rate effects of the mechanical response. The energy absorption of the $[\pm\theta]_3$ carbon samples showed a weak function of crushing speed. As the ply angle increased the magnitude of the effect of the crushing speed increased. The Kevlar® specimens all failed in a local buckling mode and the energy absorption was a function of the crushing speed. Energy absorption increased by between 20% and 45% for both fibre architectures with the samples containing more fibres in the load direction providing the most significant increase. It was concluded that the energy absorption capacity would be rate sensitive if the mechanical properties controlling the energy absorption, fibres or resin, were rate sensitive. In this case the $[0/\pm\theta]_2$ carbon samples displayed no rate effect as the fibres dominate the

energy absorption and are not rate sensitive themselves. The largest changes in energy absorbed with rate were seen in the Kevlar® samples with axial fibres and a fibre orientation of 15° suggesting that Kevlar® is rate sensitive. The buckling failure mode exhibited here is controlled by plastic yielding, under compression, of the fibre and/or the matrix [1]. Hence, these results imply that the compressive strength of Kevlar® is rate dependant.

Thornton [8] crushed carbon/epoxy and glass/epoxy tubes at crush speeds between 2.54mm/min and 8.47m/s. Little change was seen in SEA, although at higher test rates the load/compression curve became more serrated.

Ramakrishna [40] investigated the energy absorption of knitted glass fibre fabric/epoxy and knitted carbon fabric/epoxy composite tubes. Tubes were tested both quasi-statically at 0.001m/s and dynamically at 13m/s using a 3kJ catapult rig. As the volume fraction increased, the SEA increased but as the test changed from quasi-static to dynamic the SEA decreased by 20%. This was attributed to several reasons. Firstly, the mode I fracture toughness ($G_{IC}$) decreases with increasing test speed [41][42] and this decreased fracture toughness means lower resistance to the longitudinal cracking of the tube wall and hence lower energy absorption. The debris and fronds were also smaller in the dynamic tests. The fine debris is associated with extensive microfracturing, which would result in a higher SEA. However, the smaller fronds indicate a reduction in frictional forces between platen and fronds. Fairfull and Hull [6] had shown experimentally that friction contributes to approximately 60% of the total energy absorption. Therefore the lower SEAs seen in the dynamic tests here were attributed to lower frictional forces during crush.

Hamada and Ramakrishna [43] tested tubes under two conditions, firstly at quasi-static speeds of $1.67 \times 10^{-5}$ m/s using a servo hydraulic machine and secondly at dynamic speeds of 8.5m/s using a drop-weight testing machine (see Figure 2-15). Tubes were manufactured from unidirectional carbon and PEEK with fibre orientations of 0°, ±5° and ±10°. The quasi-statically tested tubes all absorbed just over double the energy of those tested dynamically, for all fibre orientations. The highest values were seen for the ±10° samples with an SEA of 225kJ/kg for the quasi-

static tests and 100kJ/kg for the dynamic tests. The difference in SEA was attributed to changes seen in the crush zone morphology. The dynamically tested tubes developed large axial cracks, had fewer fibre fractures and did not have well defined fronds or a debris wedge.
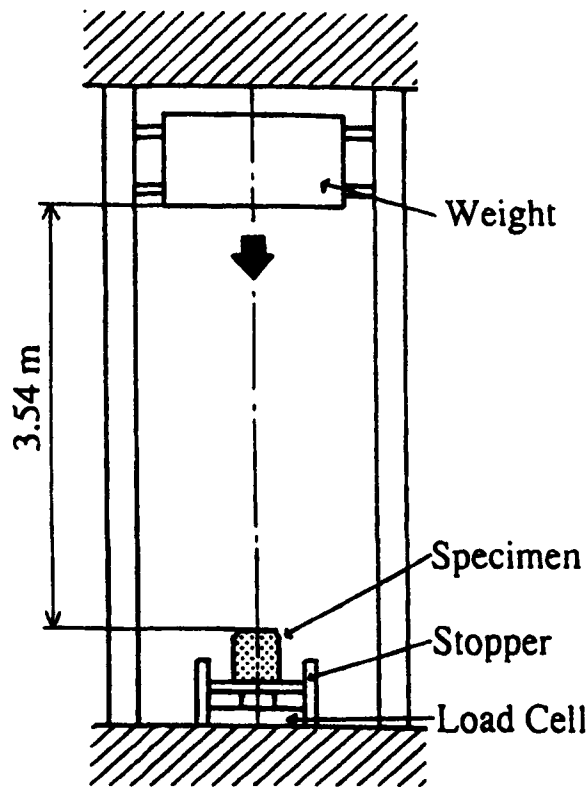


**Figure 2-15 – Schematic diagram of drop tower used by Hamada and Ramakrishna [43]**

*Crushing Surface*

Fairfull and Hull [44] considered the frictional processes that occur in the crush zone and the interactions between fracture and friction that lead to the overall level of energy absorption. This was investigated by crushing glass/epoxy tubes against four hardened steel platens of different surface roughness. The four surface finishes were a ground surface (Ra 0.4μm), produced in a precision toolroom, a polished surface (Ra 0.2μm), produced by hardening, grinding and polishing, a sandblasted finish (Ra 1μm) and a cross-milled surface (Ra 3.2μm) produced by milling perpendicular rows of grooves. The ground surface finish gave the highest SEA with the sandblasted and cross-milled finishes only slightly lower. The smoothest, polished finish gave an SEA typically 7% lower than the ground surface, which was consistent with there being less resistance to the fronds sliding across the surface. In conclusion, increasing

surface roughness could increase SEA up to a point, beyond which debris becomes embedded in the surface and effectively reduces the coefficient of friction for the remainder of the crush. It was also concluded that the various frictional processes account for more than 50% of the total energy absorption of glass cloth/epoxy tubes compared to 60% found by Fairfull and Hull [6].

Farley et al [45] tested the effects of crushing surface on the energy absorption of graphite and glass-epoxy tubes. A wide variety of fibre/matrix combinations with fibre orientations of $[\pm\theta]_6$ and $[0/\pm\theta]_4$ were used on two different crushing surfaces. The first, smooth surface, was polished using a diamond impregnated polishing wheel and the second, rough surface, was glass bead blasted. Roughness was measured using a stylus tracing Perthometer and the average roughness was 0.3μm for the smooth surface and 12μm for the rough. It was found from the tests that only tubes which failed by lamina bending were affected by the crushing surface roughness. Tubes that failed in other modes were not influenced because their lamina bundles do not slide against the crushing surface. For those tubes failing in lamina bending the energy absorption could increase, decrease or remain unchanged as the crushing surface roughness increased, and was dependent on the relative strains to failure of the fibres and matrix. If the fibre failure strain were greater than the matrix failure strain then energy absorption increased with surface roughness. If the fibre failure strain was less than the matrix failure strain then energy absorption decreases with increased surface roughness. Finally, energy absorption capabilities remained unchanged by surface roughness when the fibre and matrix failure strains were equal.

## 2.3 Effect of Damage on Impact Performance of Composite Structures

Abrate [46] summarised impact on composite structures by considering impact testing, damage assessment and the residual properties of composites. Three types of impact tests were identified, the gas gun, drop weight and pendulum. To replicate flying debris, i.e. that of a small load at high velocity, the best simulation would be the gas gun. Compressed air is released from a chamber and a projectile being fired at the sample being impacted. A simple LED and photodetector measure impact velocity. For simulation of impacts involving large masses and low velocities the drop weight or pendulum tests are preferred. The drop weight test was identified as the

most common test and involves masses, sometimes guided by rails, being dropped from a known height. The pendulum tests are used to generate low velocity impacts and use a steel ball swung from a cord or a cantilevered beam.

Impact damage consists of delaminations, matrix cracking and fibre failures. Delaminations may significantly reduce the flexural strength of a laminate. When characterising the damage zone it is most common to measure the area of the delaminations. Thresholds of impact are taken from the onset of delamination and the size of delaminations increases linearly with energy levels above the threshold. Matrix cracks develop due to either excessive transverse shear stress or when normal stresses exceed the transverse tensile strength of the ply. It is generally accepted that damage is initialised by matrix cracks and then these cracks induce delaminations at ply interfaces. Fibre failure is the last event and follows delamination in larger impacts.

In terms of testing impacted samples, the residual strength has been tested in tension, compression, shear and bending. The most common tests to be performed are the compression and tension tests.

Compression is critical for impact damaged specimens because under this type of loading, strength reductions are the largest. Several test procedures have been described to measure the compression after impact (CAI) strength with the most commonly used being the NASA 1142 (1985) and Boeing BSS 7260 (1982). CAI tests can be expensive as they use relatively large coupons, requiring costly machining and high capacity test equipment. For example, for a material which has an undamaged strength of 400MPa the NASA procedure would require 452kN force and the Boeing around 200kN. Caution is needed when using results in component design as the CAI strength depends on size of delaminations and smaller damage areas lead to smaller reductions in residual strength.

Experimental studies on the residual tensile strength show that the fibre strength and strain to failure have significant effects on the tensile strength of both damaged and undamaged samples. The impact damage remains relatively insignificant with just matrix cracks and delamination, but when fibre failure occurs, the residual tensile strength becomes significantly lower.

Doyum and Altay investigated the types and characteristics of defects produced by low-velocity impacts on glass/epoxy tubes [47]. Impacts ranging from 3.5J to 8.5J were considered by dropping a 0.5kg, hemispherical nosed impactor from various heights. The test set-up is shown in Figure 2-16 and specimens had a diameter of 79mm and a wall thickness of 3mm. Up to 7.36J, damage was localized at the impact point and the severity of the damage increased with increasing energy. Above 7.36J, cracks formed circumferentially around the tubes up to lengths of 25mm.
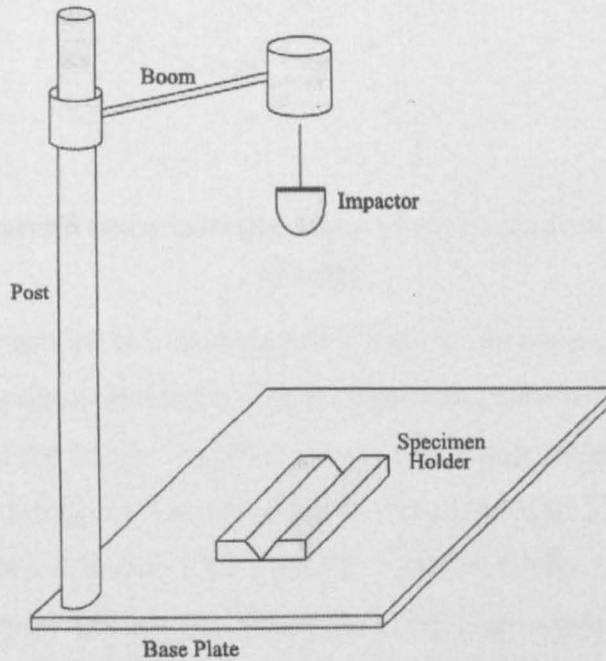


**Figure 2-16 – Drop weight impact set-up used by Doyum and Altay [47]**

Freitas and Reis [48][49] performed CAI tests on composite panels made from unidirectional prepregs of carbon fibres IM7 or T800 in epoxy resins. 24 plies were used for both composite materials with 4 stacking sequences:

Layup B: $[-45_3/0_3/+45_3/90_3]_s$

Layup C: $[-45/0/+45/90/-45_2/0_2/+45_2/90_2]_s$

Layup D: $[-45_4/+45_4/0_3/90]_s$

Layup E: $[-45_3/+45_3/0_5/90]_s$

Impact damage was applied using a falling weight impact machine with an impactor of 16mm in diameter with masses of between 2 and 10kg and a variable height up to 2m. Compression after impact tests were carried out at 0.5mm/min using the test fixture shown in Figure 2-17.
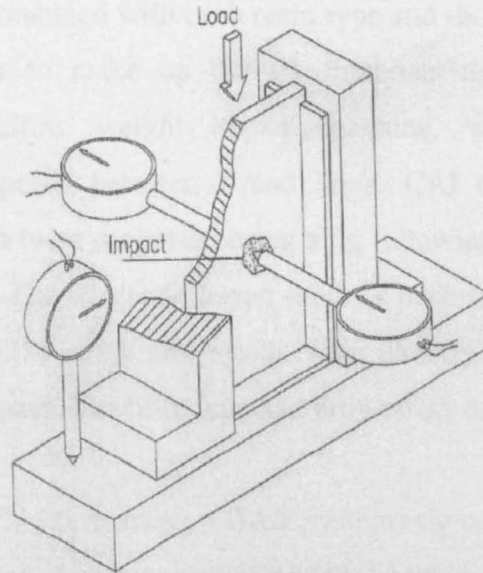
**Figure 2-17 – Instrumented compression after impact (CAI) testing fixture used by Freitas and Reis [48]**

The samples were clamped at both ends and simply supported at the edges to prevent global buckling during compression. The damage area increased linearly to 25J and was independent of the layup. Unstable growth was noted during compression after impact due to a buckling mechanism in the delaminated area. It was concluded that the delaminated area influences the residual strength of the material, which is a function of the impact energy and the failure load was dependent on fibre layup whereas the strain to failure was not.

Cartié and Irving investigated the effect of resin and fibre properties on impact and compression after impact performance of CFRP [50]. Six different carbon/epoxy composites were used for the study and Table 2-1 summarises the properties of the resins and fibres used.

| Properties | 922 resin | 914 resin | 924 resin | 920 resin | HTA Fibres | IMS Fibres |
|---|---|---|---|---|---|---|
| Tensile Strength (MPa) | 56 | 47.7 | 65 | 34.9 | 3400 | 5400 |
| Tensile Modulus (GPa) | 4.05 | 3.9 | 3.8 | 3.76 | 238 | 295 |
| Tensile Strain (%) | 1.7 | 1.4 | 2.4 | 8.41 | 1.4 | 1.7 |
| Poisson Ratio | 0.38 | 0.41 | 0.41 | 0.39 | | |
| Compression Strength (MPa) | 196 | 180 | 175 | 290 | | |
| Toughness $G_{IC}$ (J/m$^2$) | 51 | 103 | 150 | 541 | | |
| $T_g$ (°C) | | 190 | 190 | 107 | | |

**Table 2-1 – Properties of the materials used by Cartié and Irving for their CAI tests [50]**

The HTA fibres were combined with each resin type and the IMS fibres with the 924 and 922 resin systems to make up the six materials tested. Impact tests were conducted using a falling weight impact machine, with a 16mm diameter hemispherical tip at speeds between 1 and 3m/s. CAI tests were performed at 0.5mm/min and samples were supported using a jig following the Boeing standard for CAI recommendations. The 920 resin based samples performed best in the CAI tests and the 922 specimens the worst and results were directly related to the amount of damage obtained by impact. The fibre type had little effect on the CAI strength.

Habib [51] performed CAI tests using a BAE Systems rig on T300/914 carbon/epoxy laminates. 4, 6 and 8mm laminates were tested, with varying amounts of impact damage between 4.5J and 70J. A threshold was found for each laminate at which the damage area would contain delamination. Three levels of impact were then selected for each laminate, one at the threshold level, another at twice that amount and a third at two and half times. Table 2-2 shows the impact energies and subsequent size of damage area for each of the laminates tested.

| Plate Thickness (mm) | Impact Energy (J) | $T^*$ Multiple | Damage Area ($mm^2$) |
|---|---|---|---|
| 4 | 4.5 | 1 | 380 |
| | 9 | 2 | 543 |
| | 11.25 | 2.5 | 552 |
| 6 | 15 | 1 | 79 |
| | 20 | 2 | 1252 |
| | 25 | 2.5 | 1378 |
| 8 | 28 | 1 | 71 |
| | 56 | 2 | 2205 |
| | 70 | 2.5 | 2266 |

$T^*$ - Threshold Energy

**Table 2-2 – Impact energies and damage areas for laminates tested by Habib [51]**

The damaged area increased with increasing impact energy and tended to level off at a certain energy level. From the CAI tests it was found that the threshold impact energy

did not affect the results of the 6 and 8mm laminates. All other tests were significantly affected with samples failing by buckling and causing low CAI strengths.

Sjögren et al [52] investigated the elastic properties of impacted carbon/epoxy laminates. 16-ply and 48-ply laminates were manufactured from Hexcel HTA/6376C prepreg and subjected to impact from a 7.5mm radius impactor. The 16-ply samples were impacted at 8J, the 48-ply samples at 30J. Tensile and compression tests at 0.5mm/min were performed on specimens cut from three distinct regions of the laminate. The undamaged material was designated Region I, the region with mainly delamination Region II and the most damaged region, containing matrix cracks, delamination and fibre breakage, Region III. The effects of the impact damage on the tensile and compressive moduli are shown in Figure 2-18.
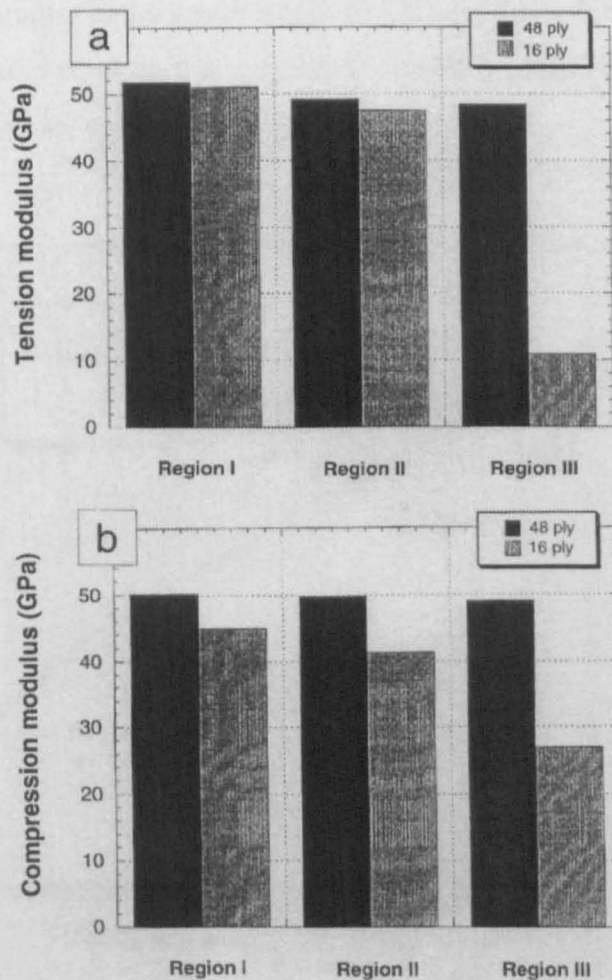


Figure 2-18 – Axial moduli for the impacted laminates tested by Sjögren et al [52]

The tensile modulus was reduced by almost 80% in the most damaged region (Region III) of the 16-ply laminate, but only by 6% in the 48-ply laminate. This difference was attributed to more broken fibres in the thinner laminate. The decrease in modulus of specimens from Region II was relatively small for both the 16 and 48-ply specimens and it was concluded that delaminations only had a minor effect on the elastic modulus. It was also stated that the moduli were mainly controlled by fibre breakage in tension and compression but, was less detrimental to the compression modulus. This was due to the fact that the broken fibres could still sustain some load in compression.

Nakai et al [53] performed tensile tests on braided glass/epoxy samples containing a braided hole and a machined hole. The braided hole was fabricated by inserting a Teflon® pin in the centre during the braiding process and the machined holes made by drilling. The samples had a gauge length of 120mm, the hole was 6mm in diameter and tensile tests were conducted at a speed of 1mm/min. Figure 2-19 shows the load-displacement curves for the three samples tested.
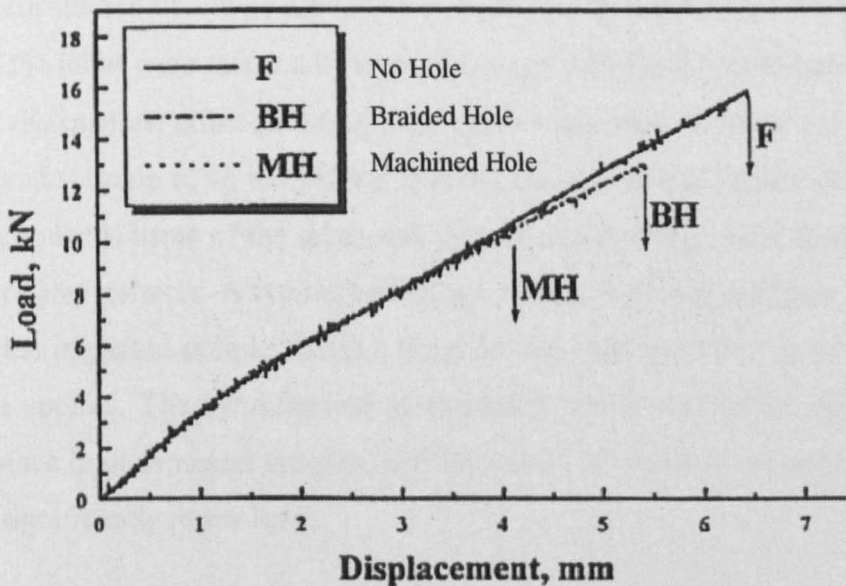


**Figure 2-19 – Load-displacement curves for the tensile tests of braided glass/epoxy samples containing holes conducted by Nakai et al [53]**

The results showed that the specimens all had the same modulus but the holes caused lower failure loads with the braided hole being 17% lower than the standard specimen

and the machined hole 36% lower. The failure mechanisms were also different. In the machined hole specimen failure occurred around the hole whilst failure occurred away from the braided hole.

The effect of post-impact crush of hybrid braided composite tubes was investigated by Karbhari et al [54]. Tubes manufactured from various hybrids of carbon, glass and/or Kevlar® yarns in a vinylester matrix were subjected to a 25J impact. Fibre orientations of [±45°] and [0°±45°] were tested with samples containing the same or a mixture of fibre types. Samples had a diameter of 55.9mm and a 2.5mm wall thickness. Impacts were centred at 63.5mm from the chamfered edge of the tube and a 19.05mm diameter impactor used to create the damage. The test speed was 25.4mm/min and samples were tested with and without impact damage and their SEAs compared. Overall damage area was measured for each sample and it was found that most of the damage was concentrated in the outermost, resin rich layers with little through thickness damage. The damage area decreased with an increase in the number of layers of braid used, and the highest level of damage was seen in the all-carbon samples. Overall the triaxially braided samples showed larger damage areas due to greater propagation of energy along the axial yarns. Upon testing it was found that the SEAs of the tubes were reduced by impact damage with the Kevlar® based specimens showing the smallest effect (30kJ/kg). The carbon specimens showed the largest drops of energy absorption of up to 68kJ/kg. Overall, the presence of impact damage altered the failure mechanisms of the tubes and there was very little stable formation of full fronds or splay patterns. A typical pair of test results is shown in Figure 2-20. As can be seen the impacted sample shows a large drop in load level due to the damage that has been applied. The hybridisation of materials, which showed an improvement in performance in undamaged samples, still improved the crush of the impacted samples but at a significantly lower level.
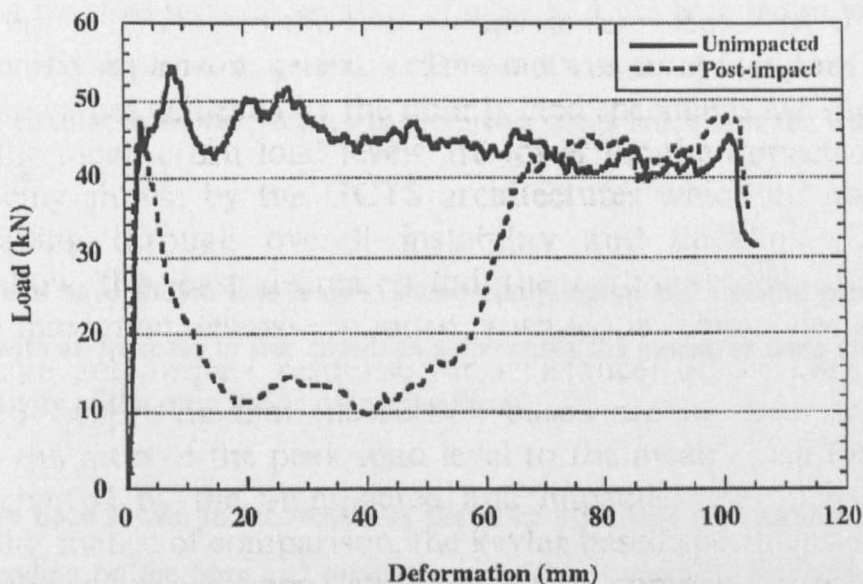
**Figure 2-20 – Comparison of the crush response of an undamaged and impacted glass/carbon braided tube tested by Karbhari [54]**

## 2.4 Conclusions

It has been shown that a large number of parameters have an effect on the crush behaviour and energy absorbing properties of composite tubes. In some cases contradictory observations have been made on the effect of these parameters, which may be due to other unforeseen or unobserved parameters having an effect.

When considering the SEA, carbon based samples have shown to be most effective, followed by glass and finally Kevlar®. The carbon and glass samples generally failed in the splaying mode and the larger SEAs are due to better mechanical properties. Kevlar® samples generally produce lower SEAs due to failing predominantly by buckling. It has been shown that a splaying failure is important in promoting high SEA levels. When comparing matrix type it has been shown here that the property that has largest effect on the SEA is fracture toughness.

Fibre volume fraction has been shown to have a large effect on SEA. If there are a large percentage of axial, load bearing fibres in the structure, then SEA increases with an increase in volume fraction. However, a reduction in SEA is seen when the matrix controls the energy absorption. It has also been shown that a volume fraction of over 15% is required for stable crush to occur.

By varying the cross-sectional geometry of tubes SEA has been shown to increase, decrease or stay the same. In general, a t/D ratio of over 0.015 is required for stable crush and circular tubes were shown to produce a stable crush over the widest range of t/D ratios.

Coupon tests have shown that tensile, shear, compressive and flexural properties all increase with an increase in test speed. In some cases the increases were attributed to rate sensitivity of the resin and in others the fibres.

SEAs have been shown to increase, stay the same or reduce with an increase in test rate, depending on the fibre and matrix combination. Generally, Kevlar® and glass reinforced tubes showed an increase in SEA as test rate increased whilst carbon reinforced samples showed a decrease or no change in energy absorption.

When composite materials are subjected to impacts, either from a gas gun, pendulum or drop weight, significant reductions in residual tensile and compressive strengths were recorded. Smaller impacts caused matrix cracking and delaminations and had relatively insignificant effects on the residual properties. As the impacts increased and caused fibre failure as well, the residual properties became significantly lower. The effect of impacts leading to fibre breakage was more detrimental to the tensile properties as the broken fibres could still sustain some load in compression.

The work in this thesis will concentrate on varying fibre architecture, specimen geometry and loading rate with an aim of identifying their effects on the energy absorption potential of composite tubes.

Minimal research has been seen of the effects of damage on the overall energy absorption. Therefore, various damage types will be simulated and threshold values of damage will be identified, below which, SEAs will be unaffected.

## 2.5 Chapter 2 References

[1] Farley GL and Jones RM, Crushing Characteristics of Continuous Fibre-Reinforced Composite Tubes, Journal of Composite Materials, Vol.26, No.1, pp37-50, 1992.

[2] Farley GL and Jones RM, Analogy for the Effect of Material and Geometrical Variables on Energy Absorption Capability of Composite Tubes, Journal of Composite Materials, Vol.26, No.1, pp78-89, 1992.

[3] Farley GL, Energy Absorption in Composite Materials for Crashworthy Structures, ICCM VI, pp3.57-3.66, July 1987.

[4] Farley GL, Relationship Between Mechanical-Property and Energy-Absorption Trends for Composite Tubes, NASA Technical Paper 3284, pp1-13, December 1992.

[5] Hull D, A Unified Approach to Progressive Crushing of Fibre-Reinforced Composite Tubes, Composites Science and Technology, Vol.40, pp377-421, 1991.

[6] Fairfull AH and Hull D, Energy Absorption of Polymer Matrix Composite Structures: Frictional Effects, Symposium on Structural Failure, ed. Wierzbicki T and Jones N, Chapter 8, pp255-279, Wiley, Chichester, June 1988.

[7] Farley GL and Jones RM, Prediction of the Energy-Absorption Capability of Composite Tubes, Journal of Composite Materials, Vol.26, No.3, pp388-404, 1992.

[8] Thornton PH, Energy Absorption in Composite Structures, Journal of Composite Materials, Vol.13, pp247-262, 1979.

[9] Thornton PH and Edwards PJ, Energy Absorption in Composite Tubes, Journal of Composite Materials, Vol.16, pp521-545, November 1982.

[10] Hamada H and Ramakrishna S, Effect of Fiber Material on the Energy Absorption Behavior of Thermoplastic Composite Tubes, Journal of Thermoplastic Composite Materials, Vol.9, No.3, pp259-279, July 1996.

[11] Farley GL, Effect of Fiber and Matrix Maximum Strain on the Energy Absorption of Composite Materials, Journal of Composite Materials, Vol.20, pp322-334, 1986.

[12] Farley GL, Energy Absorption of Composite Material and Structure, Proceedings of the 43rd American Helicopter Society Annual Forum, Vol.2, pp613-627, 1987.

[13] Chiu CH, Lu CK and Wu CM, Crushing Characteristics of 3-D Braided Composite Square Tubes, Journal of Composite Materials, Vol.31, No. 22, pp2309-2327, 1997.

[14] Duckett M, PhD Thesis, Rate Dependant Effects on the Energy Absorption and Material Properties of Polymer Composites, University of Nottingham, 2001.

[15] Farley GL, Energy Absorption of Composite Materials, Journal of Composite Materials, Vol.17, pp267-279, 1983.

[16] Karbhari VM, Falzon PJ and Herzberg I, Effect of Braid Architecture on Progressive Crush of Composite Tubes, 41st International SAMPE Symposium, No.2, pp1409-1416, March 1996.

[17] Karbhari VM, Falzon PJ and Herzberg I, Energy Absorption Characteristics of Hybrid Braided Composite Tubes, Journal of Composite Materials, Vol.31, No.12, pp1164-1186, 1997.

[18] Karbhari VM and Haller J, Progressive Crush of Hybrid Composite Components, Proc. Of 12th ESD Advanced Composites Conference, Detroit, pp1-10, April 7-10, 1997.

[19] Chiu CH, Tsai KH and Huang WJ, Crush-failure modes of 2D triaxially braided hybrid composite tubes, Composites Science and Technology, Vol.59, No.11, pp1713-1723, 1999.

[20] Satoh H, Hirakawa H, Maekawa Z, Hamada H, Nakamura M and Hull D, Comparison of Energy Absorption Among Carbon/Thermoplastic Tubes, Proceedings of the 1993 38th International SAMPE Symposium and Exhibition, Vol.38, No.1, pp952-966, May 10-13 1993.

[21] Ramakrishna S, Hamada H, Maekawa Z and Sato H, Energy Absorption Behaviour of Carbon Fibre Reinforced Thermoplastic Composite Tubes, Journal of Thermoplastic Composite Materials, Vol. 8, No.3, pp323-344, 1995.

[22] Hamada H, Coppola JC, Hull D, Maekawa Z and Sato H, Comparison of energy absorption of carbon/epoxy and carbon/PEEK composite tubes, Composites, Vol.23, No.4, pp245-252, 1992.

[23] Warrior NA, Turner TA, Robitaille F and Rudd CD, Effect of resin properties and processing parameters on crash energy absorbing composites made by RTM, Composites Part A, Vol.34, No.6, pp.543-550, 2003.

[24] Ramakrishna S and Hull D, Energy Absorption Capability of Epoxy Composite Tubes with Knitted Carbon Fibre Fabric Reinforcement, Composites Science and Technology, Vol.49, No.4, pp349-356, 1993.

[25] Hamada H and Ramakrishna S, Scaling Effects in the Energy Absorption of Carbon-fiber/Peek Composite Tubes, Composites Science and Technology, Vol. 55, No.3, pp211-221, 1995.

[26] Fairfull AH and Hull D, Effect of Specimen Dimensions on the Specific Energy Absorption of Fibre Composite Tubes, Department of Materials Science and Metallurgy, University of Cambridge, UK, Internal Conference of Composite Materials VI, July 1987.

[27] Farley GL, Effect of Specimen Geometry on the Energy Absorption Capability of Composite Materials, Journal of Composite Materials, Vol. 20, pp390-400, 1986.

[28] Farley GL, Crushing Characteristics of Composite Tubes with "Near-Elliptical" Cross Sections, Journal of Composite Materials, Vol. 26, No.12, pp1741-1751, 1992.

[29] Sigalas I, Kumosa M and Hull D, Trigger Mechanisms in Energy-Absorbing Glass Cloth/Epoxy Tubes, Composites Science and Technology, Vol.40, No.3, pp265-287, 1991.

[30] Czaplicki MJ, Robertson RE and Thornton PH, Comparison of Bevel and Tulip Triggered Pultruded Tubes for Energy Absorption, Composites Science and Technology, Vol.40, No.1, pp31-46, 1991.

[31] Jimenez MA, Miravete A, Larrode E and Revuelta D, Effect of trigger geometry on the energy absorption in composite profiles, Composite Structures, Vol.48, No.1-3, pp107-111, 2000.

[32] Hull D and Coppola JC, Performance of Glass Fibre-Vinyl Ester Composite Tubes Crushed Using Internal Mandrels, International Conference on Composite Structures, Chapter 10, pp129-143, 1991.

[33] Curtis CD, PhD Thesis, Energy Absorption and Crush Behaviour of Composite Tubes, University of Nottingham, 2000.

[34] Fernie R, PhD Thesis, Loading Rate Effects on the Energy Absorption of Tubular Crash Structures, University of Nottingham, 2002.

[35] Okoli OI, The effects of strain rate and failure modes of fibre reinforced composites, Composite Structures, Vol.54, No.2-3, pp299-303, 2001.

[36] Gilat A, Goldberg RK and Roberts GD, Experimental study of strain-rate-dependent behavior of carbon/epoxy composite, Composites Science and Technology, Vol.62, No.10-11, pp1469-1476, 2002.

[37] Okoli OI and Smith GF, The effect of strain rate and fibre content on the Poisson's ratio of glass/epoxy composites, Composite Structures, Vol.48, No.1-3, pp157-161, 2000.

[38] Berry and Hull D, Effect of speed on progressive crushing of epoxy-glass cloth tubes, Proceedings of the 3rd Conference on Mechanical Properties at High Rates of Strain, Oxford, Institute of Physics Conference Series No. 70, pp463-470, 1984.

[39] Farley GL, The Effects of Crushing Speed on the Energy-Absorption Capability of Composite Tubes, Journal of Composite Materials, Vol. 25, pp1314-1329, 1991.

[40] Ramakrishna S, Energy Absorption Characteristics of Knitted Fabric Reinforced Epoxy Composite Tubes, Journal of Reinforced Plastics and Composites, Vol. 14, pp1121-1141, 1995.

[41] Smiley AJ and Pipes RB, Rate Effects on Mode I Interlaminar Fracture Toughness in Composite Materials, Journal of Composite Materials, Vol.21, pp670-687, 1987.

[42] Friedrich K, Walter R, Carlsson LA, Smiley AJ and Gillespie Jr, Mechanisms for Rate Effects on Interlaminar Fracture Toughness of Carbon/Epoxy and Carbon/PEEK Composites, Journal of Materials Science, Vol.24, pp3387-3398, 1989.

[43] Hamada H and Ramakrishna S, Comparison of Static and Impact Energy Absorption of Carbon Fiber/PEEK Composite Tubes, Composite Materials: Testing and Design, Vol.12, ASTM STP 1274, R.B.Deo and C.R.Saff, Eds., American Society for Testing and Materials, pp182-197, 1996.

[44] Fairfull AH and Hull D, Energy Absorption of Polymer Matrix Composite Structures: Frictional Effects, Symposium on Structural Failure, ed. Wierzbicki T and Jones N, Chapter 8, pp255-279, Wiley, Chichester, June 1988.

[45] Farley GL, Wolterman RL and Kennedy JM, The Effects of Crushing Surface on the Crushing Characteristics of Composite Tubes, Journal of the American Helicopter Society, pp53-60, 1992.

[46] Abrate S, Impact on Composite Structures, Cambridge University Press, Cambridge, 1998.

[47] Doyum AB and Altay B, Low-velocity impact damage in glass fibre/epoxy cylindrical tubes, Materials & Design, Vol. 18, No. 3, pp131-135, 1997.

[48] Freitas M and Reis L, Failure mechanisms on composite specimens subjected to compression after impact, Composite Structures, Vol.42, No.4, pp365-373, 1998.

[49] Freitas M and Reis L, Damage growth analysis of low velocity impacted composite panels, Composite Structures, Vol.38, No.1-4, pp509-515, 1997.

[50] Cartié DDR and Irving PE, Effect of resin and fibre properties on impact and compression after impact performance of CFRP, Composites: Part A, Vol.33, No.4, pp483-493, 2002.

[51] Habib FA, A new method for evaluating the residual compression strength of composites after impact, Composite Structures, Vol.53, No.3, pp309-316, 2001.

[52] Sjögren A, Krasnikovs A and Varna J, Experimental determination of elastic properties of impact damage in carbon fibre/epoxy laminates, Composites: Part A, Vol.32, No.9, pp1237-1242, 2001.

[53] Nakai A, Ohki T, Takeda N and Hamada H, Mechanical properties and micro-fracture behaviors of flat braided composites with a circular hole, Composite Structures, Vol.52, No.3-4, pp315-322, 2001.

[54] Karbhari VM, Haller JE, Falzon PK and Herszberg I, Post-impact crush of hybrid braided composite tubes, International Journal of Impact Engineering, Vol. 22, No.4, pp419-433, 1999.

# 3.0 Experimental Methods

## 3.1 Introduction

It has been shown from the literature that when crushing composite tubes, many variables affect the energy absorption potential. The material type, manufacture process, geometry of the tube, test rate, pre-test damage, crush initiator, temperature and crushing surface are some of these variables. In the scope of this work it was not possible to investigate all of these and the study focussed on the effects of pre-test damage, test rate, tube geometry and fibre type on the energy absorption potential of circular composite tubes.

The objective of this work is to understand the effect of pre-test damage on the failure mode and subsequent energy absorption of glass reinforced composites. A range of simulated damage types and levels will be tested with threshold levels of damage that could be inflicted on specimens without significantly effecting their energy absorption capabilities found.

Circular tubes were manufactured and tested by axial compression (crushed), failure modes were observed and SEAs calculated. Preliminary tests were conducted on glass CoFRM/polyester tubes with an external diameter of 89.1mm and wall thickness of 4mm containing drilled holes as simulated damage. Supply of the polyester resin used in these initial tests was stopped. Further work was undertaken using a similar unsaturated polyester resin.

Larger tubes with were tested with simulated damage caused by drilled holes and drop weight impacts. The wall thickness and hence t/D ratio, was varied to investigate its effect on the damage tolerance. These large tubes exceeded the machine capabilities for dynamic studies and a smaller, 38.1mm diameter, 2mm wall thickness specimen was developed. Damage was introduced in the form of drilled holes, impact damage and simulated delamination. Quasi-static (5mm/min) tests were conducted as well as dynamic (5m/s) tests to investigate rate effects on the damage tolerance.

In order to generalise the failure modes of the tubes, stress concentration factors were calculated based on tube geometry and size of damage introduced. Tensile coupon tests of undamaged samples and those containing holes were carried out at 5mm/min and 5m/s.

Table 3-1 shows the matrix for all tube tests undertaken and the following sections discuss the manufacture and testing procedures used.

| Tube Type:<br>Test Speed: | Large<br>CoFRM/Crystic<br>5mm/min | Large<br>CoFRM/Norpol<br>5mm/min | Small<br>CoFRM/Norpol<br>5mm/min | Small<br>CoFRM/Norpol<br>5m/s | Small<br>Braid/Norpol<br>5mm/min | Small<br>Braid/Norpol<br>5m/s |
|---|---|---|---|---|---|---|
| No Damage | x | x | x | x | x | x |
| Wall Thickness | | x | | | | |
| Holes - size | x | x | x | x | x | x |
| Holes - position | | | x | x | | |
| Impact Damage | | x | x | x | x | x |
| Delamination | | | x | x | | |

**Table 3-1 – Test matrix for all tube tests**

## 3.2 Materials

*Tensile coupons and large CoFRM/Crystic tubes*

The reinforcement used was an E-glass continuous filament random mat (CoFRM), supplied by Vetrotex Ltd. It had an areal mass of 450g/mm$^2$; contained 8% thermoplastic polyester binder and product code Unifilo U750-450. The resin system was a pre-accelerated polyester based resin, Crystic 701PA, supplied by Scott Bader Ltd. Methyl Ethyl Ketone Peroxide (MEKP) Butanox M50 initiator, supplied by Akzo-Nobel, was used at 1% and gave a gel time of around 4 hours at 20°C.

*Small and large CoFRM/Norpol tubes*

The reinforcement was E-glass CoFRM as described above. The resin system used was Norpol 720-100, an unaccelerated polyester based resin supplied by Reichhold. NL49P accelerator, supplied by Akzo-Nobel, at 0.5% by weight and MEKP M50 initiator used at 1% by weight giving a gel time of around 1 hour at 20°C.

*Small Braided/Norpol tubes*

The reinforcement used for the braided tubes was Hybron 2001 roving, a 600 Tex glass tow supplied by PPG industries. The filament diameter was 12microns with a silane size at 0.55%. The Norpol resin system was used with accelerator and initiator as described above.

In comparing the two resin systems, Crystic 701PA and Norpol 420-100, the tensile moduli were comparable at 3.580GPa and 3.700GPa respectively. The strains to failure were 2.5% for the Crystic resin and 3.5% for the Norpol.

## 3.3 Specimen Manufacture

The large CoFRM/Crystic and CoFRM/Norpol tubes with a 4mm wall thickness were both manufactured using an existing mould. The layout of the mould is shown in Figure 3-7. To vary the wall thickness of the large CoFRM/Norpol tubes new inner mandrels were made. To keep the tubes comparable, the volume fraction needed to be the same for all samples. The 4mm walled samples were manufactured using 6 layers of mat, which led to 5 and 4 layered samples of wall thickness 3.33mm and 2.67mm. Mandrels were made with a ground finish.

For the small tube manufacture a new mould was designed producing an outer diameter of 38.1mm and 2mm wall thickness; see Figure 3-1 and Figure 3-2.
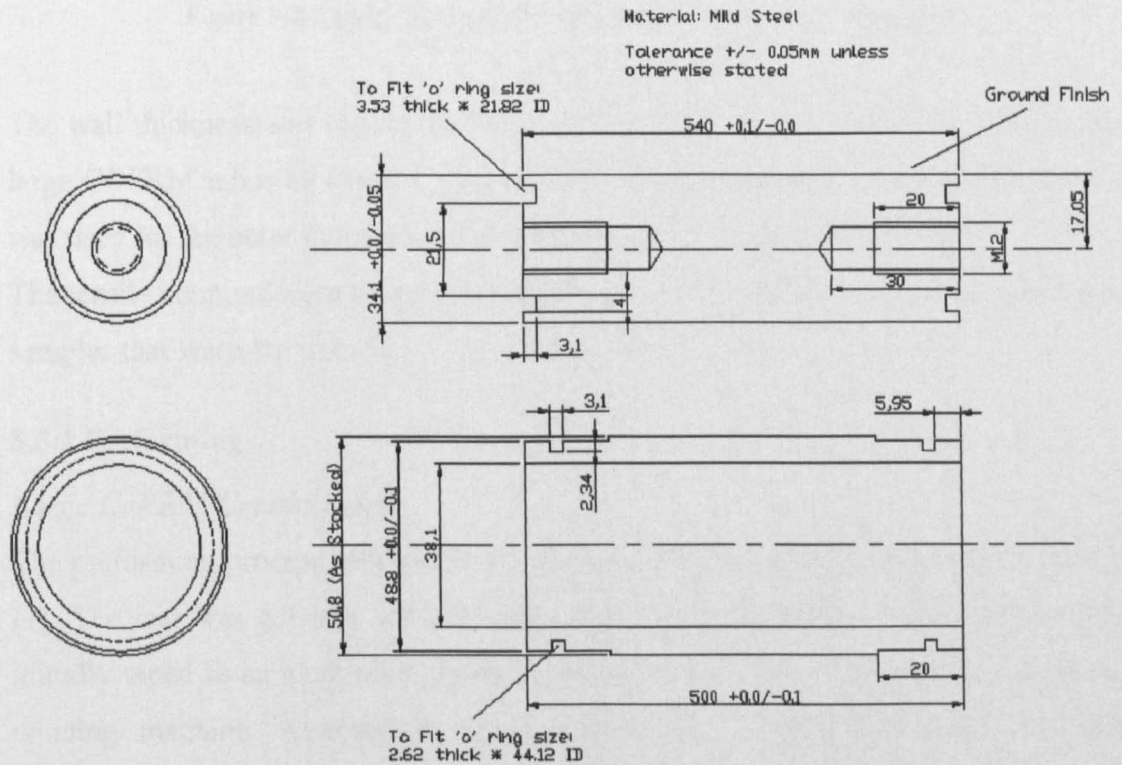


**Figure 3-1 – Inner and outer mandrel design for new tube mould (AutoCAD 2000)**
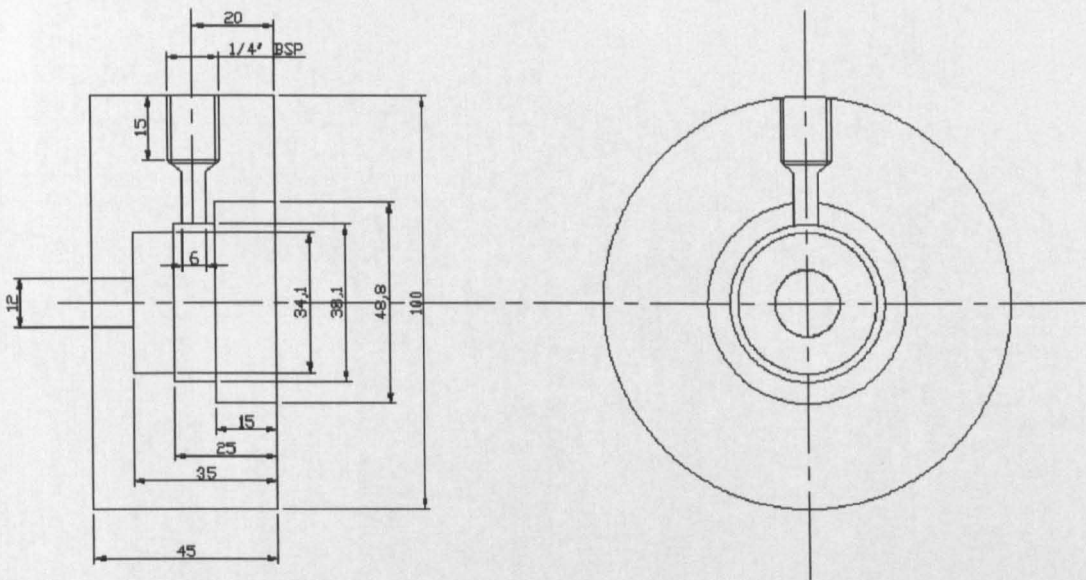
**Figure 3-2 – End Cap design for new tube mould (AutoCAD 2000)**

The wall thickness was chosen so that it would give a similar volume fraction to the large COFRM tubes by using 3 layers of mat. Bright seamless steel hydraulic tubing was used for the outer mandrel and all other parts were machined mild steel.

The tensile coupons were manufactured from an existing plaque tool, which produced samples that were 4mm thick.

### 3.3.1 Preforming

*Large CoFRM/Crystic Tubes*

The preforming process followed a pressurised roller technique developed by Corden [1]. The mat was cut into 300mm tapes ready to be preformed. These pieces were initially taped to an aluminium mandrel, which was supported in a Pultrex filament-winding machine. Attached to the machine was a pressurised roller and this compacted the fibres as they were rolled. A hot air gun was used during rolling and this melted the binder, allowing the layers to bond together as they were rolled. After six layers had been rolled onto the mandrel the preform was slid off ready for moulding. Preforms were then trimmed to 250mm in length, removing the starter tape. Figure 3-3 shows the filament winding machine, mandrel and roller and a completed preform is shown in Figure 3-4.
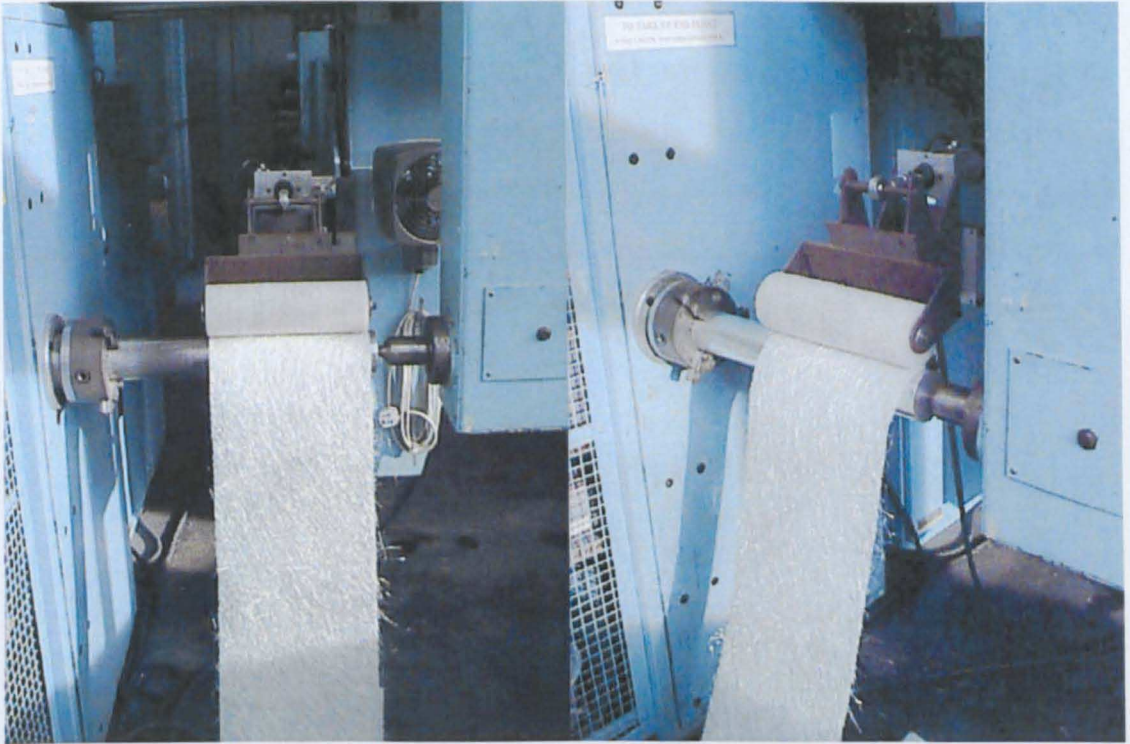
**Figure 3-3 – Filament winding machine used for performing 89.1mm diameter CoFRM/Crystic tubes (from Duckett [5])**



**Figure 3-4 – Preforms (from Duckett [5])**

### Large and Small CoFRM/Norpol Tubes

The preforming process used for the large CoFRM/Crystic tubes could not be used for the smaller design, as the inner mandrel could not be attached to the filament winding machine. Therefore a new preformer was designed and manufactured to enable mandrels of diameters from 20mm to 100mm to be used. Figure 3-5 shows the finished rig. This preformer was also used for the large CoFRM/Norpol tubes for continuity.
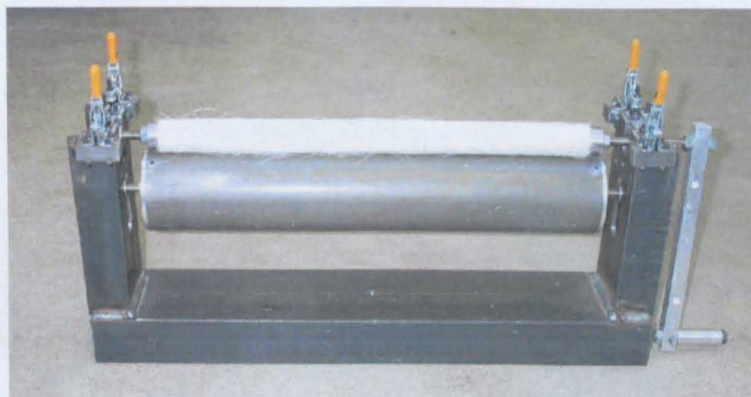


**Figure 3-5 – Hand operated preforming rig for 38.1mm diameter tubes**

For the large tubes the mat was cut to 1580mm long by 500mm wide for the 4mm wall samples, giving six layers in the mould. For the 3.33mm walled samples, 5 layers and for the 2.67mm walled samples 4 layers were used, to provide similar volume fractions for each tube type. Strips of mat were cut to 500mm wide by 340mm long for the small CoFRM tubes, allowing 3 layers to be preformed on the mandrel. The mat was heated via a blower to melt the thermoplastic binder and a hand crank allowed the mandrel to be rotated. All parts of the mould were applied with Chemlease PMR-90 between mouldings and the preforming took place directly onto the inner mandrel of the mould.

### Small Braided/Norpol Tubes

The braiding took place directly on the inner mandrel of the small tube mould, after coating with Chemlease PMR-90 mould release. The braiding machine had 48 bobbins loaded with the glass tows and the mandrel attached to it. A ±45° braid was used and 6 layers were applied to the mandrel. Figure 3-6 shows the braiding machine with the mandrel attached during the process.
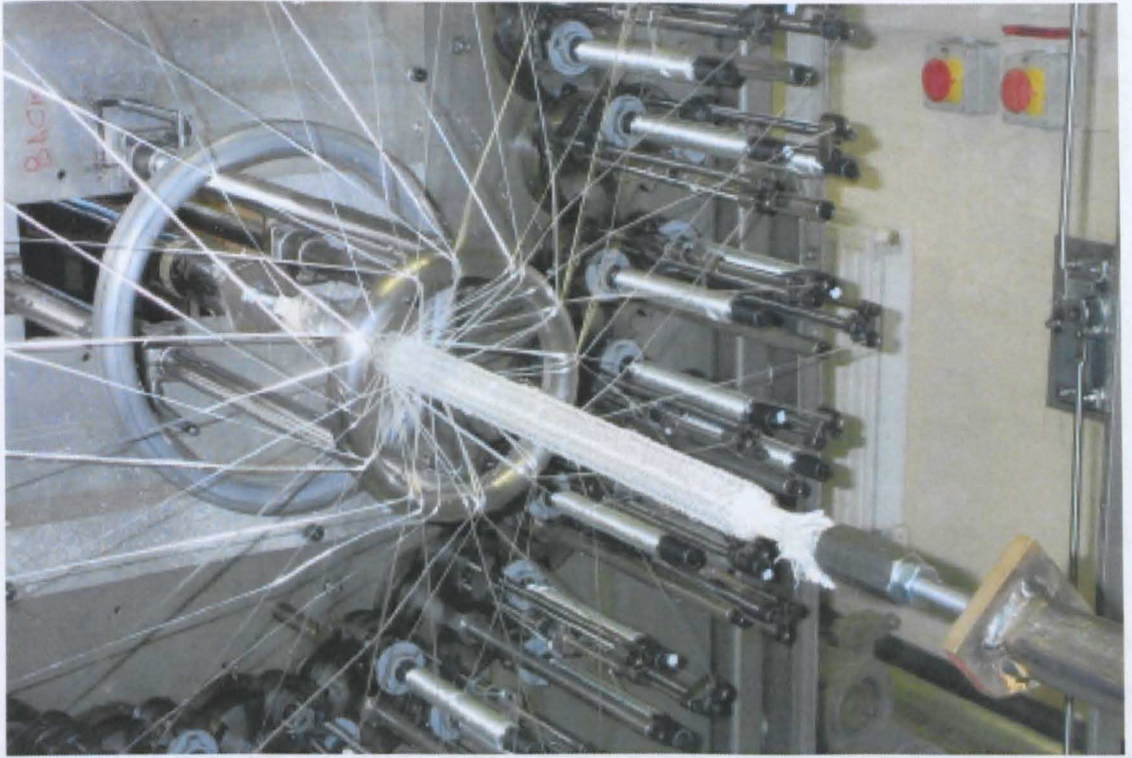
Figure 3-6 – The braiding of the 38.1mm diameter small braided tubes

*Tensile Coupons*

A Fox and Offord 50 tonne hydraulic upstroke press was used. The platens were pre-heated to 70°C and six layers of mat were stacked and compacted at 20 tonnes for 15 minutes. The preform was removed and cut to size for moulding using a Stanley knife.

### 3.3.2 Moulding

*Tensile Coupons*

An aluminium RTM tool was used with a depth of 4mm and vacuum assistance at the vent. The tool was treated with five layers of Chemlease PMR-90 polyester mould release prior to the preform being positioned. The tool was closed, with an 'o' ring seal, and clamped at the perimeter. The inlet port was connected to a pressure pot and the outlet to a vacuum pump. Resin was then injected at 0.5bar with suction at the vent. When the mould had filled the vacuum pump and pressure pump were switched off and the moulding left to cure for 24 hours at room temperature. The cured plaque was then removed from the tool and post-cured for 2 hours at 80°C.

Specimens were cut from the plaque using a diamond tipped cutting wheel. The quasi-static specimens were 210mm by 25mm and the dynamic specimens 180mm by 25mm. The difference in length was due to the grip sizes and gave a gauge length of 100mm for both tests.

*Large CoFRM/Crystic Tubes*

The tubes were processed by RTM with vacuum assistance at 2bar. The mould consisted of an internal and external mandrel with two end caps; held together with a tie rod down the centre, see Figure 3-7.
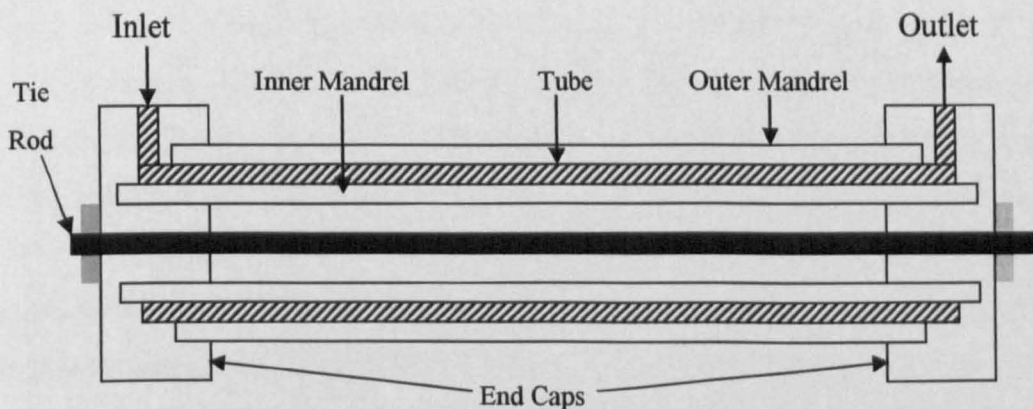


**Figure 3-7 – Mould used for the manufacture of the 89.1mm diameter tubes**

Before moulding Chemlease PMR-90 release agent was applied to all surfaces to aid in the removal of samples. Two preforms were placed end to end onto the internal mandrel and the external mandrel placed over the top before attaching the end caps and tie rod. The inlet port was connected to the pressure pot, which injects the resin and the outlet to the vacuum pump. The vacuum was turned on first and when the resin reached the inlet port the pressure pot was brought on-line at a pressure of 2 bar. When the mould had filled and resin started to flow from the outlet pipe, the vacuum was removed and the resin flushed through the mould, at 2 bar from the pressure pot, for around thirty minutes. The mould was then placed in an oven at 80°C to cure for 2 hours before de-moulding.

The samples were all post-cured for 3 hours at 80°C before being cut into 110mm lengths using a diamond tipped cutting wheel.

### *Large and Small CoFRM/Norpol and Small Braided/Norpol Tubes*

As with the large CoFRM/Crystic tubes the RTM method was used for moulding although no vacuum was applied at the outlet. The vacuum assistance was discontinued due to the lower viscosity of the Norpol resin. This allowed the moulds to fill more easily without the need for a vacuum. The moulds were otherwise prepared in the same way. The inlet was connected directly to a pressure pot containing the mixed resin and pressure applied at 2bar. The moulds filled in around 5 minutes and resin was flushed through the mould for a further 20 minutes. The mould was then left overnight for the resin to cure before being removed and post-cured at 80°C for 2 hours.

### 3.3.3 Further Preparation

Figure 3-8 shows the cutting plan used for the large CoFRM/Crystic tubes. The ends of all the tubes were discarded and the central sections used for burn off tests to calculate the volume fractions of the samples. All samples were cut using a diamond tipped cutting wheel and were 110mm long. Similar cutting plans were used for each type of tube tested. The large CoFRM/Norpol tube specimens were also 110mm long whilst the small CoFRM and braided tubes were cut to 80mm. Specimen length was chosen to allow a crush of 50mm without tube compaction. After testing the large tubes it was found that a shorter length of sample could be used, which allowed an extra sample to be taken from each mould and reduce manufacturing time.
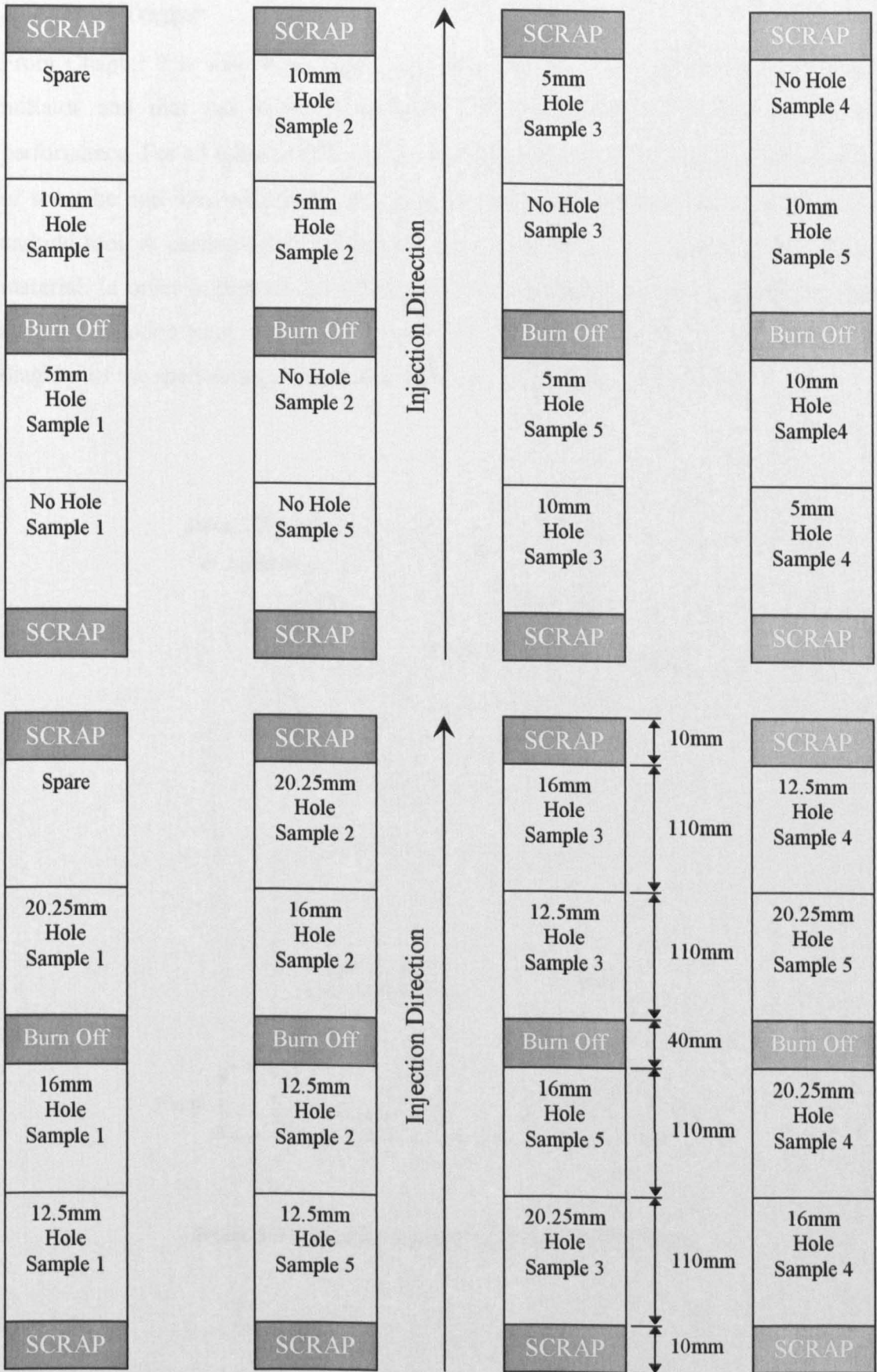
**Column 1 (top):**

| SCRAP |
|---|
| Spare |
| 10mm Hole Sample 1 |
| Burn Off |
| 5mm Hole Sample 1 |
| No Hole Sample 1 |
| SCRAP |

**Column 2 (top):**

| SCRAP |
|---|
| 10mm Hole Sample 2 |
| 5mm Hole Sample 2 |
| Burn Off |
| No Hole Sample 2 |
| No Hole Sample 5 |
| SCRAP |

**Column 3 (top):**

| SCRAP |
|---|
| 5mm Hole Sample 3 |
| No Hole Sample 3 |
| Burn Off |
| 5mm Hole Sample 5 |
| 10mm Hole Sample 3 |
| SCRAP |

**Column 4 (top):**

| SCRAP |
|---|
| No Hole Sample 4 |
| 10mm Hole Sample 5 |
| Burn Off |
| 10mm Sample4 |
| 5mm Hole Sample 4 |
| SCRAP |

Injection Direction

**Column 1 (bottom):**

| SCRAP |
|---|
| Spare |
| 20.25mm Hole Sample 1 |
| Burn Off |
| 16mm Hole Sample 1 |
| 12.5mm Hole Sample 1 |
| SCRAP |

**Column 2 (bottom):**

| SCRAP |
|---|
| 20.25mm Hole Sample 2 |
| 16mm Hole Sample 2 |
| Burn Off |
| 12.5mm Hole Sample 2 |
| 12.5mm Hole Sample 5 |
| SCRAP |

**Column 3 (bottom):**

| SCRAP | 10mm |
|---|---|
| 16mm Hole Sample 3 | 110mm |
| 12.5mm Hole Sample 3 | 110mm |
| Burn Off | 40mm |
| 16mm Hole Sample 5 | 110mm |
| 20.25mm Hole Sample 3 | 110mm |
| SCRAP | 10mm |

**Column 4 (bottom):**

| SCRAP |
|---|
| 12.5mm Hole Sample 4 |
| 20.25mm Hole Sample 5 |
| Burn Off |
| 20.25mm Hole Sample 4 |
| 16mm Hole Sample 4 |
| SCRAP |

Injection Direction

**Figure 3-8 – Cutting plan for the Large (89.1mm diameter, 4mm wall thickness) CoFRM/Crystic tubes**

### 3.3.4 Tube Trigger

From Chapter 2 it was shown that a chamfer was the most reliable form of crush initiator and that the angle of chamfer did not significantly affect the crush performance. For all tubes in this study a 45° chamfer was used as a trigger at one end of the tube and was produced using a centre lathe at 1400rpm and an inserted tip carbide tool. A cutting lubricant/coolant was not used to avoid impregnation of the material. In order to prevent overheating of the cutting area a very low feed rate was used. A wooden plug was made to support the tube walls during machining. A diagram of the specimen geometries is shown in Figure 3-9 and Figure 3-10.



89.1mm

110mm

Centre of damage
type (hole/impact)

30mm

45°
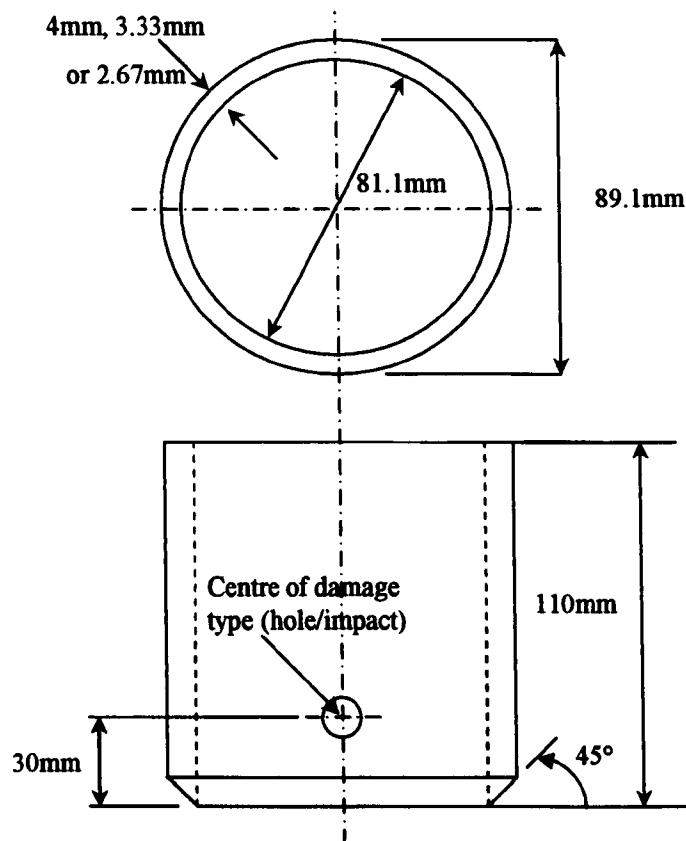
**Figure 3-9 – Specimen geometry of large CoFRM tubes**
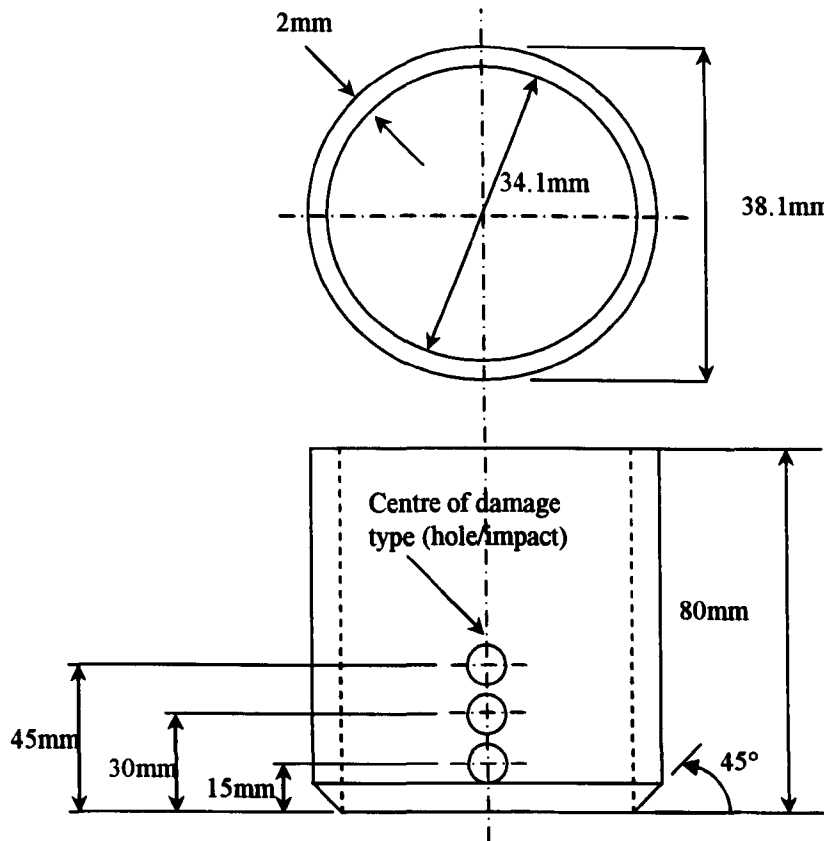
**Figure 3-10 - Specimen geometry of small tubes**

## 3.4 Damage Types/Application

Several methods of damage simulation were used; holes, delamination and impact damage.

### 3.4.1 Holes

Holes were drilled into the tubes to simulate the need to affix components to the structure or general wear and tear during service.

Composite materials are easily damaged whilst drilling and Davim and Reis [2] examined several drill types and cutting parameters for damage-free drilling of a carbon fibre reinforced epoxy composite material. A helical flute HSS drill and four-flute and helical flute cemented carbide (K10) drills were tested at various feed rates and cutting speeds. Damage was quantified by inspection of samples after drilling, looking at the areas of visible delamination around the holes. The four-flute K10 drill caused most damage with the two helical fluted drills producing similar amounts. It was also found that more damage was incurred at higher cutting speeds and feed rates.

HSS drill bits with a lip and spur cutting shape were used at 1000rpm at a feed rate of 25mm/min. The tubular samples were held in the same rig for drilling as for being impacted (see section 3.4.3). The following hole sizes and positions were used for each test type:

- **Large CoFRM/Crystic tubes:** 5mm, 10mm, 12.5mm and 20.25mm all centred at 30mm from the chamfered edge.
- **Large CoFRM/Norpol Tubes:** 5mm, 7.5mm, 10mm, 12.5mm and 16mm all centred at 30mm from the chamfered edge.
- **Small CoFRM/Norpol Tubes:** 5mm, 2×5mm, 7.5mm, 10mm, 12.5mm and 16mm at 30mm from the chamfer. 5mm and 10mm at 15mm from the chamfer and 10mm at 45mm from the chamfer.
- **Small Braided/Norpol Tubes:** 5mm, 7.5mm, 10mm, 12.5mm and 16mm all centred at 30mm from the chamfered edge.
- **Coupons:** 5mm and 10mm in the centre of the specimens.

### 3.4.2 Simulated Delamination

PET inserts were used to simulate delamination in a component, either caused during manufacture or damage during service life. Melinex® film was used and only in the small CoFRM tubes, as later results (see section 4.4.3) showed the effect on SEA to be negligible. The film was cut using a wad-punch and inserted during the preforming process. Three samples were manufactured; those containing one 32mm diameter insert, two 32mm diameter inserts and one 50.8mm insert. The inserts were between the first and second layers (from the outside) of the preform. The samples with two inserts had one placed between the first and second layers and another aligned with the first between the second and third layers. Tubes were cut so as the bottom edges of the inserts were 15mm from the chamfered edge.

### 3.4.3 Impact Damage

Impact damage was introduced using a Rosand falling weight impact test machine. The damage was applied to simulate impacts caused by stones or debris being thrown up and hitting the part, or tool drops during manufacture or servicing. An impactor was attached to the smallest weight available on the machine giving a total mass of 5.792kg. The impactor had a 12mm diameter tip and the tubes held in a fixture. The weight of the fixtures held them in place during damage application. The impactor

and fixture for the large (89.1mm diameter) tubes are shown in Figure 3-11 and for the small (38.1mm diameter) tubes in Figure 3-12.
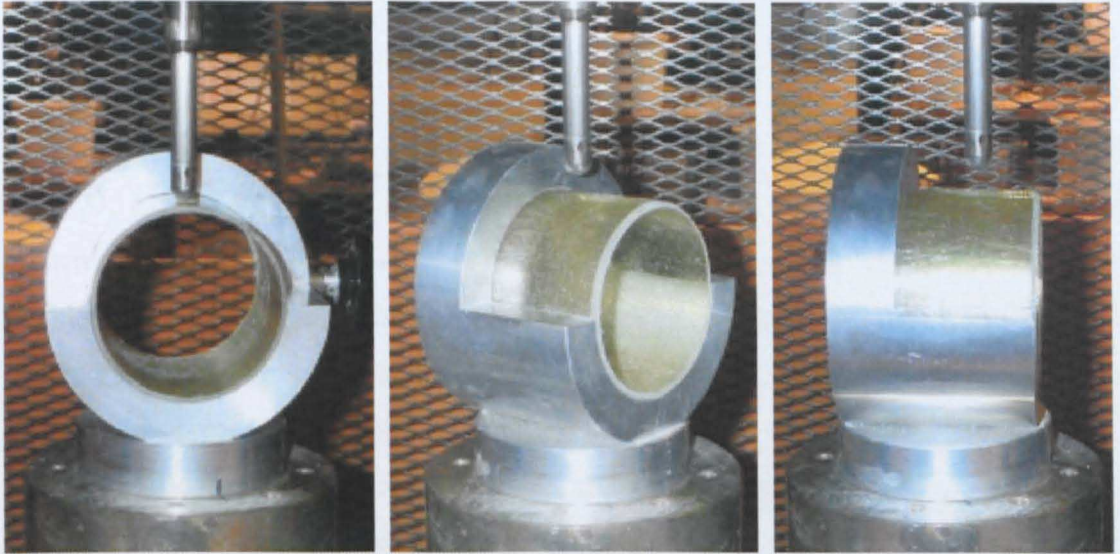


**Figure 3-11 – Fixture used to add damage to and drill large (89.1mm diameter) tubes**



**Figure 3-12 – Fixture used to add damage to and drill small (38.1mm diameter) tubes**

The distance from the chamfered edge was marked on the tube using pen and aligned with the impactor by eye. The drop heights for the impact energies were calculated as follows:

$$\text{Impact Energy} = \text{mass of impactor} \times g \times \text{drop height}$$

This led to the following drop heights for the impacts used:

| 1.5J | $\Rightarrow$ | 0.0264m |
|------|---------------|---------|
| 3J   | $\Rightarrow$ | 0.0528m |
| 6J   | $\Rightarrow$ | 0.1056m |
| 9J   | $\Rightarrow$ | 0.1584m |

The large tubes and small braided and CoFRM tubes were all tested with impacts of 1.5J, 3J, 6J and 9J centred at 30mm from the chamfer. Typical impact damage is shown in Figure 3-13 to Figure 3-15. The damage zone was determined as the area of visible delamination. Measurements were taken and the area estimated for each specimen. For most samples the damage zone could be approximated to a simple circle, ellipse or square. For more complex shapes, as with the 9J impact in the 2.67mm walled tube in Figure 3-13 below, the area was split into several elements, in this case an ellipse and two triangles.
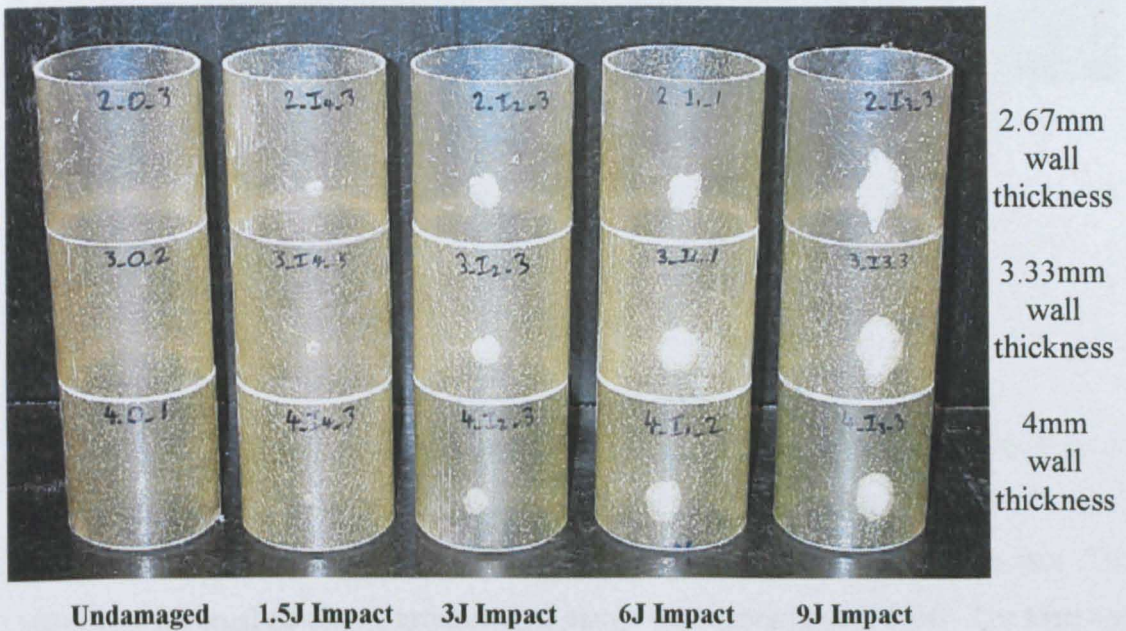


**Figure 3-13 – Impacted large CoFRM tubes pre-testing**

| 1.5J Impact | 3J Impact | 6J Impact | 9J Impact |
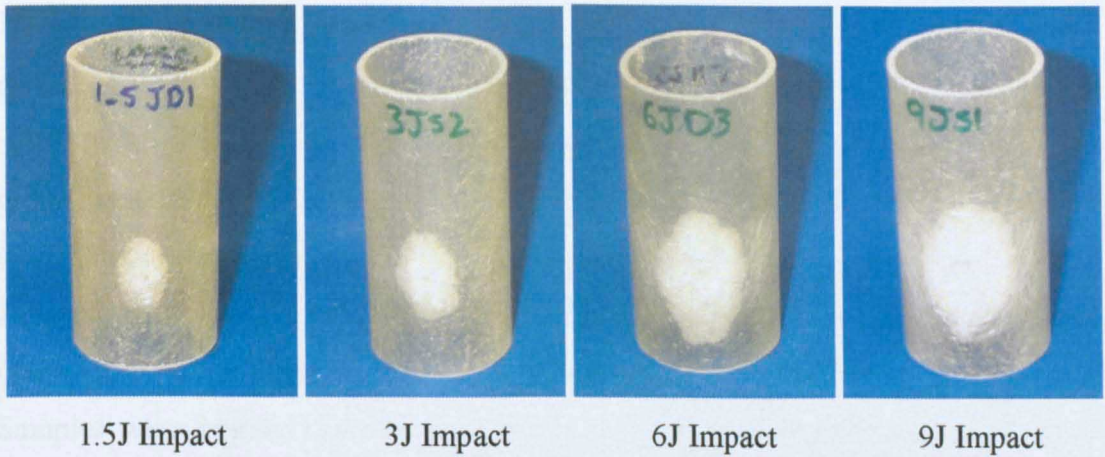
**Figure 3-14 – Impacted small CoFRM tubes pre-testing**



| 1.5J Impact | 3J Impact | 6J Impact | 9J Impact |
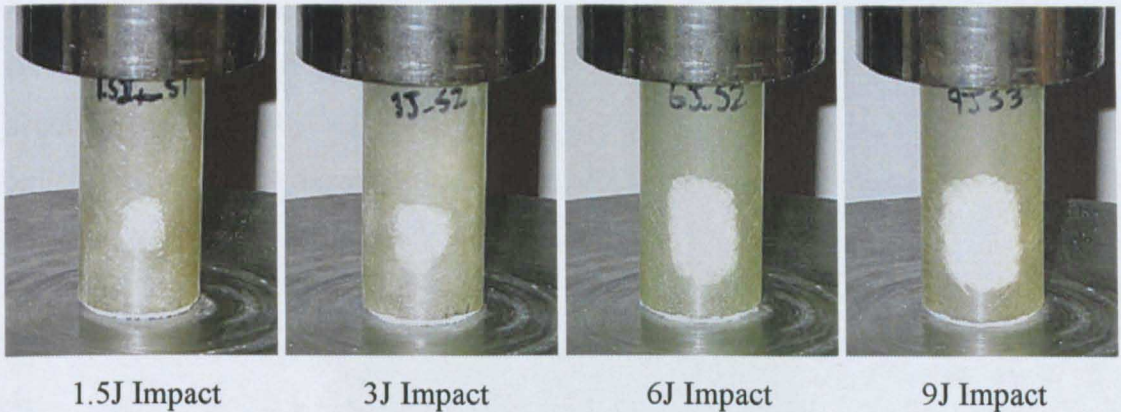
**Figure 3-15 – Impacted small braided tubes pre-testing**

## 3.5 Test Procedures

### 3.5.1 Large Tube Test Conditions

The large tubes were tested quasi-statically, at 5mm/min, on an Instron 8500 servo hydraulic test machine with a 1000kN load cell attached. Five samples for each CoFRM/Crystic tube test were used and three of each CoFRM/Norpol tube test. The samples were crushed onto a ground steel platen for a distance of 50mm. The load and displacement data was recorded directly from the Instron test machine onto a PC.

A thermal camera (AGEMA Thermovision 900) was set up on the CoFRM/Crystic samples during crush to give an indication of the heat dissipated. When a material is compressed or expanded temperature changes are experienced and higher stresses cause larger changes. The thermal camera was used here to identify the areas of stress during crush. Where pre-test damage was added, the thermal camera would also identify how the stress built up around the damage zone.

### 3.5.2 Small Tube Test Conditions

*Quasi-static* tests were conducted on an Instron 1195 test machine with a 100kN load cell. The crosshead speed was 5mm/min and tubes were crushed for 50mm onto a ground steel platen. Three tubes of each damage type were crushed and all specimens were 80mm in length and had a 45° chamfer as a trigger.

*Dynamic tests* were carried out on a Rosand IFW5 falling weight impact test machine (see Figure 3-16). The effective impactor mass was 44.65kg (without a specimen). Samples were bonded directly onto the impactor using cyanoacrylate. The fixture used for these tube tests is shown in Figure 3-17. The load data were acquired using a Kistler 9051A piezoelectric load cell with a measuring range of 0-120kN. The load cell was connected to a PC via a PCI based instruNET 100 and iNET 200 data acquisition system at a sample rate of 40000 samples/sec. A nominal test speed of 5m/s was used and three samples of each damage type were crushed using specimens 80mm in length with 45° chamfers as triggers.
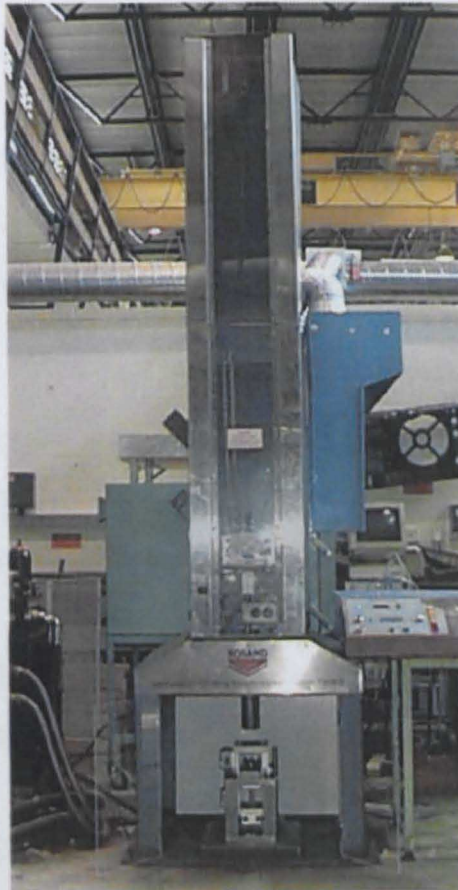


**Figure 3-16 - Rosand falling weight impact test machine**

**Figure 3-17 – Dynamic tube test rig**

### 3.5.3 Calculations

The dynamic tests produced load and time data. By knowing the start speed and calculating the deceleration (change in load/mass), the velocity at each data point could be calculated. Assuming the velocity was constant between each point the distance travelled was calculated (velocity × time). The summation of the distance travelled between each data point gave the displacement of tube crush, allowing the load displacement curve to be plotted.

The SEA was calculated from the area under the load displacement curve (giving the total energy absorbed) divided by the mass of tube that was crushed. The area under the curve was calculated using the trapezium rule and the effect of the chamfer was removed by discounting 5mm of crush from the start of the test. The mass of tube crushed was calculated from the mass per unit length of the tube and the stroke, taken from the load displacement curve. A sample calculation is shown in Appendix 7.1.

The impact velocity was calculated from the images taken from a high-speed camera. In this case a Kodak HS4540 camera was used. The time between each frame was known, so by measuring the distance between a certain number of images gives a velocity. Typical frames and calculation are shown in Figure 3-18.

Image 1      Image 2      Image 3      Image 4

**Scale of images 2.7:1**
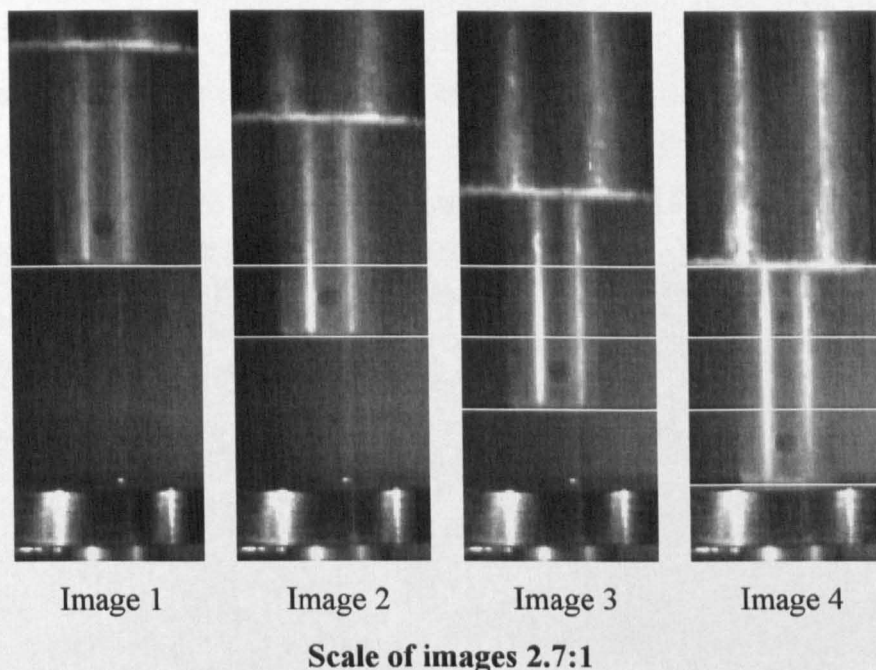
- The camera was recording at 2000 frames per second.
- There are 10 frames between each image.
- Therefore there are 0.005 seconds between each image.
- Distance moved between image 3 and 4 is 27mm (measured from a printed image).
- Speed at impact = 0.027 / 0.005 = **5.4m/s**

**Figure 3-18 - Example of the speed calculation for the dynamic tube tests**

### 3.5.4 Coupon Test Procedures

Three specimens of each hole diameter (0mm, 5mm and 10mm) were tested both quasi-statically and dynamically.

**Quasi-Static Testing**

Quasi-static tests were based on ASTM D3039 [3] and BS2782 [4] using an Instron 1195 test machine with a 100kN load cell. The test speed was 5mm/min and samples were tested to failure.

## Dynamic Testing

The dynamic tests were conducted on a modified falling weight Rosand IFW5 test machine and a novel tensile test fixture designed by Fernie [6]. The original test fixture is shown in Figure 3-19 and schematic in Figure 3-20.
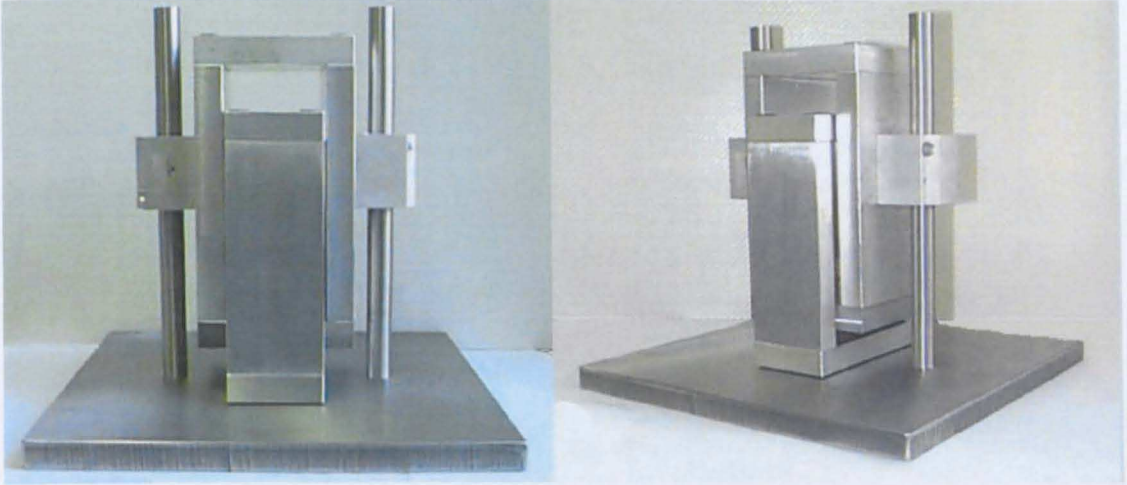


**Figure 3-19 – Original impact tensile test fixture designed by Fernie [6]**
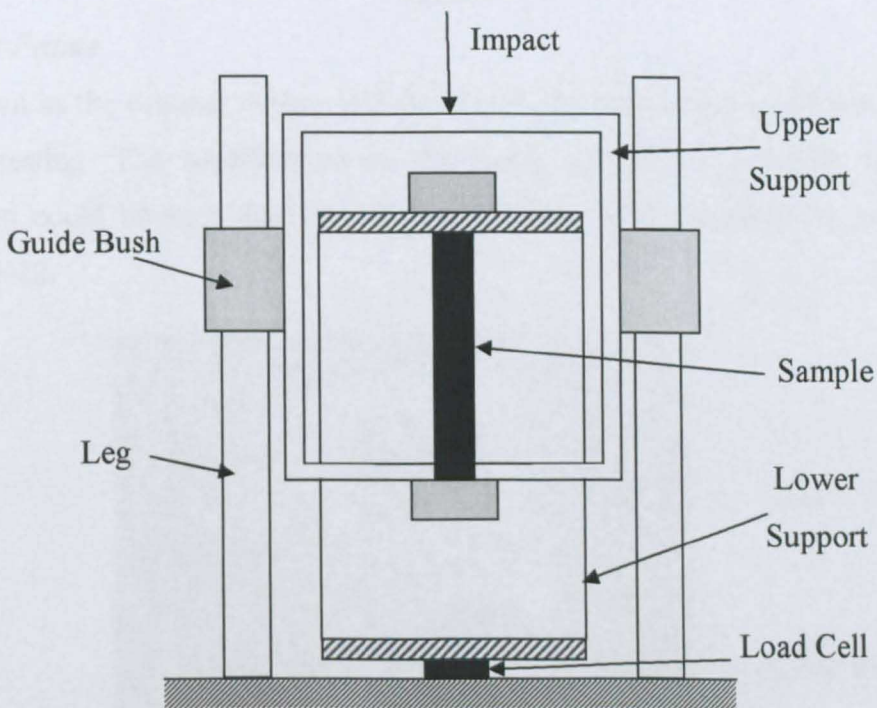


**Figure 3-20 – Schematic of original impact test fixture**

To assess the possibility of bending in the specimens during testing a specimen was fitted with a strain gauge on either side and then tested. The strains from this test are shown in Figure 3-21, and as can be seen, gave almost identical results confirming that no bending was taking place. However, after these initial tests several

modifications and improvements were made to the support frame, position of load cell and grip design and were undertaken in collaboration with Duckett [5] and Fernie [6].
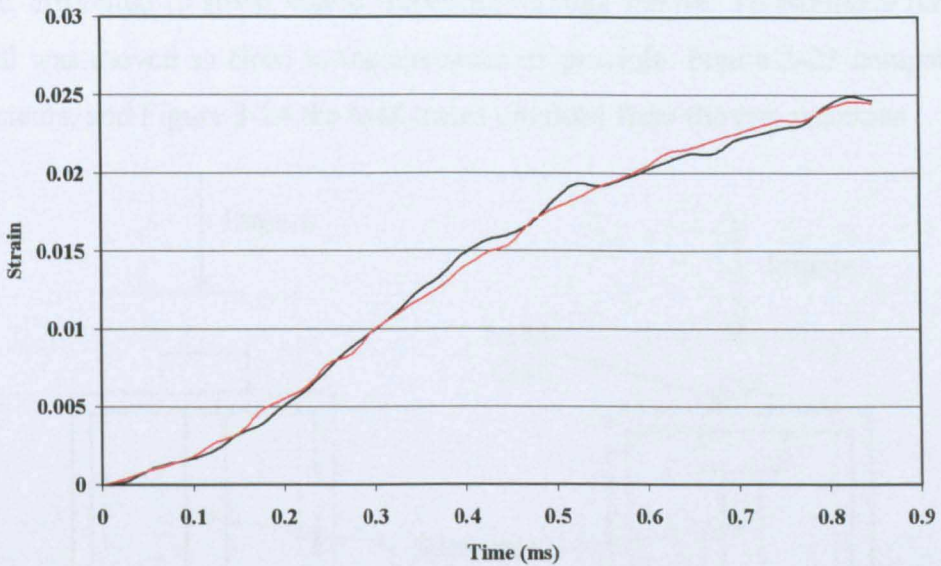


**Figure 3-21 – Traces from the strain gauges fitted to either side of a tensile specimen to check rig alignment**

*Support Frame*

As shown in the original design in Figure 3-19, the specimens could not be viewed during testing. The modification to the frame provided a window, so that the specimen could be seen and filmed during testing. The modified rig is shown in Figure 3-22.
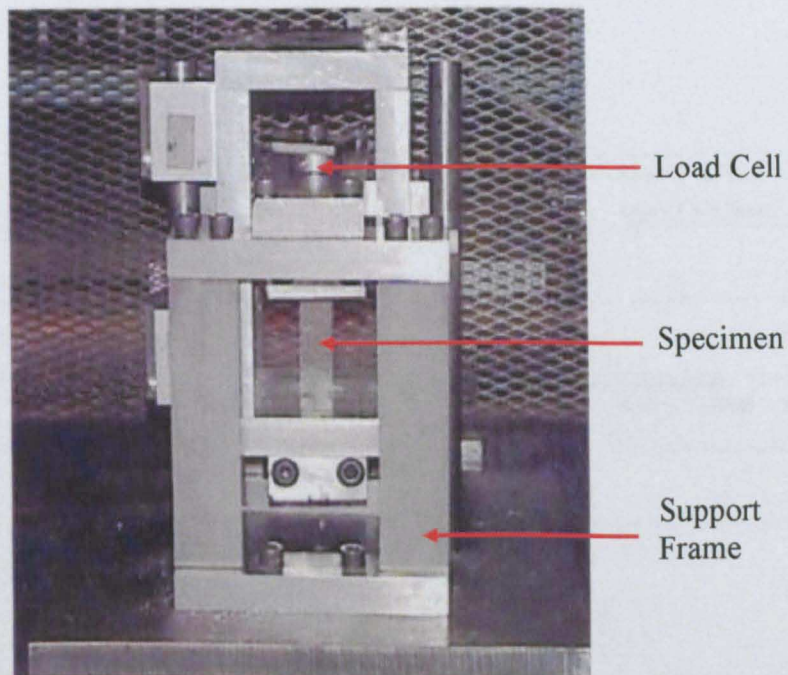


**Figure 3-22 – Modified impact tensile test rig**

*Position of Load Cell*

During the preliminary tests the load data obtained from the load cell contained a lot of noise, attributed to stress waves travelling through the rig. To eliminate these the load cell was moved as close to the specimen as possible. Figure 3-23 compares the amendments, and Figure 3-24 the load traces obtained from the two positions.
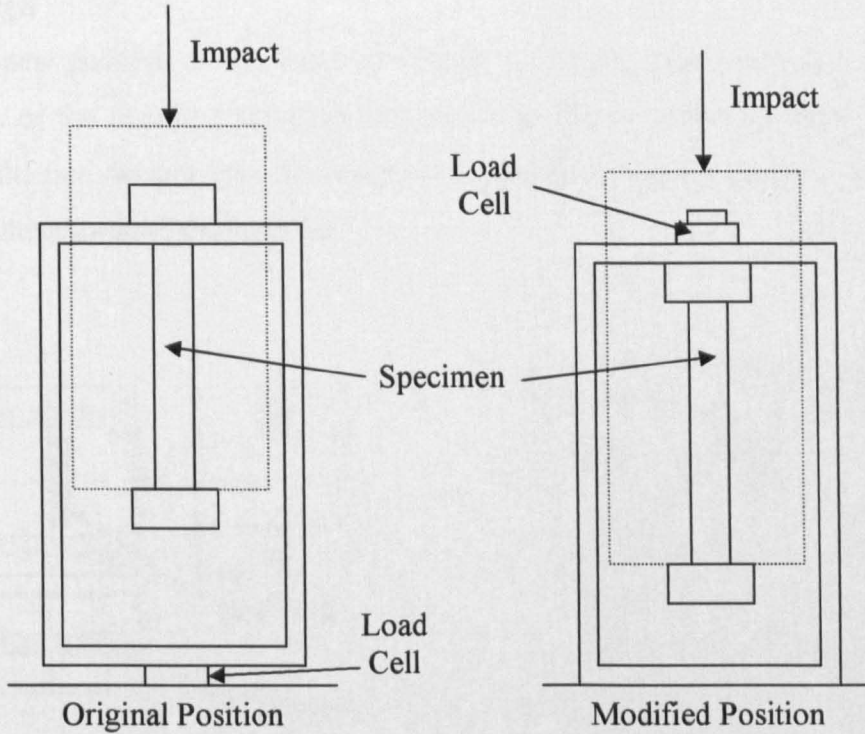


**Figure 3-23 – Original and modified position of the load cell**
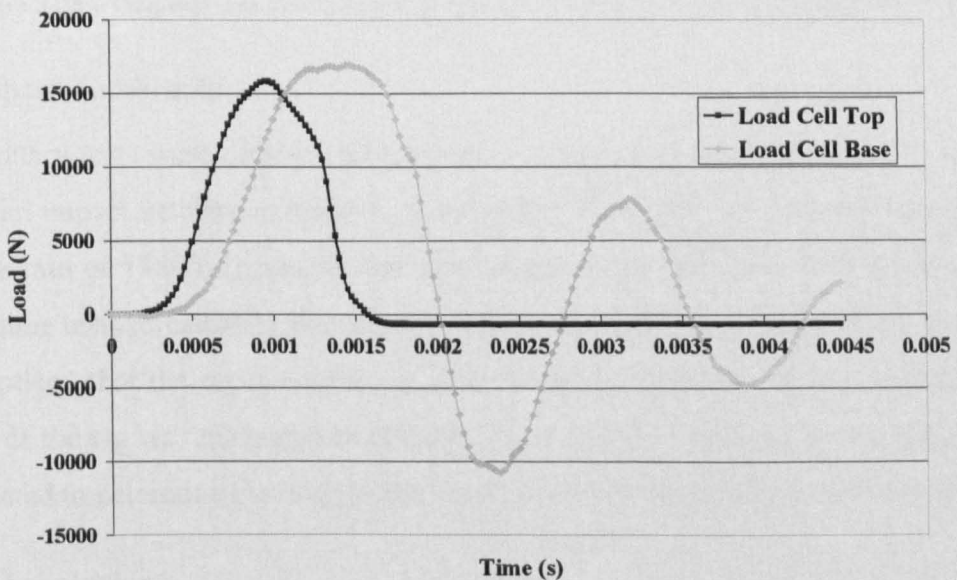


**Figure 3-24 – Load traces from original and modified load cell positions**

The trace achieved from the original position of the load cell, at the base of the rig, shows the load oscillating, attributed to stress reflecting through the rig. Also, a lag can be seen when compared to the modified position, where the load cell was moved to the top of the rig. In this modified position the oscillations and lag have been removed from the trace.

*Grip Design*

With the new position of the load cell (Figure 3-23) new grips were required and a schematic of the new and old grips are shown in Figure 3-25. The only difference between the two designs was the addition of material to the top of the grip allowing for attachment through the load cell.



Fixing bolt     load cell

Original Grip        Modified Grip
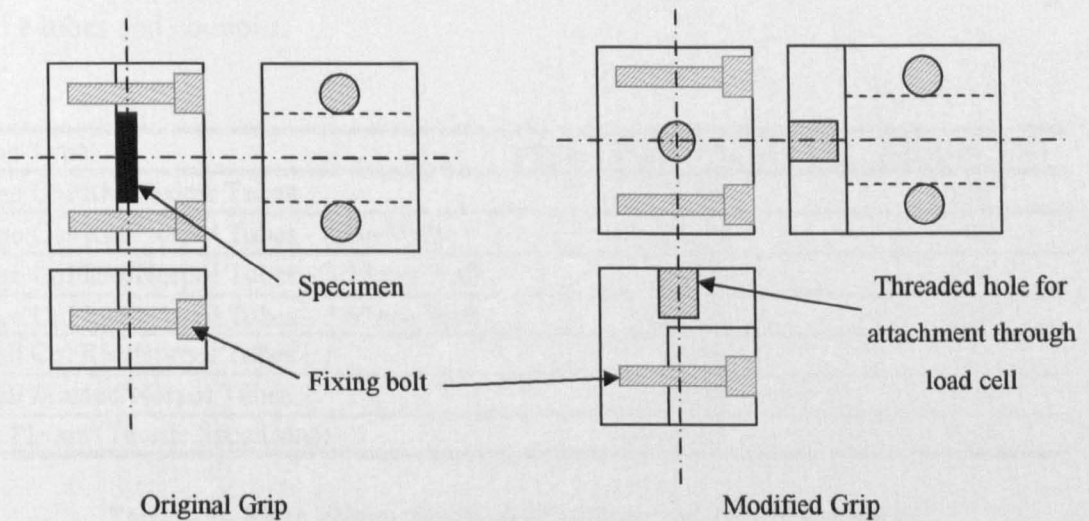
**Figure 3-25 – Original and modified grips used for the dynamic tensile coupon tests at 5m/s**

## Test Speed Calibration

Preliminary tests were conducted in order to find the drop height required to achieve an initial impact velocity of 5m/s. A Kodak HS4540 high-speed camera was used at a sample rate of 13500 frames/sec and the images interpreted in a similar way to the small tube tests to calculate the velocity. Upon inspection of the high-speed images it was noticed that the rig moved away from the impactor upon impact. Therefore the speed of the rig was measured to obtain the test speed. A number of test drops were conducted to determine the drop height required for an initial impact velocity of 5m/s.

## Data Acquisition

The load data were acquired as in 3.5.2.

## 3.6 Physical Characterisation of Specimens

### 3.6.1 Determination of Fibre Volume Fraction

Loss on ignition tests were carried out on both tube and coupon specimens using a similar method to that of the ASTM standard D2584-94 [7]. Samples of around 5g taken from the centres of different mouldings, measured to an accuracy of ±0.01g, were placed in an electric furnace at 625°C. They were left for 3 hours to remove the resin and then the fibres weighed and mass fractions calculated. These values could then be used to calculate the volume fractions using the density values taken from manufacturers' data. The glass fibres had a density of 2540kg/m$^3$, Crystic resin, 1190 kg/m$^3$ and Norpol resin 1100kg/m$^3$. Table 3-2 shows the calculated volume fractions for the tubes and coupons.

| Tube Type | Fibre Volume Fraction (%) | Std. Dev. (%) |
|---|---|---|
| Large CoFRM/Crystic Tubes | 26.24 | 1.10 |
| Large CoFRM/Norpol Tubes - 4mm Wall | 22.78 | 1.32 |
| Large CoFRM/Norpol Tubes - 3.33mm Wall | 22.70 | 2.64 |
| Large CoFRM/Norpol Tubes - 2.67mm Wall | 20.15 | 1.10 |
| Small CoFRM/Norpol Tubes | 25.60 | 1.27 |
| Small Braided/Norpol Tubes | 39.58 | 2.36 |
| Flat Plaque (Tensile Specimens) | 25.57 | 0.93 |

**Table 3-2 – Fibre Volume Fractions of all Tube and Tensile Specimens**

### 3.6.2 Microscopy of Crush Zone

Sections through the tubes were taken after testing had taken place.

*Preparation of Samples*

The samples needed to be cast in resin before sectioning, and to prevent deformation this was done while the tubes were still under load from the Instron test machine. Clear polyester casting resin, initiated by 2% Butanox M50 was used, and left to cure for two hours. Once cured a diamond tipped cutting wheel was used to section the sample before sanding with grit sizes of 250, 400, 600 and 1200. The sample was sanded for three minutes for each grit size, starting with the most coarse, the 250 grit and ending with the 1200 grit. Polishing could then be carried using alumina solution for about 2 minutes before the sample could be examined under an optical microscope.

*Microscopy*

To obtain a complete micrograph of the crush zone around thirty images were required. These images were collected using a Zeiss microscope and Apheion imaging software. Both statically and dynamically tested tubes were examined in this way.

### 3.6.3 SEM Images of Fronds

To examine the samples after testing, a scanning electron microscope (SEM) was used. Samples were taken from the outer fronds of statically and dynamically tested small CoFRM tubes and bonded onto an aluminium tab using a carbon pad. An Emscope SC500 coating unit was used for gold coating the specimens. Here, a vacuum is pulled around the specimen and purged with argon before gold was sputtered onto the sample. Two coats of gold were applied for a total of 4 minutes each. The sample was then placed in the SEM chamber for examination.

### 3.6.4 Examination of the Impact Damage and Crack Formation

Sections were taken to examine the through-thickness effects of the impact damage and to view in detail the cracks that formed during testing. Small CoFRM tubes containing impact damages of 1.5J, 3J, 6J and 9J were sectioned (before crushing) using a diamond tipped cutting wheel. In order to obtain a section through the cracks that formed during an unstable failure mode, interrupted test samples were used. This meant that the tubes were crushed until the crack appeared and then the load was removed allowing sections to be taken through the crack. Sections were taken through small CoFRM tubes containing a 10mm hole and impact damages of 1.5J, 3J, 6J and 9J. These part-tested samples are shown in Figure 3-26.

| 10mm Hole | 1.5J Impact | 3J Impact |



6J Impact | 9J Impact
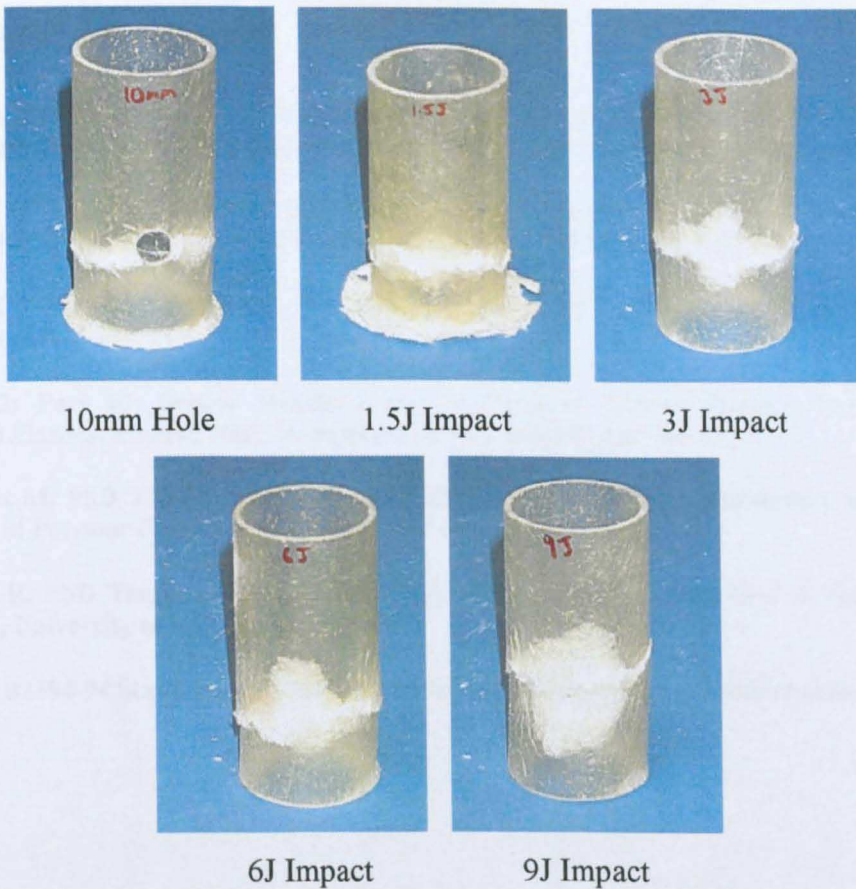
**Figure 3-26 – Part-tested small CoFRM/Norpol tubes used to take sections through fast fractures.**

These samples were sectioned twice, once in the centre of the impact or hole and again 20mm along the circumference from this centre (see Figure 3-27). Once sectioned, samples were viewed using a low magnification microscope and images taken using an attached Polaroid camera.
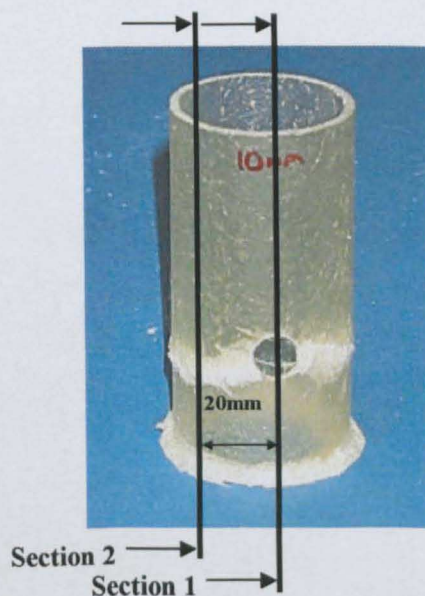


**Figure 3-27 – Sections through part tested tubes**

## 3.7 Chapter 3 References

[1] Corden TJ, Development of Design and Manufacturing Techniques for Glass Reinforced Plastic Waste Water Treatment Equipment, PhD Thesis, University of Nottingham, UK, 1996.

[2] Davim JP and Reis P, Study of delamination in drilling carbon fiber reinforced plastics (CFRP) using design experiments, Composite Structures, Vol.59, No.4, pp481-487, 2003.

[3] ASTM D3039-95a Standard Test Method for Tensile Properties of Oriented Fibre Composites, 1996.

[4] BS2782: Part 10: British Standard Test Methods of Testing Plastics, Part 10, Glass Reinforced Plastics, Method 1003, Determination of Tensile Properties, 1977.

[5] Duckett M, PhD Thesis, Rate Dependant Effects on the Energy Absorption and Material Properties of Polymer Composites, University of Nottingham, 2001.

[6] Fernie R, PhD Thesis, Loading Rate Effects on the Energy Absorption of Tubular Crash Structures, University of Nottingham, 2002.

[7] ASTM D2584-94 Standard Test Method for Ignition Loss of Cured Reinforced Resins.

# 4.0 Results

This chapter looks at the results of the tube crush tests described in Chapter 3. Specific energy absorptions will be measured for each tube type and threshold levels of damage, below which a sample will crush as if undamaged, will be identified for each tube type and damage simulation.

## 4.1 Crushing and Failure Modes of Tubes

Tubes failed by two main mechanisms, *stable* or *unstable* crushing. During stable crushing, tubes failed progressively and a steady crush load was reached and maintained throughout the test. In this case the splaying failure was observed as described in Chapter 2 [1]. Figure 4-1 shows an undamaged tube during crush and respective load-displacement trace and is an example of a stable crush. During the initial part of the crush, up to point 1 in the figure, the crush zone is being formed. At point 1 a debris wedge has been created and opens an axial crack in the wall of the tube. At point 2 a steady crush has been achieved and the geometry of the crush zone will remain unchanged throughout the test.

Unstable crushing was seen in some of the damaged samples where the zone of damage caused a circumferential, through thickness fracture to form. Figure 4-2 shows a small CoFRM tube containing a 7.5mm hole during crush and respective load-displacement trace and is an example of an unstable crush. These fractures cause a reduction in energy absorption due to a reduction in crush load, but many samples recovered to a progressive crush after the damage zones had been passed. Figure 4-3 shows an image taken from a low magnification microscope of a part-tested small CoFRM tube containing a 10mm hole through section 2 (see section 3.6.4). This shows a cross-section of a tube that failed unstably with a crack developing around the tube. The crack can clearly be seen as a shear failure through the wall thickness of the tube. This failure reduces the load carried by the tube as only friction between the two sides of the crack is supporting the structure once it has developed. The failure mode, either stable or unstable, were identified for each test and shown in the results tables throughout this chapter.

The magnitude of the load drop and speed of recovery to progressive crush are dependent on when and how the cracks form and how much of the tube is left uncrushed. In general, smaller amounts of damage caused cracks to form at higher
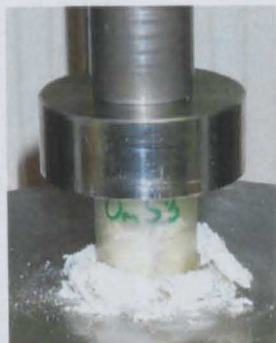
displacements allowing more of the tube to crush progressively and subsequently producing a higher SEA. With larger amounts of damage the unstable failures occurred whilst the load was increasing before a steady crush had been achieved.
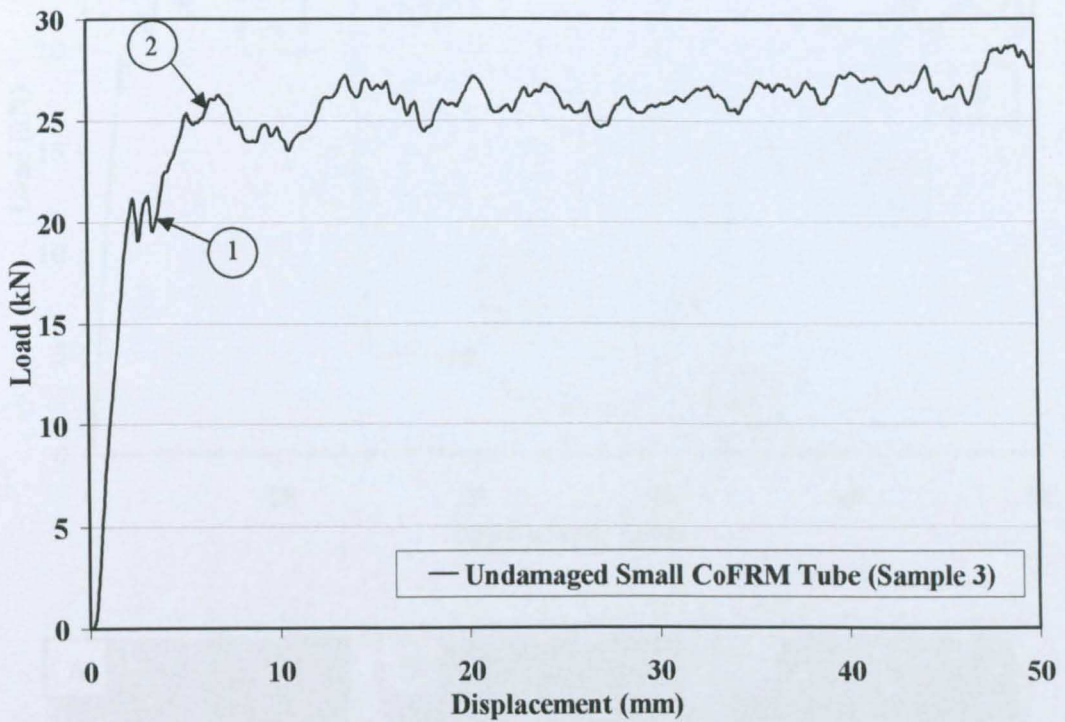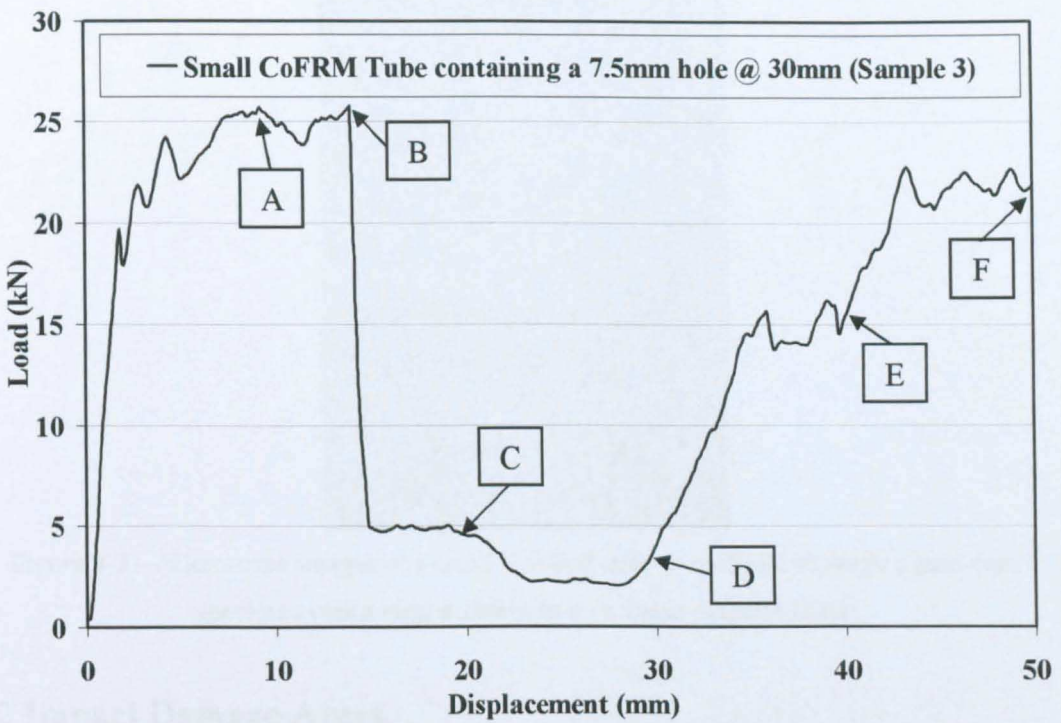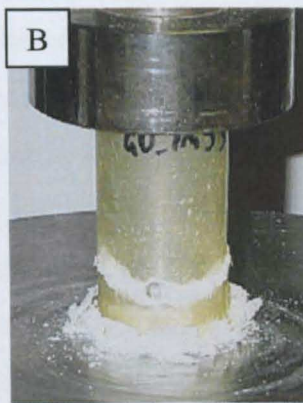




0mm crush

17mm crush

34mm crush

50mm crush

**Figure 4-1 – Load-displacement curve of an undamaged small, 38.1mm diameter, 2mm wall thickness, CoFRM tube (sample 3) and images taken during testing at 5mm/min. An example of the stable failure mode (progressive crush).**

Figure 4-2 – Load-displacement curve of a Small, 38.1mm, 2mm wall thickness, CoFRM tube containing a 7.5mm hole centred at 30mm from the chamfer (sample 3) and images taken during testing at 5mm/min. An example of the unstable crush mode

**Figure 4-3 – Microscope images of a small CoFRM tube at section 2 through a part-tested specimen containing a 10mm hole (6 times magnification)**

## 4.2 Impact Damage Areas

Damage areas in the tubes caused by impacts were measured by calculating the areas of visible damage and stress whitening in the samples (see section 3.4.3). Table 4-1 shows the average damage areas of all tube types and Figure 4-4 shows the impact energy versus damage area curves. As expected, the 4mm walled samples have the smallest damage areas at every impact level and the areas for each impact increase as the tube wall thickness reduces. For the small CoFRM tubes the damage area seems to level off and above a 6J impact there is almost no increase in damage size. A similar trend was seen Habib [2] during impact testing of carbon/epoxy laminates. This levelling off of the damage area suggests that further increases in impact energy would not significantly increase the damage. Instead the through thickness damage would increase up to a point where complete penetration of the impactor would be seen. The other tubes showed a linear relationship between impact energy and damage area and show no signs of the damage area levelling off.

| Tube Type | Damage Area (mm$^2$) | | | |
| --- | --- | --- | --- | --- |
| | 1.5J impact | 3J impact | 6J impact | 9J impact |
| Large CoFRM/Norpol - 4mm Wall | 15 | 165 | 386 | 550 |
| Large CoFRM/Norpol - 3.33mm Wall | 47 | 199 | 436 | 672 |
| Large CoFRM/Norpol - 2.67mm Wall | 73 | 240 | 501 | 749 |
| Small CoFRM/Norpol - 2mm Wall | 219 | 398 | 731 | 786 |
| Small Braided/Norpol - 2mm Wall | 184 | 339 | 578 | 849 |

**Table 4-1 – Average damage areas caused by impact damage for all tube types**
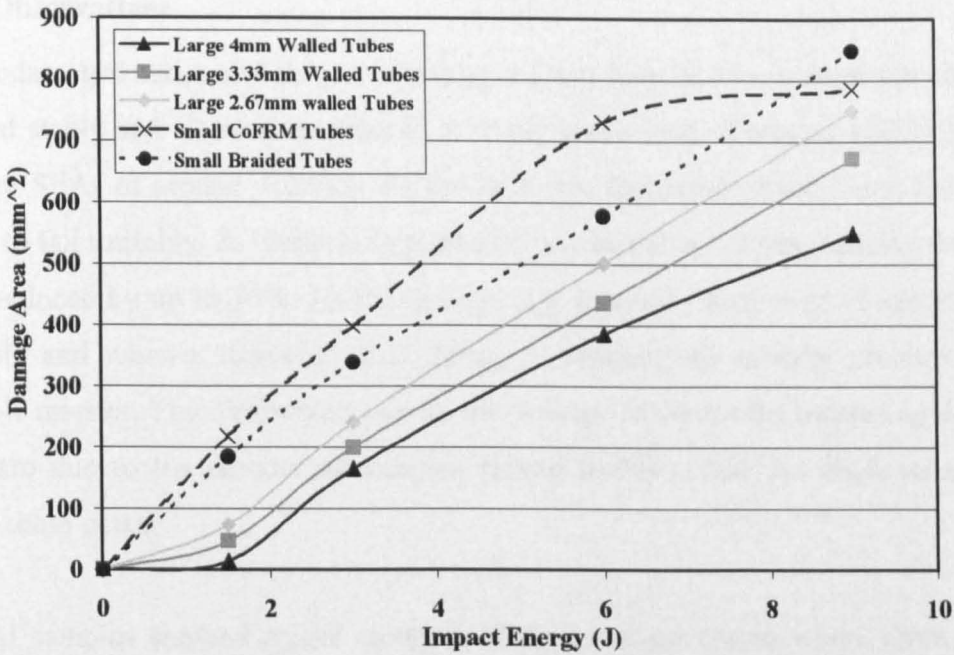
**Figure 4-4 – Impact energy versus damage area for large and small tubes**

## 4.3 Large CoFRM/Crystic Tube Tests

The large Crystic tube tests were quasi-static (5mm/min) tests of 89.1mm diameter, 4mm wall thickness CoFRM tubes, manufactured using a Crystic polyester resin. Samples were tested undamaged and containing 5mm, 10mm, 12.5mm, 16mm and 20.25mm diameter holes, centred at 30mm from the chamfered edge of the tube. Table 4-2 shows the average SEAs, percentage drops in SEA compared to undamaged samples and failure modes (see Section 4.1) for these tests. Load-displacement curves and SEAs for each test are presented in Section 7.2.

| Damage Type | Average SEA (kJ/kg) | Std. Dev. (%) | Percentage Drop (%) | Failure Mode Stable | Unstable |
|---|---|---|---|---|---|
| Undamaged | **66.64** | 5.40 | - | 5 | - |
| 5mm Hole | **70.40** | 3.77 | -5.65 | 5 | - |
| 10mm Hole | **56.45** | 24.18 | 15.29 | 3 | 2 |
| 12.5mm Hole | **44.28** | 26.65 | 33.54 | 2 | 3 |
| 16mm Hole | **37.75** | 45.57 | 43.35 | 2 | 3 |
| 20.25mm Hole | **22.87** | 9.68 | 65.67 | - | 5 |

**Table 4-2 – SEAs, percentage drops and failure modes for the large (89.1mm outer diameter, 4mm wall thickness) Crystic tubes containing holes centred at 30mm from the chamfer, tested at 5mm/min. The failure modes indicate the number of samples that failed stably by progressive crush or unstably by fast fracture, for each damage type**

### 4.3.1 Observations

The undamaged tubes and those containing a 5mm hole at 30mm from the chamfer crushed stably and all samples reached a steady crush load of around 110kN, giving average SEAs of around 70kJ/kg. As the hole size increased above 5mm, the tubes began to fail unstably. A 10mm hole produced two unstable failures, causing the SEA to be reduced by up to 50%. As the damage size increases further more samples fail unstably and when a diameter of 20.25mm is reached, all samples crushed in an unstable manner. The differences seen in the average SEAs for the increasing damage sizes are due to the number of samples failing unstably and the displacements at which these occur.

Several samples showed spikes in the load-displacement traces where there was a sudden and brief drop off in load. Loud cracks where heard during testing and occurred at these spikes. In the general crushing of composite tubes, a central wall crack grows with increasing displacement and it is generally believed that the cracks grow steadily [3]. The behaviour here represents unstable crack growth and was attributed to the resin stiffness.

Figure 4-5 shows a line graph of the average SEAs with standard deviations for the large Crystic tubes. For hole sizes above 5mm an even drop of SEA can be seen. Also, a large deviation in SEAs is seen for hole sizes between 10mm and 16mm in diameter and therefore for these damage sizes, predicting the failure type becomes very difficult. These points will be discussed further in Chapter 5.
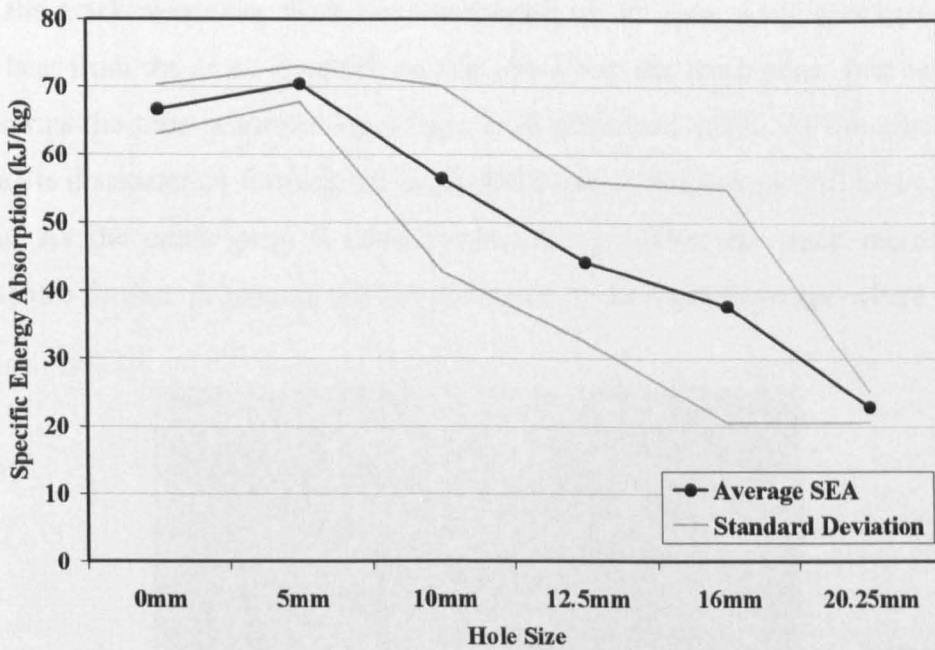
Figure 4-5 - Line graph showing average SEAs and standard deviations of the CoFRM/Crystic
89.1mm diameter tubes containing holes centred at 30mm from the chamfer

## Thresholds

There was no change in crush behaviour when a 5mm hole was introduced into the
large CoFRM/Crystic tubes and the results (Figure 4-5) show a small increase in
average SEA. This effect was attributed simply to variability within the specimens.
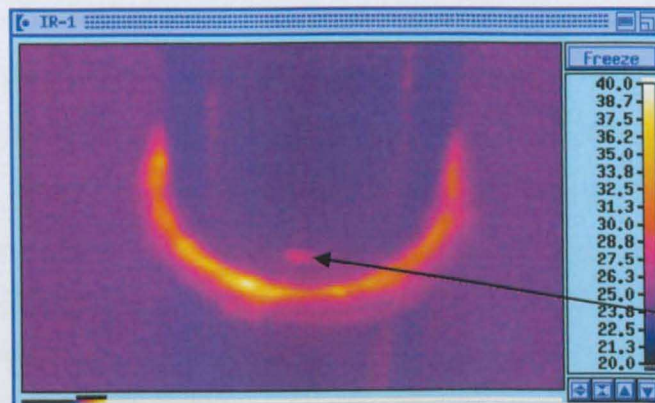
### 4.3.2 Thermal Images of Large CoFRM/Crystic Tubes

Figure 4-6 shows thermal images taken of the CoFRM/Crystic 89.1mm diameter
tubes. Image (a) shows an undamaged tube mid-crush and the temperature can be seen
to rise to 44°C in the crush zone. This is an increase of 20°C when compared to the
main body of the tube. The heat is caused by friction between the crush zone and the
crush platen and between the debris wedge and the tube itself. Chadwick and Caliskan
[5] reported an increase in the crush zone temperature of 30°C in a glass/vinylester
tube and attributed the rise to friction between broken fibres and resin.

Images (b) and (c) are taken from the same test of a tube containing a 10mm hole.
Image (b) shows the appearance of the hole before a crack had been formed and
before any damage had been observed by eye. This shows that the hole is acting as a
stress concentration as the load and hence energy is being concentrated at this point.
Image (c) shows the crack spiralling round the tube and it is interesting to note that

where the crack meets the crush zone to the left of the hole, a hot spot can be seen where heat from the crack is adding to that already in the crush zone. Just before the crack forms the tube is supporting a large load of around 90kN. As the crack forms this load is dissipated in forming the crack and some of this energy will be transferred to heat. As the crush zone is already hot the heat from the crack increases the temperature further, producing the hot spot seen in the thermal image where the two meet.
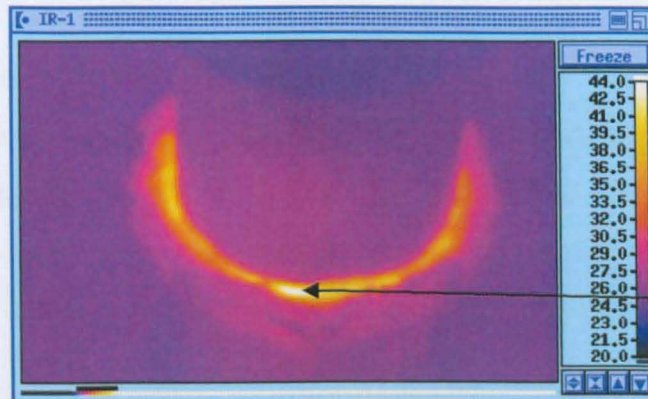


(a) Undamaged tube - Temperature can be seen reaching up to 44°



(b) Tube containing a 10mm hole - Hole can be seen before crack has appeared.
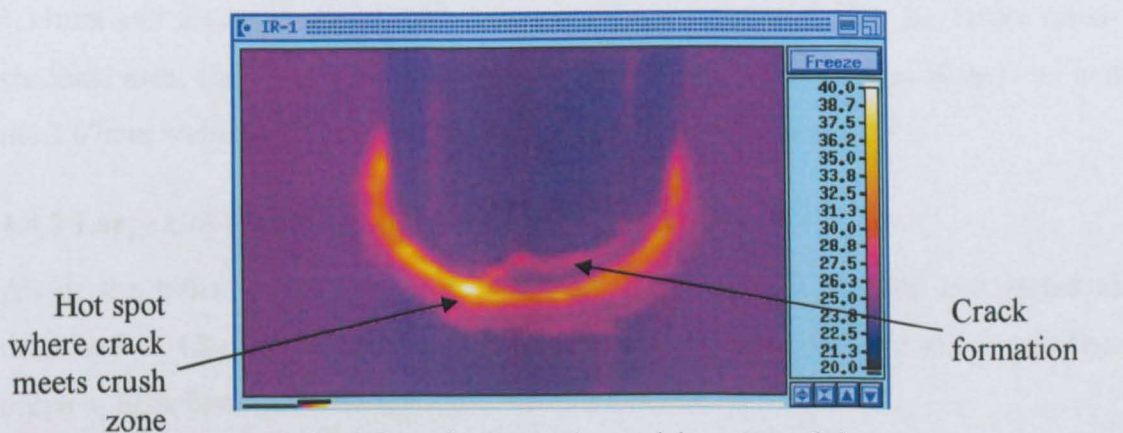


(c) Crack formation in sample containing a 10mm hole

**Figure 4-6 – Thermal images taken from large CoFRM/Crystic tubes during crush at 5mm/min**

## 4.4 Large CoFRM/Norpol Tubes

In this section, results are presented for the tubular crush tests of the large (89.1mm diameter) CoFRM/Norpol tubes with varying wall thickness between 2.67mm and 4.00mm. Load-displacement curves and SEA values for each test are shown in Section 7.3. All the tests were quasi-static (5mm/min) and simulated damage caused by drilled holes and impacts was added. Curves were plotted from data recorded directly from the Instron test machine and SEAs calculated as described in Chapter 3.

### 4.4.1 Undamaged Large CoFRM/Norpol Tubes

Table 4-3 shows the average SEAs and failure modes recorded for the quasi-statically (5mm/min) tested large CoFRM tubes of varying wall thickness.

The undamaged large tubes of all wall thickness failed stably with a steady crush load. The scatter in SEA was very low for all the undamaged tubes with a maximum deviation of only 4.13% for the 2.67mm walled tubes.

From these tube geometries, there has been no threshold value of t/D ratio found, as there has been no drop off in energy absorption at higher levels. It had been shown by Hamada and Ramakrishna [4] that carbon/PEEK tubes with a t/D ratio of less than 0.015 would fail by brittle fracture whereas above 0.015 they failed progressively. They found that as long as the tube crushed progressively (t/D > 0.015) SEA was dependant on t rather than the t/D ratio and that the highest energy absorptions were for values of t between 2-3mm.

The differences between the undamaged tubes were their mean crush loads and subsequent SEAs. The mean crush loads were 110kN, 90kN and 70kN for the 4mm, 3.33mm and 2.67mm walled tubes respectively. As expected, due the larger cross-sectional area, the 4mm walled samples produced the highest energy absorption and the 2.67mm walled tubes the least with a drop in SEA of around 11%.

### 4.4.2 Large CoFRM/Norpol Tubes containing Holes

All of the holes were centred at 30mm from the chamfered edge, and tested as described in Chapter 3. Table 4-3 shows the SEAs, failure modes and percentage drops in SEA from an undamaged tube for these tests.

| Hole Size | Wall Thickness (mm) | Average SEA (kJ/kg) | Std. Dev. (%) | Percentage Drop (%) | Failure Mode | |
|---|---|---|---|---|---|---|
| | | | | | Stable | Unstable |
| Undamaged | 4 | 70.68 | 3.16 | - | 3 | - |
| | 3.33 | 66.97 | 2.21 | - | 3 | - |
| | 2.67 | 63.04 | 4.13 | - | 3 | - |
| 5mm Hole | 4 | 72.18 | 2.41 | -2.12 | 3 | - |
| | 3.33 | 70.05 | 2.46 | -4.59 | 3 | - |
| | 2.67 | 63.57 | 6.77 | -0.85 | 3 | - |
| 7.5mm Hole | 4 | 38.90 | 16.84 | 44.96 | - | 3 |
| | 3.33 | 61.70 | 9.56 | 7.87 | 2 | 1 |
| | 2.67 | 43.11 | 34.04 | 31.61 | 1 | 2 |
| 10mm Hole | 4 | 34.06 | 7.00 | 51.82 | - | 3 |
| | 3.33 | 46.66 | 35.44 | 30.33 | 1 | 2 |
| | 2.67 | 34.68 | 19.89 | 44.99 | - | 3 |
| 12.5mm Hole | 4 | 30.41 | 13.28 | 56.98 | - | 3 |
| | 3.33 | 33.34 | 17.01 | 50.21 | - | 3 |
| | 2.67 | 27.09 | 16.86 | 57.03 | - | 3 |
| 16mm Hole | 4 | 32.39 | 21.07 | 54.17 | - | 3 |
| | 3.33 | 30.42 | 41.21 | 54.58 | - | 3 |
| | 2.67 | 20.51 | 12.01 | 67.46 | - | 3 |

Table 4-3 – SEAs, percentage drops in SEA and failure modes for the 89.1mm diameter CoFRM/Norpol tubes of varying wall thickness containing drilled holes centred at 30mm from the chamfer.

When introducing holes to the 4mm walled tubes it was seen that the 5mm hole had no significant effect on the failure mode or energy absorption. However, larger holes provoked unstable failures and drops in SEA of between 45% and 57% were seen. Average SEA values for these tubes were all below 40kJ/kg, compared to the undamaged tubes, which produced an average of 70.68kJ/kg.

Similarly, 5mm holes in the 3.33mm walled tubes had no significant effect on failure mode or SEA. The 7.5mm hole produced one unstable failure and a drop in average SEA of 7.87%. Two unstable failures were seen when a 10mm hole was added and a decrease in SEA of 30.33%. The 12.5mm and 16mm holes caused unstable failures in all samples and drops in SEA of over 50%.

As with the previous tubes, the 5mm hole in a 2.67mm walled tube had no significant effect but as the hole size increased to 7.5mm two samples failed unstably causing a drop in SEA of 31.61%. Above this size all samples failed unstably with drops in SEA of up to 67.46% for the 16mm hole.

Similar trends were seen in the large CoFRM tubes containing holes as had been seen in the large Crystic tubes. A line graph of the average SEAs for each wall thickness against hole size is shown in Figure 4-7.
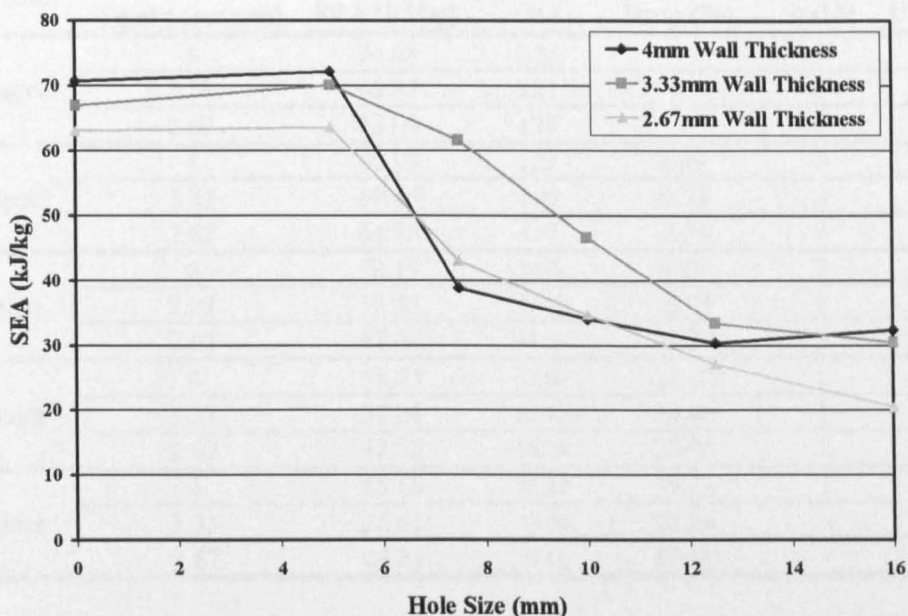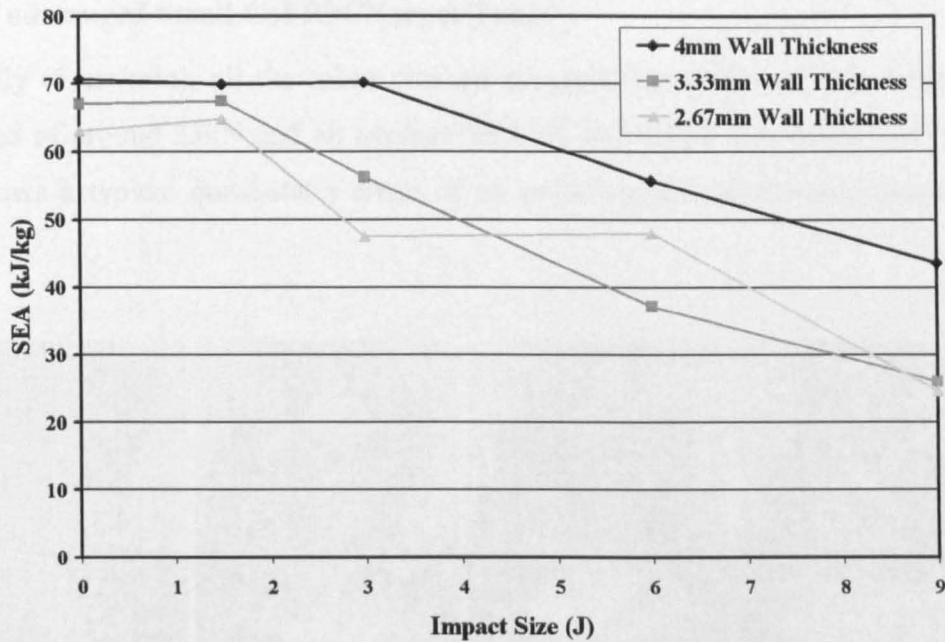
Figure 4-7 – Average SEAs for each hole size tested in the CoFRM/Norpol large (89.1mm diameter) tubes of varying wall thickness

In general, as hole diameter increased above 5mm, more samples failed unstably, producing lower average SEAs. At a hole size of 12.5mm, where all samples failed unstably, this reduction in SEA levels off and it is believed that further increases in hole diameter would not reduce the energy absorption further. Therefore, a threshold hole size of 5mm was found for all wall thicknesses above which tubes began to fail unstably.

### 4.4.3 Large CoFRM/Norpol Tubes containing impact damage

This section looks at the large, 89.1mm diameter CoFRM/Norpol tubes of varying wall thickness containing impact damage. The tests were conducted and impacts applied as described in Chapter 3. Table 4-4 summarises the results.

| Impact Size | Wall Thickness (mm) | Average SEA (kJ/kg) | Std. Dev. (%) | Percentage Drop (%) | Failure Mode | |
|---|---|---|---|---|---|---|
| | | | | | Stable | Unstable |
| Undamaged | 4 | 70.68 | 3.16 | - | 3 | - |
| | 3.33 | 66.97 | 2.21 | - | 3 | - |
| | 2.67 | 63.04 | 4.13 | - | 3 | - |
| 1.5J Impact | 4 | 69.91 | 2.73 | 1.09 | 3 | - |
| | 3.33 | 67.45 | 1.96 | -0.71 | 3 | - |
| | 2.67 | 64.78 | 4.17 | -2.76 | 3 | - |
| 3J Impact | 4 | 70.19 | 3.67 | 0.69 | 3 | - |
| | 3.33 | 56.23 | 33.12 | 16.05 | 2 | 1 |
| | 2.67 | 47.47 | 48.58 | 24.70 | 2 | 1 |
| 6J Impact | 4 | 55.75 | 33.60 | 21.12 | 2 | 1 |
| | 3.33 | 37.24 | 62.72 | 44.40 | 1 | 2 |
| | 2.67 | 47.92 | 55.78 | 23.98 | 2 | 1 |
| 9J Impact | 4 | 43.60 | 58.40 | 38.31 | 1 | 2 |
| | 3.33 | 26.01 | 13.70 | 61.16 | - | 3 |
| | 2.67 | 24.59 | 28.60 | 61.00 | - | 3 |

Table 4-4 - SEAs, percentage drops in SEA and failure modes for the 89.1mm diameter CoFRM/Norpol tubes of varying wall thickness containing impacts centred at 30mm from the chamfer.

When impact damage was introduced to the 4mm walled tubes no change was seen in either the failure mode or SEA recorded for impacts up to and including 3J. All samples failed progressively with no apparent effect of the pre-test damage. For larger impacts, samples began to fail unstably with the 6J impact causing one unstable failure and the 9J impact two. Average SEA fell by 21.12% and 38.31% respectively for the 6J and 9J impacts.

For the 3.33mm walled tubes the pre-test damage effects became evident at 3J (causing one unstable failure). The 6J impact produced two and the 9J impact causing all samples to fail unstably.

Again the 1.5J impact had no significant effect on the failure mode or energy absorption of the 2.67mm walled tubes. Both the 3J and 6J impacts caused drops in SEA of around 24% with one out of the three samples failing unstably. The 9J impact caused all samples to fail unstably with a drop in average SEA of 61% compared to the undamaged tubes.

As with the holes, more severe pre-damage caused more unstable failures and lower SEAs. It was also noticed that when a sample containing damage crushed progressively, there was a drop in load around the damaged region and this drop increased with increasing pre-damage energy. The average SEAs for each wall thickness against impact damage size are shown in the line graph in Figure 4-8.

**Figure 4-8 - Average SEAs for each impact size tested in the CoFRM/Norpol large (89.1mm diameter) tubes of varying wall thickness**

## Thresholds

The pre-test damage thresholds for the large tubes appeared to be 3J impact for the 4mm walled samples and 1.5J for the 3.33mm and 2.67mm walled samples. Unsurprisingly, the thicker wall thickness of tube withstood more impact damage before failure modes become affected. This reduced the theoretical damage density. Above these threshold values the SEA was subject to greater variability as the probability of unstable failures increased.

## 4.5 Small CoFRM/Norpol Tube Tests

In this section, results are presented for the tubular crush tests of the 38.1mm diameter tubes manufactured from CoFRM and Norpol resin. Curves were plotted from data recorded directly from the Instron test machine for the static results and from the load cell for the dynamic tests. SEAs were calculated as described in Chapter 3. The SEAs and load-displacement curves for all small CoFRM/Norpol tube tests are shown in Section 7.4.

### 4.5.1 Undamaged Small CoFRM/Norpol Tubes

Statically (5mm/min), all the tubes crushed progressively with a steady crush load achieved of around 25kN and an average SEA of 74.55kJ/kg was calculated. Figure 4-9 shows a typical quasi-static crush of an undamaged tube showing progressive failure.



| 0mm crush | 17mm crush | 34mm crush | 50mm crush |

**Figure 4-9 – Quasi-static crush of an undamaged, 38.1mm diameter CoFRM/Norpol tube (sample 3)**

Dynamically (5m/sec), the tubes crushed progressively as shown in the high speed camera images of Figure 4-10, but the steady crush load achieved was slightly lower than for the quasi-static tests, at around 22kN, leading to an average SEA of 67.85kJ/kg, a drop of 9% compared to the statically tested samples.
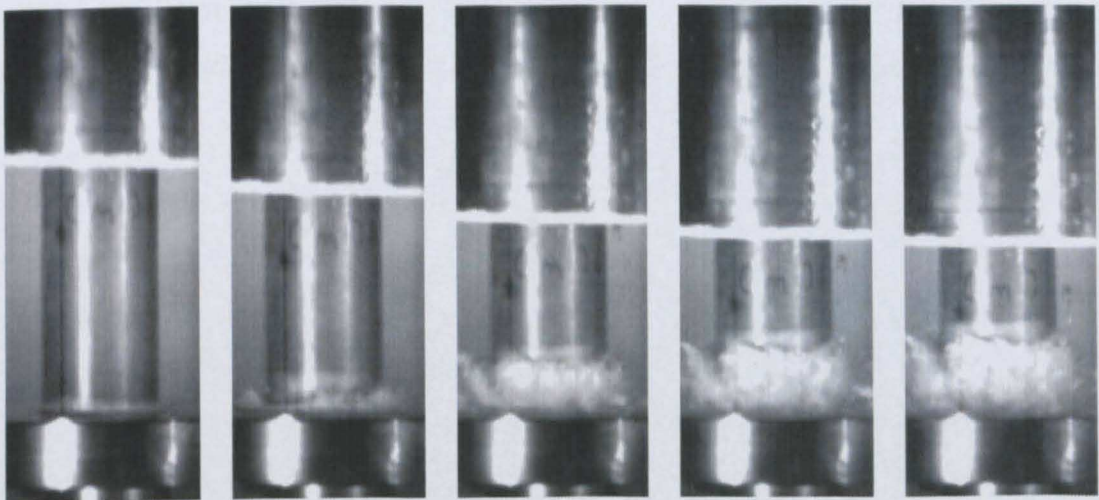


**Figure 4-10 – High-speed camera images from a dynamically crushed small (38.1mm diameter) CoFRM/Norpol tube**

Figure 4-11 shows the undamaged tubes post crush. Looking at the statically tested tubes it can be seen that the fronds are curved and remain relatively intact. However, during the dynamic tests the resin fragments to greater extent, fibres become unconstrained and the fronds remain close to the tube wall with a smaller radius of curvature than the quasi-static tests.
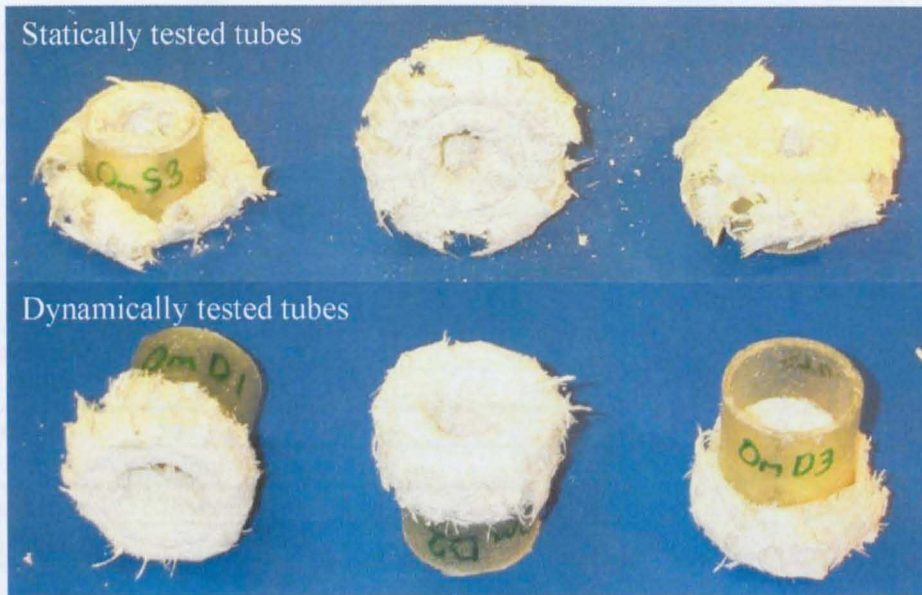


**Figure 4-11 – Photos of undamaged small (38.1mm diameter) CoFRM/Norpol tubes post crush**

## 4.5.2 Small CoFRM/Norpol Tubes Containing Holes

The main results are summarised in Table 4-5. The following sections discuss the effects of adding a hole of between 5mm and 16mm diameter and two 5mm holes centred at 30mm from the chamfered edge. Also, the effect of hole position was investigated by adding a 10mm centred at 15mm, 30mm and 45mm from the chamfer.

| Hole Size and Position | Test Speed | Average SEA (kJ/kg) | Std. Dev. (%) | Percentage Drop (%) | Failure Mode | |
|---|---|---|---|---|---|---|
| | | | | | Stable | Unstable |
| Undamaged | 5mm/min | 74.55 | 3.75 | - | 3 | - |
| | 5m/s | 67.85 | 4.01 | - | 3 | - |
| 5mm Hole @15mm | 5mm/min | 66.72 | 12.68 | 10.5 | 2 | 1 |
| | 5m/s | 66.77 | 6.50 | 1.6 | 3 | - |
| 5mm Hole @30mm | 5mm/min | 58.36 | 39.80 | 21.7 | 2 | 1 |
| | 5m | 60.02 | 2.69 | 11.5 | 3 | - |
| 2x5mm Hole @30mm | 5mm/min | 38.21 | 46.46 | 48.7 | - | 3 |
| | 5m/s | 58.34 | 2.30 | 14.0 | 3 | - |
| 7.5mm Hole @30mm | 5mm/min | 40.67 | 12.42 | 45.5 | - | 3 |
| | 5m/s | 51.78 | 11.88 | 23.7 | 2 | 1 |
| 10mm Hole @15mm | 5mm/min | 48.70 | 16.81 | 34.7 | - | 3 |
| | 5m/s | 46.46 | 18.66 | 31.5 | 1 | 2 |
| 10mm Hole @30mm | 5mm/min | 21.97 | 24.65 | 70.5 | - | 3 |
| | 5m/s | 54.33 | 10.44 | 19.9 | 1 | 2 |
| 10mm Hole @45mm | 5mm/min | 26.26 | 13.77 | 64.8 | - | 3 |
| | 5m/s | 59.65 | 1.90 | 12.1 | 3 | - |
| 12.5mm Hole @30mm | 5mm/min | 25.68 | 17.18 | 65.6 | - | 3 |
| | 5m/s | 20.07 | 16.82 | 70.4 | - | 3 |
| 16mm Hole @30mm | 5mm/min | 22.32 | 52.59 | 70.1 | - | 3 |
| | 5m/s | 19.10 | 28.41 | 71.8 | - | 3 |

**Table 4-5 – Average SEAs, percentage drop in SEA and failure modes for the small 38.1mm diameter CoFRM/Norpol tubes containing holes tested at 5mm/min and 5m/s.**

## Addition of a Hole at 15mm

### Static Performance

Adding a 5mm hole into the tube at 15mm caused an unstable failure in one of the three statically tested tubes. Here, the load dropped significantly for 10mm of crush before recovering up to a steady crush load. The other samples crushed progressively with similar SEAs to the undamaged tubes. The introduction of a 10mm hole however caused all specimens to fail unstably. The load-displacement curves all dropped to 5kN after a 2-3mm displacement and did not reach a steady crush load until 25mm displacement.

### Dynamic Performance

Dynamically, the effect of the 5mm hole was less noticeable, with local drops in load only at the position of the holes. Tubes crushed progressively and a drop in average SEA of just 1.6% was seen when compared to the undamaged tubes. However, adding a 10mm hole at 15mm caused a 31.5% drop in SEA with tubes cracking and failing

Chapter 4 - Results

unstably as had been seen in the static tests. Fragments were also retrieved from the drop tower and similar pieces were left on the crush platen during the static tests.

**Addition of a Hole at 30mm**

The small CoFRM tubes were tested with hole sizes of 5mm, 7.5mm, 10mm, 12.5mm and 16mm centred at 30mm from the chamfer. The bar chart in Figure 4-12 shows the average SEAs for each of the dynamically and statically tested tubes containing these holes.
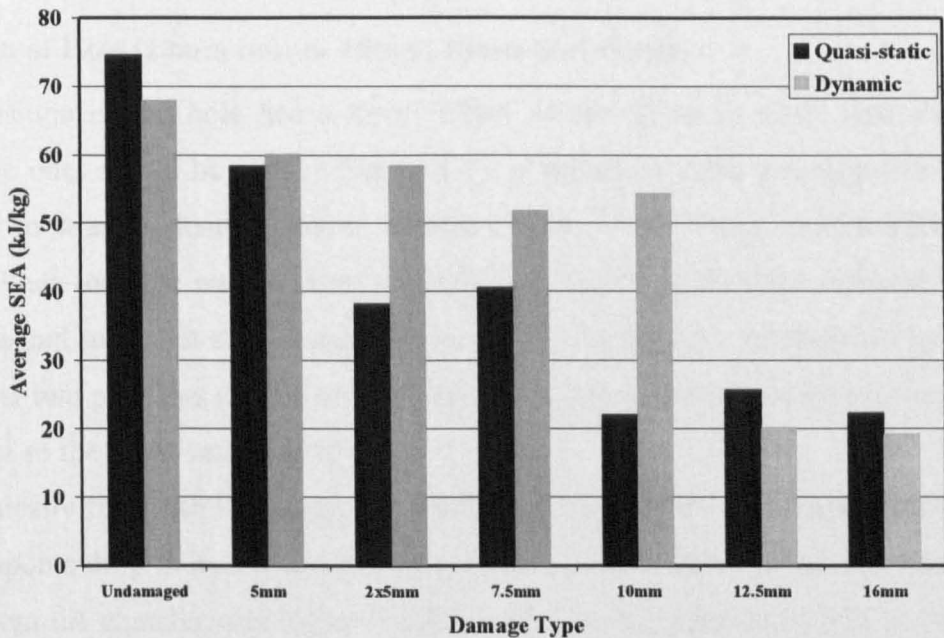


**Figure 4-12 – Bar chart showing average SEAs for the quasi-static and dynamic tests (5m/sec) of the small (38.1mm diameter, 2mm wall) CoFRM/Norpol tubes containing holes centred at 30mm.**

Quasi-statically, all of the tubes saw drops in SEA and every tube failed unstably except for one of the samples with a 5mm hole. The SEA reductions ranged between 21.7% (when a 5mm hole was introduced) up to 70.5% for the tubes containing a 10mm hole.

Dynamically the effect of the holes becomes less damaging to the energy absorption. At a diameter of 7.5mm there were drops in SEA of up to 23.7. For the samples containing a 12.5mm or 16mm hole the SEAs dropped by over 70%.

4-17

**Multiple Holes**

Quasi-statically, all of the tubes containing two 5mm holes at 30mm failed in an unstable manner although there was a large variation in the displacements at which the fracture initiated. This led to a very high standard deviation of 46.46% and an average SEA of 38.21kJ/kg, a 48.70% drop from the undamaged tubes.

The dynamically tested samples failed progressively with local drops in load around the holes at 30mm displacement. The average SEA recorded was 58.34kJ/kg, which fell between that for the 5mm and 10mm holes at 30mm and is similar to the 7.5mm hole. This makes sense, as the losses in available volumes are similar in these cases.

**Position of Hole (10mm hole at 15mm, 30mm and 45mm)**

The position of the hole had a larger effect on the SEAs in static tests than the dynamic ones as can be seen in Figure 4-13. Statically, a crack propagated from the hole as soon as the load increased whether it was 15mm, 30mm or 45mm from the edge. When the hole was at 15mm the SEA was higher as the crack affected less of the tube and sufficient stroke remained for the tube to regain a steady crush load. For the other two positions (30mm and 45mm) the load never recovered before the end of the tests so the SEAs remained low.

Dynamically the crush load was only affected when the crush zone reached the hole, whereupon a drop in load was seen. This led to higher SEAs when the distance of the hole from the chamfer was higher. Undamaged dynamic specimens only crushed for about 30mm due to the limited impact energy and in the case of the 10mm hole at 45mm, the crush zone did not reach the hole and so no drop in load was seen. On peeling away the fronds after testing it was found that the geometry of the hole remained unchanged.
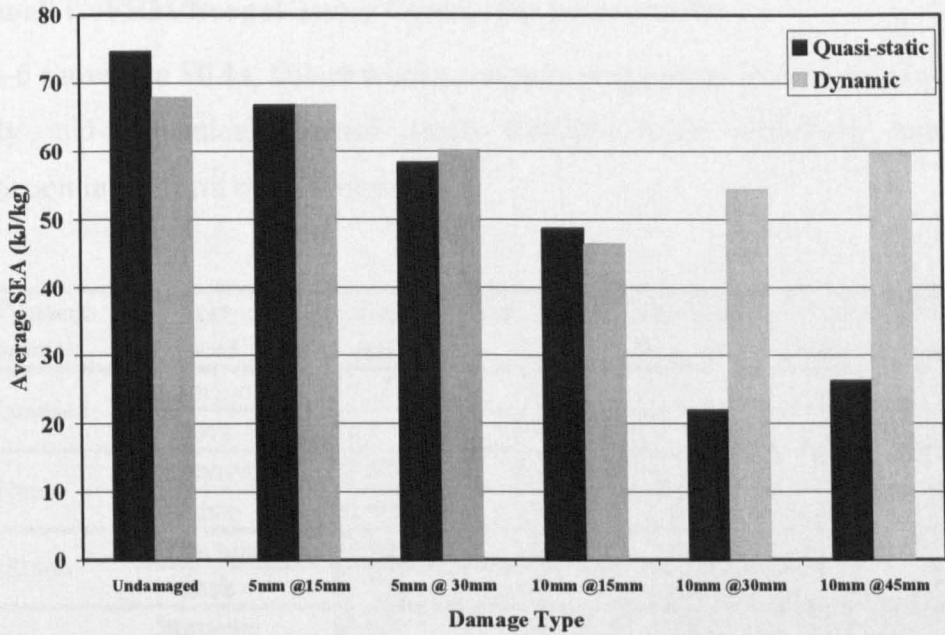
**Figure 4-13 – Bar chart showing SEAs for the small, 38.1mm diameter CoFRM/Norpol tubes containing holes along the tube, tested quasi-statically and dynamically (5m/sec)**

## Thresholds

When considering threshold values of holes that would have no effect on the energy absorption of the small CoFRM tubes it was found that quasi-statically, no hole could be added from 5mm upwards without the probability of provoking an unstable failure and hence a drop in SEA. Dynamically, one or two 5mm holes could be added with little effect on the energy absorption. Larger holes were likely to provoke unstable failures and lower SEAs.

### 4.5.3 Small CoFRM/Norpol Tubes Containing Delamination

Table 4-6 shows the SEAs, failure modes and percentage drops in SEA for the quasi-statically and dynamically tested small CoFRM tubes containing simulated delamination in the form of PET inserts.

| PET Insert Diameter | Test Speed | Average SEA (kJ/kg) | Std. Dev. (%) | Percentage Drop (%) | Failure Mode Stable | Unstable |
|---|---|---|---|---|---|---|
| Undamaged | 5mm/min | 74.55 | 3.75 | - | 3 | - |
| | 5m/s | 67.85 | 4.01 | - | 3 | - |
| 32mm | 5mm/min | 70.67 | 0.35 | 5.2 | 3 | - |
| | 5m/s | 64.44 | 2.34 | 5.0 | 3 | - |
| 2x32mm | 5mm/min | 59.99 | 4.54 | 19.5 | 3 | - |
| | 5m/s | 59.04 | 4.80 | 13.0 | 3 | - |
| 50.8mm | 5mm/min | 63.63 | 10.87 | 14.6 | 3 | - |
| | 5m/s | 61.16 | 2.57 | 9.9 | 3 | - |

**Table 4-6 - Average SEAs, percentage drop in SEA and failure modes for the 38.1mm diameter CoFRM tubes containing simulated delamination tested at 5mm/min and 5m/s**

Overall, only small drops in SEA are seen compared to the undamaged tubes for both the static and dynamic tests. The single 32mm PET insert caused 5% reduction in SEA for both the static and dynamic tests. Larger reductions (19.5% and 13%) for the static and dynamic tests respectively, were recorded when two inserts are introduced. The 50.8mm PET insert reduced SEA by 14.6% for the static and 9.9% for the dynamic tests.

The reductions in SEA, although less damaging than the through-thickness holes, can be attributed to a reduction in interlaminar fracture toughness and a consequent reduction in the energy required to form the central interlaminar crack.

### Thresholds

No threshold level of delamination for unstable failure has been found from these studies as although there have been up to 20% reduction in SEA, all samples crushed progressively and there were no unstable failures produced.

### 4.5.4 Small CoFRM/Norpol Tubes Containing Impact Damage

Table 4-7 shows the average SEAs, failure modes and percentage drops in SEA for the small CoFRM tubes with pre-test impact damage.

| Impact Size | Test Speed | Average SEA (kJ/kg) | Std. Dev. (%) | Percentage Drop (%) | Failure Mode Stable | Failure Mode Unstable |
|---|---|---|---|---|---|---|
| Undamaged | 5mm/min | 74.55 | 3.75 | - | 3 | - |
| | 5m/s | 67.85 | 4.01 | - | 3 | - |
| 1.5J Impact | 5mm/min | 46.50 | 48.65 | 37.6 | 1 | 2 |
| | 5m/s | 64.28 | 5.40 | 5.3 | 3 | - |
| 3J Impact | 5mm/min | 29.51 | 29.82 | 60.4 | - | 3 |
| | 5m/s | 40.60 | 35.68 | 40.2 | - | 3 |
| 6J Impact | 5mm/min | 29.31 | 10.97 | 60.7 | - | 3 |
| | 5m/s | 31.43 | 9.64 | 53.7 | - | 3 |
| 9J Impact | 5mm/min | 21.90 | 32.02 | 70.6 | - | 3 |
| | 5m/s | 36.36 | 9.66 | 46.4 | - | 3 |

Table 4-7 - Average SEAs, percentage drop in SEA and failure modes for the 38.1mm diameter CoFRM tubes containing impacts tested at 5mm/min and 5m/s

The average SEAs for the undamaged tubes and those containing impact damage are represented in the bar chart shown in Figure 4-14.
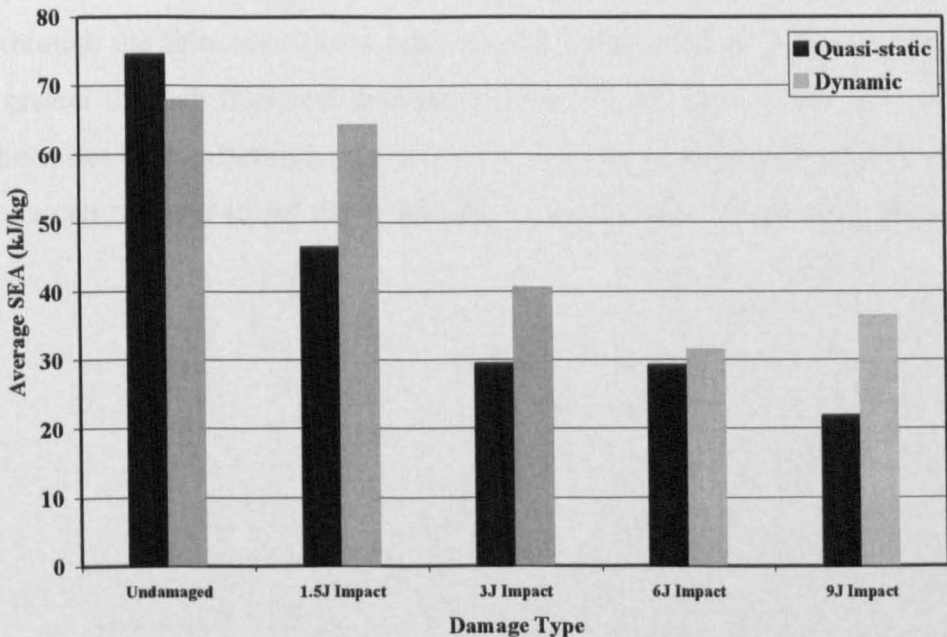


Figure 4-14 – Bar chart showing average SEAs for the quasi-static and dynamic tests of the small CoFRM tubes containing impact damage

Overall, it can be seen that for both the static and dynamic tests the impact damage has had a major effect on the energy absorption potential of the tubes. The only specimens that were relatively unaffected were the dynamically tested tubes containing 1.5J impact damage, with an SEA of 64.28kJ/kg and percentage drop of 5.3%. All other specimens failed unstably with SEA reductions of between 37.6% and 70.6%. Generally the effect of the impact damage caused greater reductions in the static than the dynamic tests.

The optical microscopy shown in Figure 4-15 show cross-sections of small CoFRM tubes containing impact damage before and after testing (see Section 3.6.4). The 1.5J and 3J impacts have deformed the surface of the tube with little damage to the rest of the sample. When 6J of damage was added the surface of the tube starts to crack showing compressive failures. With 9J of damage more evidence of compressive failure was seen at the surface and the matrix damage caused fibres to become unconstrained.

Sections 1 and 2 show cross-sections at the damage point and then 20mm round the tube for part-tested samples containing impact damage. All the sections are for statically tested tubes and show the cracks that formed during the unstable failure of the samples. Section 1 through the 1.5J sample shows that the crack promoted shear failure through the thickness of the tube. As the impact energy increases, the tubes have a greater through thickness damage and the failure mode is less obvious. The failure becomes clearer through section 2, which is away from the damage point, and the cracks can be seen to be shear failures as in the case of section 1 of the 1.5J sample.
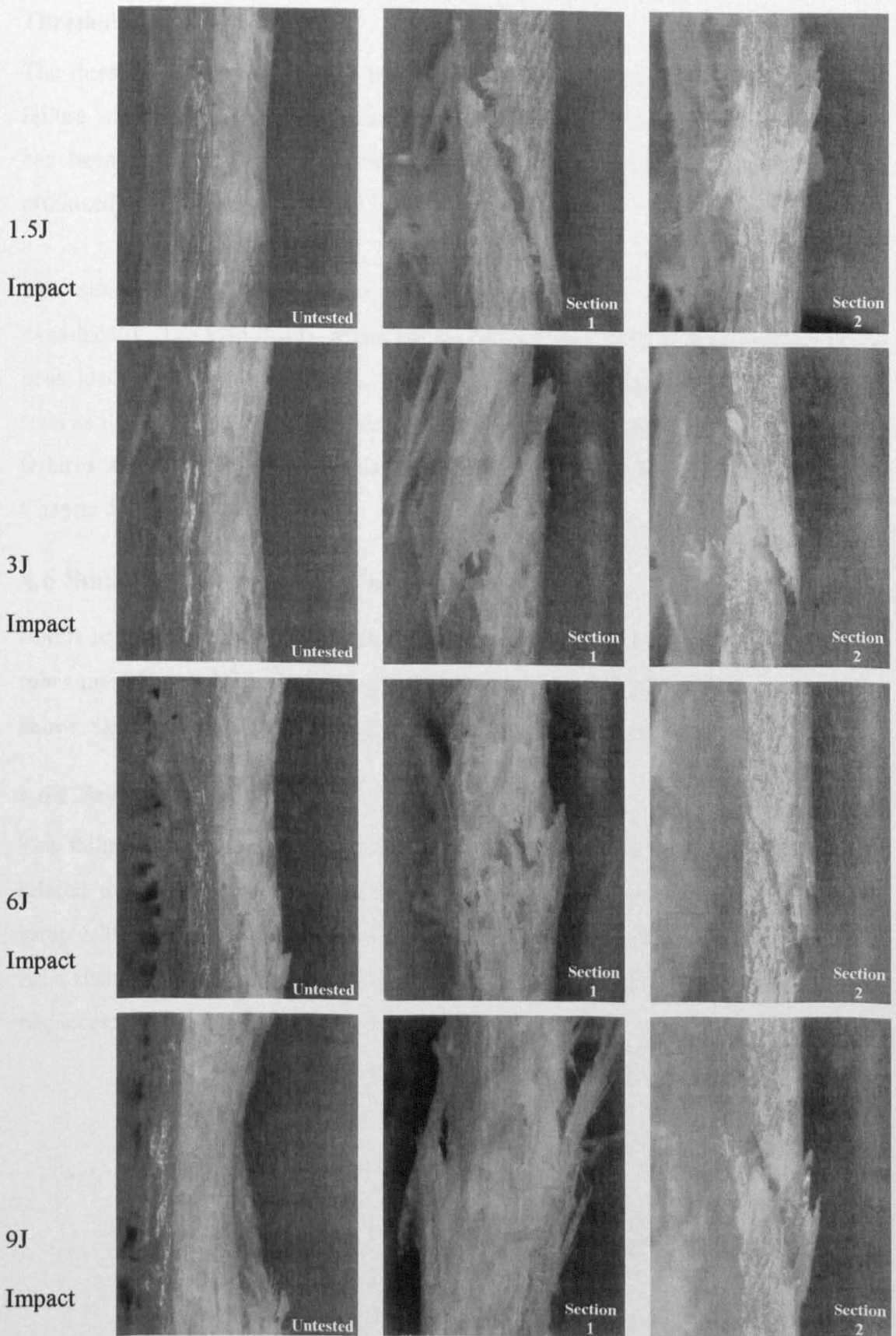
**Figure 4-15 – Microscope images (5 times magnification) of impacted 38.1mm diameter CoFRM tube samples before axial crush and at two sections after part testing. Section 1 was taken through the centre of the damage area and Section 2 at 20mm circumferentially round the tube**

**Thresholds**

The threshold of impact damage that could be added before the risk of an unstable failure was a 1.5J impact, and this applied only for the dynamic tests. No threshold has been found for the quasi-statically tested tubes as an unstable failure was produced by all the impacts added in these tests.

The small CoFRM tubes have shown more damage tolerance when tested dynamically. The load-displacement curves (Appendix 7.7-7.13) display lower initial peak loads and mean crush loads. The samples generally cracked at the start of the tests as the load was rising and this reduction in peak load may cause fewer unstable failures and thereby higher damage tolerance. This will be discussed further in Chapter 5.

## 4.6 Small Braided/Norpol Tube Tests

In this section, results are presented for the tubular crush tests of the 38.1mm diameter tubes manufactured from braided glass fibre at ±45° and Norpol resin. Appendix 7.5 shows SEAs and load-displacement curves for all tests conducted.

### 4.6.1 Failure Modes

The failure modes seen in the quasi-statically tested small braided tubes could be related to the apparent SEAs of the tubes. The undamaged tubes were the only samples that failed stably via a buckling mode in this case. This mode yielded a lower SEA than a progressive splaying crush and caused a characteristic undulating load-displacement curve (Figure 4-16).
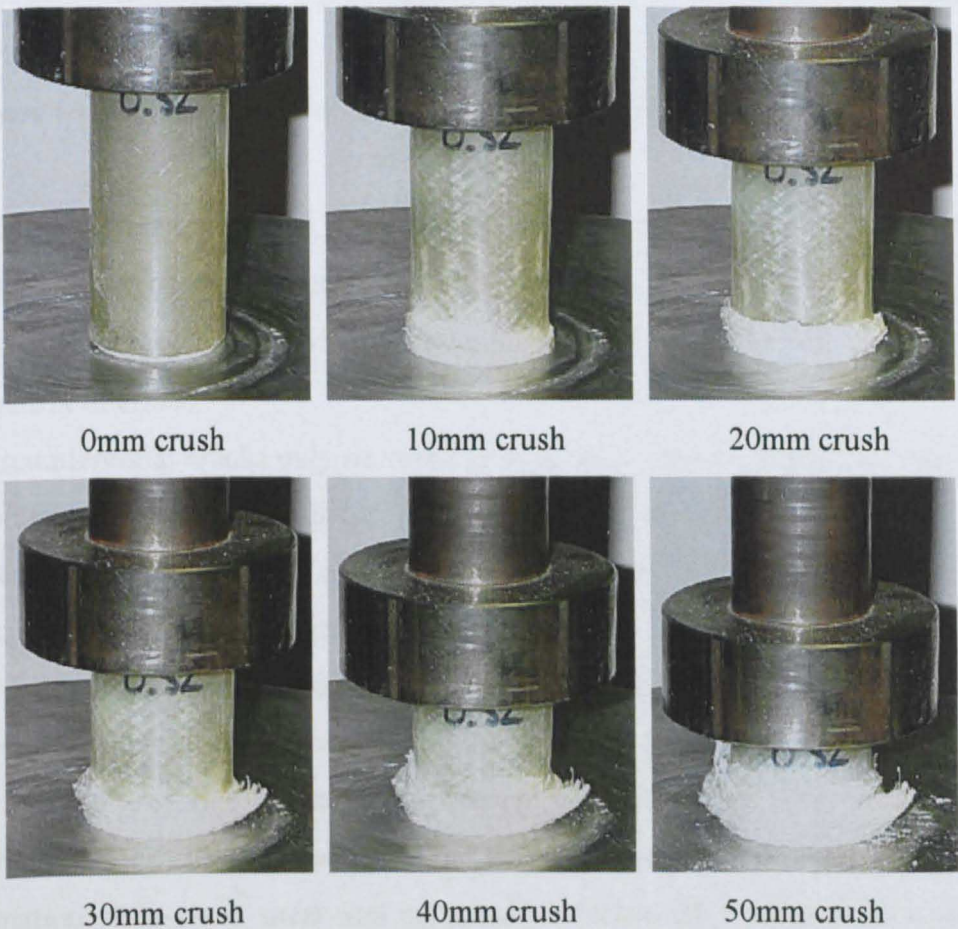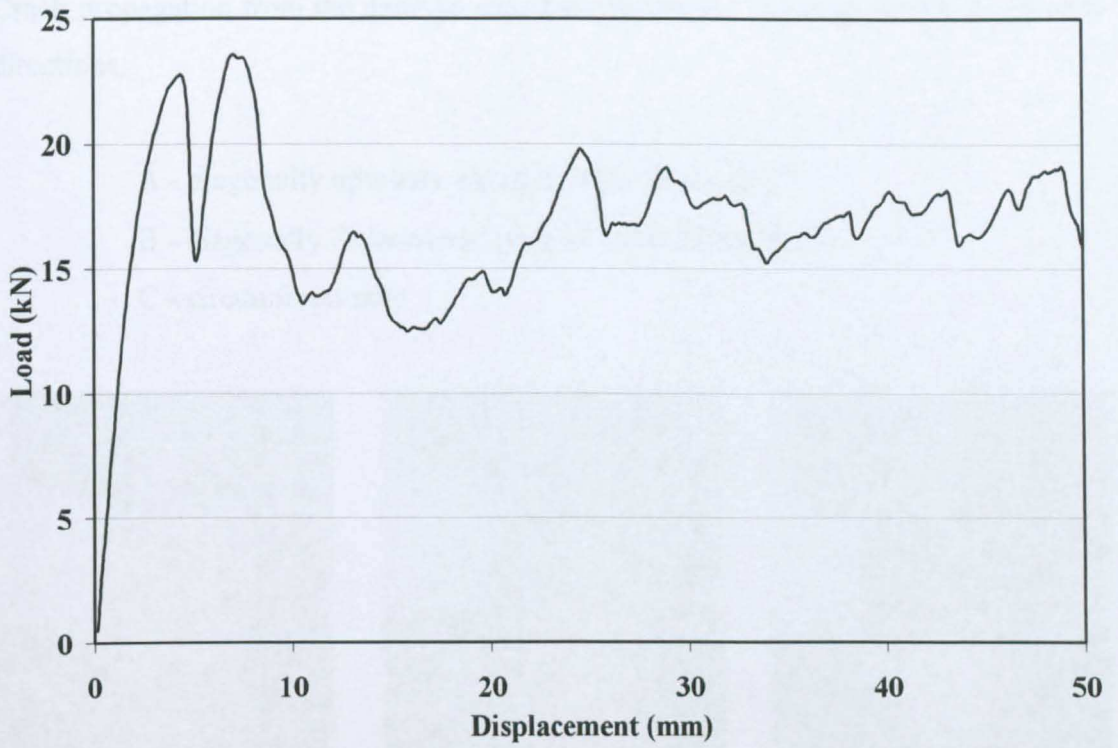
Figure 4-16– Load-displacement curve and images through crush for an undamaged braided small, 38.1mm diameter, tube tested at 5mm/min

Crack propagation from the damage zone (see Figure 4-17) was generally in one of 3 directions:

A - diagonally upwards, parallel to the fibres at 45°

B - diagonally downwards, parallel to the fibres at 45°

C - circumferentially



| Two type A fractures | Two type B fractures | Two type C fractures |

**Figure 4-17 – Crack propagation types in the 38.1mm diameter braided tubes containing simulated damage**

In all cases there were at least two cracks that initiated from the damage area and the most common were the diagonal, in-plane shear cracks. This is due to the fact that the braid was manufactured at ±45° and the cracks tended to follow the relatively weak fibre/matrix interface.

The circumferential cracks only occurred in samples containing higher damage levels, the 16mm hole and the 9J impact, and were caused by compressive failure. These samples had the highest stress concentration factors (see Chapter 5) and so the highest maximum stresses at the edges of the holes. Cracks initiated here and propagated circumferentially rather than following the fibre direction.

The graph in Figure 4-18 shows the SEAs achieved by each combination of crack types and the grey line indicates the average SEA for each. The results are quite scattered but it can be seen that the tubes that failed via in-plane shear (B + B) or a combination of in-plane shear and compressive failure (B + C) generally achieved higher SEAs than other combinations because the in-plane shear failure (type A) propagated at 45°. This eliminated most of the tube from any subsequent crushing.
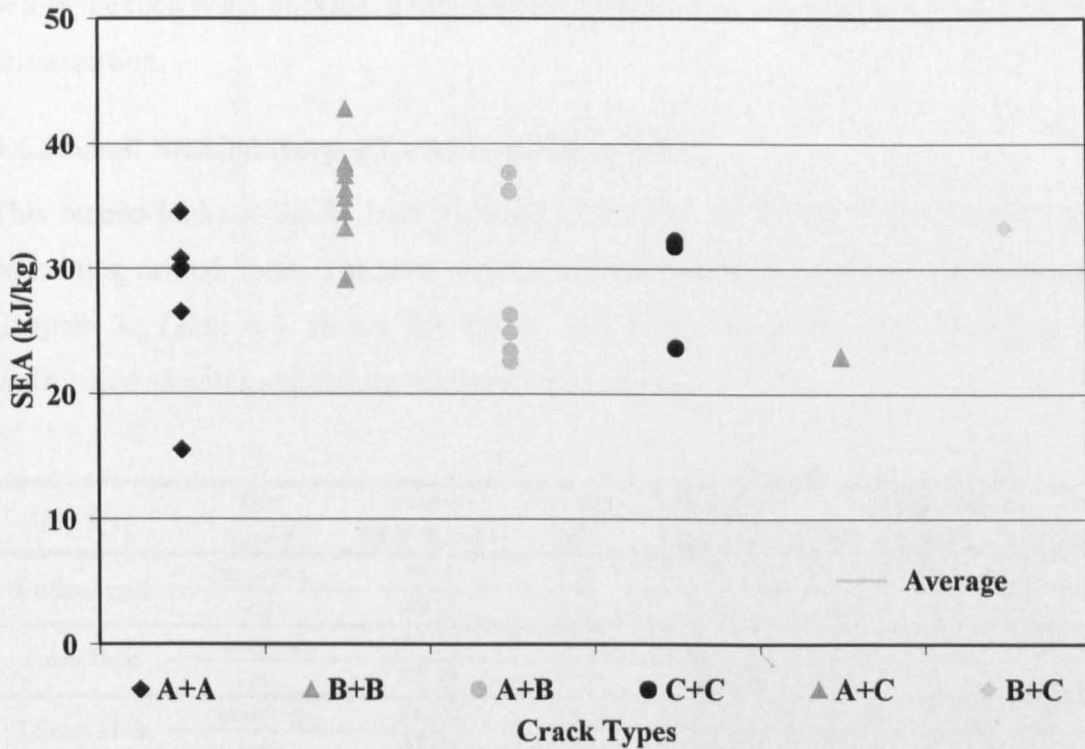
Figure 4-18 – SEAs vs. crack propagation types for small braided tubes containing simulated damage

### 4.6.2 Undamaged Small Braided/Norpol Tubes

The undamaged, braided tubes when crushed quasi-statically and dynamically gave SEAs of 38.8kJ/kg and 48.38kJ/kg respectively with standard deviations of 3.84% and 1.41%. The statically crushed tubes failed by buckling which gave a load-displacement curve that was less uniform than for the CoFRM small tubes. The dynamic tests however gave a much smoother curve, failing progressively by splaying and the SEA increased by 24.69% when crushing dynamically compared to the static tests. This difference was attributed to the different failure modes. The buckling occurred due to circumferential failures in the material causing the tube walls to buckle. The absence of axial fibres reduced the axial strength of the tube and this may help to explain the buckling failures. This lower SEA is mainly due to the elimination of the central wall crack as this had been found to be one of the principal energy absorbing mechanisms of the splaying failure [6]. Dynamically, the change in crush mode to splaying may be attributed to the matrix, which increases the apparent compressive strength, allowing a central wall crack and stable crush zone to form

before the tube walls buckled. Examinations of the crush zone (Chapter 5.1.1) support this assertion.

### 4.6.3 Small Braided/Norpol Tubes Containing Holes

This section looks at the 38.1mm diameter, 2mm wall thickness, braided small tubes containing drilled holes. The tests were conducted and holes applied as described in Chapter 3. Table 4-8 shows the SEAs, percentage drops in SEA compared to undamaged samples and failure modes for these tests.

| Hole Size | Test Speed | Average SEA (kJ/kg) | Std. Dev. (%) | Percentage Drop (%) | Failure Mode | | |
|-----------|------------|---------------------|---------------|---------------------|--------|---------|----------|
|           |            |                     |               |                     | Stable | Folding | Unstable |
| Undamaged | 5mm/min | 38.80 | 3.84 | - | - | 3 | - |
|           | 5m/s    | 48.38 | 1.41 | - | 3 | - | - |
| 5mm Hole  | 5mm/min | 26.48 | 41.72 | 31.76 | - | - | 3 |
|           | 5m/s    | 46.92 | 4.11 | 3.02 | 3 | - | - |
| 7.5mm Hole | 5mm/min | 36.60 | 3.42 | 5.67 | - | - | 3 |
|           | 5m/s    | 47.04 | 1.20 | 2.76 | 3 | - | - |
| 10mm Hole | 5mm/min | 29.35 | 20.93 | 24.36 | - | - | 3 |
|           | 5m/s    | 45.74 | 3.96 | 5.45 | 3 | - | - |
| 12.5mm Hole | 5mm/min | 34.68 | 4.37 | 10.62 | - | - | 3 |
|           | 5m/s    | 36.92 | 10.57 | 23.69 | - | - | 3 |
| 16mm Hole | 5mm/min | 27.29 | 16.99 | 29.68 | - | - | 3 |
|           | 5m/s    | 31.59 | 1.23 | 34.69 | - | - | 3 |

**Table 4-8 - Average SEAs, percentage drop in SEA and failure modes for the 38.1mm diameter braided tubes containing drilled holes centred at 30mm from the chamfer, tested at 5mm/min and 5m/s**

Quasi-statically, the scatter was large with the largest reduction in SEA seen in the tubes containing a 5mm hole, a drop of 31.76%. The lowest drop in SEA was 5.67% seen in the tubes containing a 7.5mm hole. The differences were attributed to the failure mode and the crack formation seen and is discussed earlier in section 4.6.1. Dynamically, small drops were noted in SEA, up to just 5.45% for the tubes containing a 10mm hole. Above the 10mm, the SEAs dropped sharply (23.69% and 34.69% for the 12.5mm and 16mm holes respectively).

### 4.6.4 Braided Small Tubes Containing Impact Damage

Table 4-9 shows the average SEAs, failure modes and percentage drops in SEA for the small braided tubes containing impacts.

| Impact Size | Test Speed | Average SEA (kJ/kg) | Std. Dev. (%) | Percentage Drop (%) | Failure Mode | | |
|---|---|---|---|---|---|---|---|
| | | | | | Stable | Folding | Unstable |
| Undamaged | 5mm/min | 38.80 | 3.84 | - | - | 3 | - |
| | 5m/s | 48.38 | 1.41 | - | 3 | - | - |
| 1.5J Impact | 5mm/min | 32.59 | 28.18 | 16.00 | - | - | 3 |
| | 5m/s | 46.46 | 7.81 | 3.97 | 3 | - | - |
| 3J Impact | 5mm/min | 34.50 | 9.99 | 11.09 | - | - | 3 |
| | 5m/s | 47.86 | 1.98 | 1.06 | 3 | - | - |
| 6J Impact | 5mm/min | 27.49 | 12.99 | 29.16 | - | - | 3 |
| | 5m/s | 38.93 | 8.58 | 19.53 | - | - | 3 |
| 9J Impact | 5mm/min | 28.00 | 28.99 | 27.84 | - | - | 3 |
| | 5m/s | 39.34 | 18.50 | 18.68 | - | - | 3 |

**Table 4-9 - Average SEAs, percentage drop in SEA and failure modes for the 38.1mm diameter braided tubes containing impacts centred at 30mm from the chamfer, tested at 5mm/min and 5m/s**

The braided small tubes with pre-test impact damages of 1.5J, 3J, 6J and 9J all failed unstably in the quasi-static tests. The fracture mode caused large differences in SEAs between samples and is discussed further in Section 5.1.

Dynamically, the tubes containing 1.5J and 3J impacts had insignificant reductions in SEA. The largest SEAs seen by a single sample actually occurred in the tubes containing a 1.5J impact for both the quasi-static and dynamic tests. Larger drops in average SEA were noted as the pre-test impact energy level was increased.

**Thresholds**

No threshold values were found for the statically tested braided tubes, all specimens provided an unstable failure mode with cracks propagating from the hole or impact site. However, dynamically, a hole of 10mm in diameter or an impact of 3J could be added without a change to the failure mode or an unstable crush being produced.

## 4.7 Comparisons of Tube Tests

### 4.7.1 Effect of Resin Type

In order to see the effect of the resin type the large Crystic and CoFRM tubes with a 4mm wall were compared. Figure 4-19 shows a bar chart of the average SEAs for these tests.
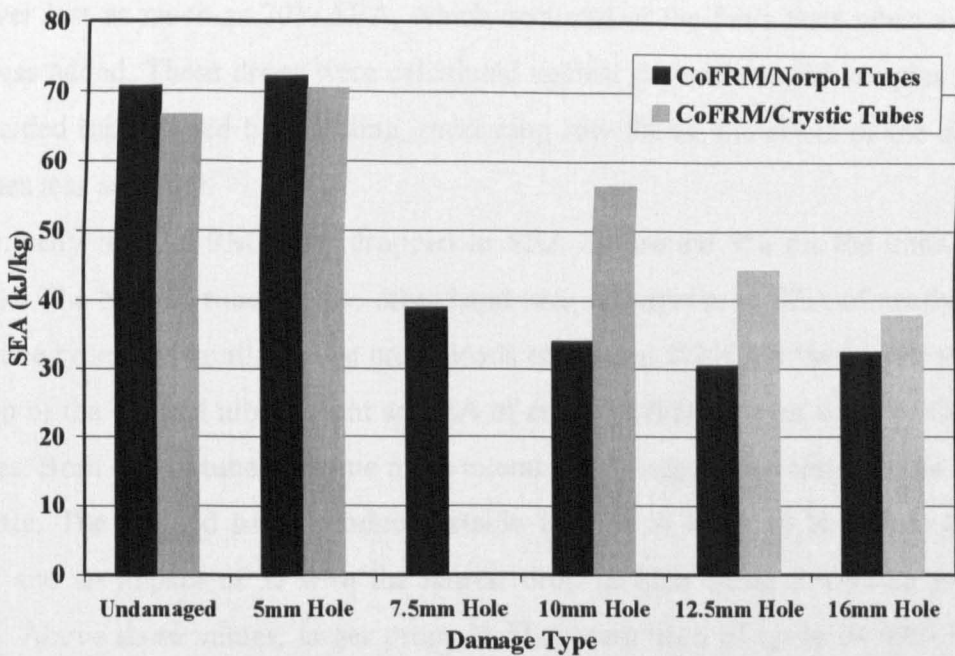
Figure 4-19– Comparison of the average SEAs for the large (89.1mm diameter, 2mm wall thickness) CoFRM tubes, manufactured using Crystic and Norpol resins tested at 5mm/min

The main difference between the two tube types was the resin used for manufacture, Crystic in the large Crystic tubes and Norpol in the Large CoFRM tubes. The resins had comparable tensile moduli at 3.580GPa and 3.700GPa for the Crystic and Norpol respectively. The strains to failure were 2.5% for the Crystic resin and 3.5% for the Norpol. When considering the undamaged samples both tube types performed similarly with the large tubes producing a slightly higher SEA. As the damage is introduced the large Crystic tubes showed more damage tolerance and gave higher SEAs for each of the hole sizes tested. This was attributed to the resin type as all other material and manufacture properties were identical. The lower SEA and hence lower crush load of the Crystic tubes has made them more tolerant to damage.

### 4.7.2 Effect of Fibre Architecture

The CoFRM and braided 38.1mm diameter tubes containing holes at 30mm and pre-test impact damage of between 1.5J and 9J were compared to examine the effects of fibre architecture. The results for the CoFRM tubes are shown in Table 4-5 (holes) and Table 4-7 (impacts), and for the braided tubes in Table 4-8 (holes) and Table 4-9 (impacts).

The reductions in SEA for the braided tubes were relatively low with a maximum of 32% for the tubes containing a 5mm hole tested at 5mm/min. The CoFRM tubes

however lost as much as 70% SEA, which occurred in the 5m/s tests when a 16mm hole was added. These drops were calculated against the undamaged samples and as the braided tubes failed by buckling, producing low SEAs, the effect of the damage becomes less apparent.

Dynamically the CoFRM tubes dropped in SEA by around 9% for the undamaged samples. The braided tubes on the other hand saw an increase in SEA of nearly 25%. Both tube types had similar mean crush loads of around 20kN but the higher volume fraction of the braided tubes meant an SEA of around 20kJ/kg lower than the CoFRM samples. Both sets of tubes became more tolerant to damage when tested at the higher load rate. The braided tubes produced stable failures at 5m/s up to a hole size of 10mm and an impact of 3J with the largest drop in SEA being 5.45% up to these values. Above these values, larger drops in SEA were seen of up to 34.69% for the samples containing a 16mm hole. The CoFRM samples remained unaffected up to a 5mm hole and for a 1.5J impact with samples containing more damage causing drops in SEA of up to 71.8%, as seen in the tubes containing a 16mm hole.

### 4.7.3 Comparison of All Tube Tests

Table 4-10 shows the average SEAs for all tube types, containing holes at 30mm from the chamfer and impact damage.

| Wall Thickness (mm) | 2 | | 2 | | 4 | 4 | 3.33 | 2.67 |
|---|---|---|---|---|---|---|---|---|
| Material | CoFRM | | ± 45° Braid | | CoFRM | CoFRM | CoFRM | CoFRM |
| Resin | Norpol | | Norpol | | Crystic | Norpol | Norpol | Norpol |
| Tube Diameter (mm) | 38.1 | | 38.1 | | 89.1 | 89.1 | 89.1 | 89.1 |
| t/D | 0.0525 | | 0.0525 | | 0.0449 | 0.0449 | 0.0374 | 0.0300 |
| Test Type | Static | Dynamic | Static | Dynamic | Static | Static | Static | Static |
| Undamaged | 74.55 | 67.85 | 38.80 | 48.38 | 66.64 | 70.68 | 66.97 | 63.04 |
| 5mm Hole | 58.36 | 60.02 | 26.48 | 46.92 | 70.40 | 72.18 | 70.05 | 63.57 |
| 7.5mm Hole | 40.67 | 51.78 | 36.60 | 47.04 | | 38.90 | 61.70 | 43.11 |
| 10mm Hole | 21.97 | 54.33 | 29.35 | 45.74 | 56.45 | 34.06 | 46.66 | 34.68 |
| 12.5mm Hole | 25.68 | 20.07 | 34.68 | 36.92 | 44.28 | 30.41 | 33.34 | 27.09 |
| 16mm Hole | 22.32 | 19.10 | 27.29 | 31.59 | 37.75 | 32.39 | 30.42 | 20.51 |
| 1.5J Impact | 46.50 | 64.28 | 32.59 | 46.46 | | 69.91 | 67.45 | 64.78 |
| 3J Impact | 29.51 | 40.60 | 34.50 | 47.86 | | 70.19 | 56.23 | 47.47 |
| 6J Impact | 29.31 | 31.43 | 27.49 | 38.93 | | 55.75 | 37.24 | 47.92 |
| 9J Impact | 21.90 | 36.36 | 28.00 | 39.34 | | 43.60 | 26.01 | 24.59 |

Table 4-10– Average SEAs for the large and small tubes containing impact damage and holes centred at 30mm from the chamfer

When examining the quasi-statically tested, undamaged CoFRM/Norpol tube results, it can be seen that as the t/D ratio reduces, the SEA also drops. The highest SEA value is seen in the 2mm walled small tubes with a t/D ratio of 0.0525 and SEA of 74.55kJ/kg dropping for the large 2.67mm walled samples with a t/D of 0.0300 and SEA of 63.04kJ/kg. This is similar to the effect seen by Hamada and Ramakrishna [4] who showed that SEA for carbon/PEEK tubes increased up to a t/D value of around 0.05 before levelling off. Figure 4-20 shows the variation of SEA with t/D ratio for the CoFRM/Norpol tubes and carbon/PEEK tubes tested by Hamada and Ramakrishna.
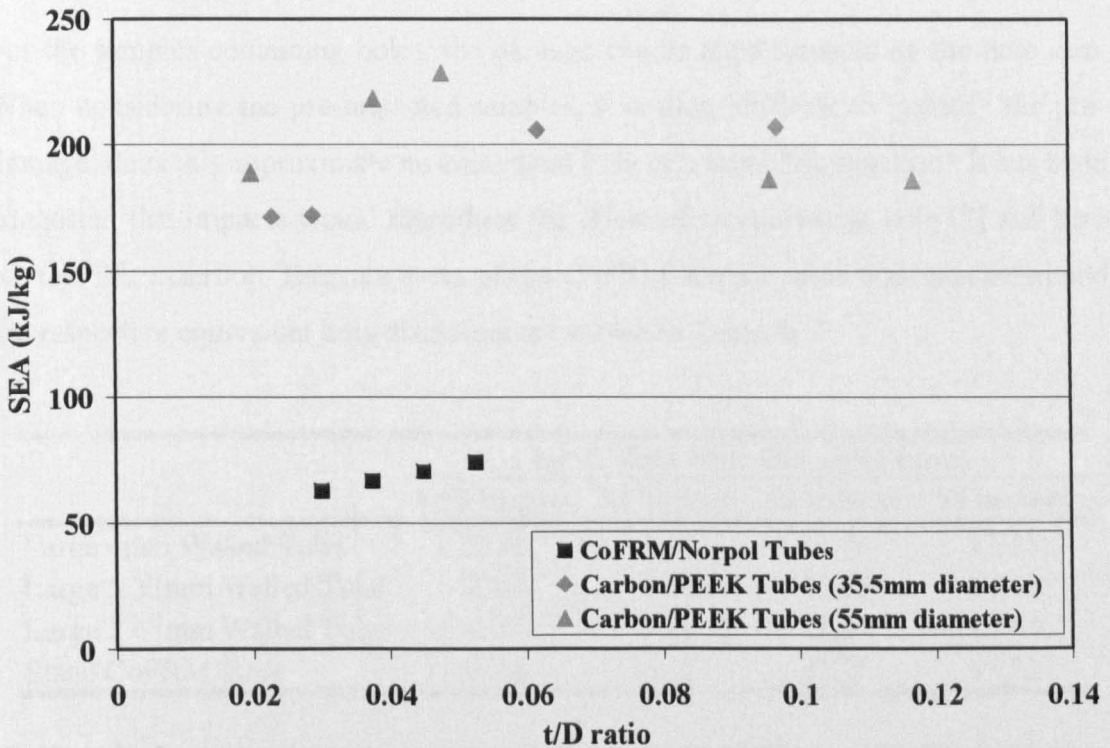


Figure 4-20 – SEAs vs. t/D ratio for CoFRM/Norpol tubes crushed at 5mm/min and Carbon/PEEK tubes crushed at 1mm/min [4]

## Threshold Values

The damage thresholds for each of the tubes tested here are shown in Table 4-11.

| Wall Thickness (mm) | 2 | | 2 | | 4 | 4 | 3.33 | 2.67 |
|---|---|---|---|---|---|---|---|---|
| Material | CoFRM | | ± 45° Braid | | CoFRM | CoFRM | CoFRM | CoFRM |
| Resin | Norpol | | Norpol | | Crystic | Norpol | Norpol | Norpol |
| Tube Diameter (mm) | 38.1 | | 38.1 | | 89.1 | 89.1 | 89.1 | 89.1 |
| t/D | 0.0525 | | 0.0525 | | 0.0449 | 0.0449 | 0.0374 | 0.0300 |
| Threshold Hole Size | None | 5mm | None | 10mm | 5mm | 5mm | 5mm | 5mm |
| Threshold Impact Amount | Found | 1.5J | Found | 3J | | 3J | 1.5J | 1.5J |

Table 4-11 – Damage thresholds of drilled holes and pre-test impact damage for each tube type

Looking at the CoFRM tubes, the results do not show any trend between t/D ratio and damage tolerance. However, wall thickness does seem to have an affect with the thicker walled tubes being more tolerant to applied damage. An increase in test rate increases the damage tolerance of the small, 2mm walled tubes. For both the CoFRM and braided tubes, no threshold was found when tested quasi-statically, but at a test rate of 5m/s hole sizes of 5mm and an impact of 1.5J could be added to the CoFRM tubes without causing unstable failures. For the braided tubes the damage thresholds were a 10mm hole and a 3J impact when tested dynamically.

### 4.7.4 Quantifying Damage

For the samples containing holes, the damage can be approximated by the hole size. When considering the pre-impacted samples, it is more difficult to quantify the pre-damage; does this approximate an equivalent hole or a local delamination? It has been suggested that impacts would reproduce the effect of an equivalent hole [7] and here we test this assertion. Damage areas of the CoFRM/Norpol tubes were measured and the respective equivalent hole diameters are shown in Table 4-12.

|  | Equivalent Hole Diameter (mm) | | | |
|  | 1.5J impact | 3J impact | 6J impact | 9J impact |
|---|---|---|---|---|
| Large 4mm Walled Tube | 2.19 | 7.25 | 11.08 | 13.23 |
| Large 3.33mm Walled Tube | 3.87 | 7.96 | 11.78 | 14.63 |
| Large 2.67mm Walled Tube | 4.82 | 8.74 | 12.63 | 15.44 |
| Small CoFRM Tube | 8.35 | 11.26 | 15.25 | 15.82 |

Table 4-12 – Equivalent hole diameters for the impacted large CoFRM and small CoFRM tubes

By comparing the damage thresholds of the impacted samples to those of the drilled holes (Table 4-11) it was found that the equivalent hole diameters matched the damage thresholds found here. For example, the large 4mm walled tubes had a damage threshold of a 5mm diameter drilled hole and a 3J impact. The equivalent hole diameter of the 3J impact was 7.25mm which fell between the range of drilled holes tested. This was found for all samples and so the pre-impact damage seems to approximate an equivalent hole. Chapter 5 discusses this further.

## 4.8 Tensile Coupon Tests

The next section discusses the results obtained from the static and dynamic tensile tests for undamaged specimens and those containing holes as described in Section 3.5.4. These tests will help in understanding the effects of stress concentration factors by comparing the experimental results to common theory. Stress-displacement curves are presented in Appendix 7.6. The average failure stresses and displacements for these coupon tests are shown in Table 4-13. The failure stresses were calculated by taking the failure load and dividing by the reduced cross-sectional area of the sample.

| Damage Type | Test Speed | Failure Stress (MPa) | Std.Dev. (%) | Failure Displacement (mm) | Std.Dev. (%) |
|---|---|---|---|---|---|
| Undamaged | 5mm/min | 161.09 | 9.45 | 4.10 | 3.83 |
| | 5m/s | 363.79 | 10.11 | 3.95 | 10.74 |
| 5mm Hole In Centre | 5mm/min | 121.31 | 7.51 | 2.88 | 6.08 |
| | 5m/s | 191.95 | 15.40 | 2.99 | 0.39 |
| 10mm Hole in Centr | 5mm/min | 84.67 | 12.13 | 2.03 | 12.73 |
| | 5m/s | 78.61 | 13.16 | 2.08 | 7.08 |

Table 4-13 – Average failure stresses and displacements of the statically and dynamically tested tensile coupons

### 4.8.1 Undamaged Tensile Specimens

The static tensile tests for the undamaged specimens produced an average failure stress of 161MPa. The dynamic average was 364MPa, a 125% increase. The specimens failed at very similar displacements of around 4mm. Figure 4-21 shows the undamaged samples pre-test and after quasi-static and dynamic tests.
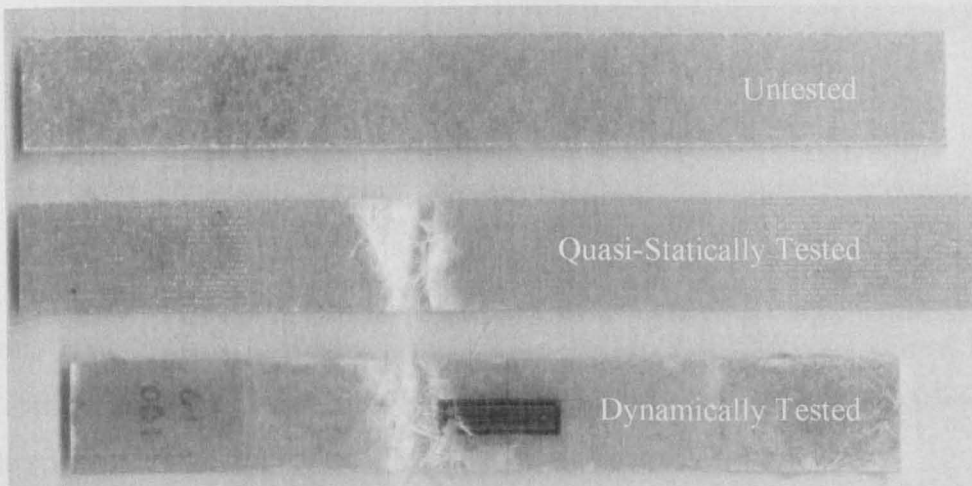


Figure 4-21 – Undamaged tensile specimens

On examination of the tested tensile samples it could be seen that there were fibre pullouts and matrix fragmentation in both the static and dynamically tested samples. This implies that the fibre-matrix bond has been exceeded before the tensile failure strength of the composite has been reached. The apparent strength increased with an increase to test speed and is consistent with the rate dependency reported by Fernie [8] and Gilat et al [9] who attributed the strain rate dependence to matrix strength. Okoli [10] also recorded increases in tensile strength as strain rate increased and attributed the rise to increased matrix yielding.

### 4.8.2 Tensile Specimens Containing a 5mm Hole

The introduction of a 5mm hole in the tensile specimen caused drops in failure load both statically and dynamically. The static results dropped by 25% to 12.1kN and the dynamic by 47% to 19.2kN. The imposed reduction in cross-sectional area is 20% and is close to the 25% drop in failure load seen in the static tests. However the hole had a disproportionate effect on the dynamic results. Figure 4-22 shows the tensile specimens containing a 5mm hole before and after testing.
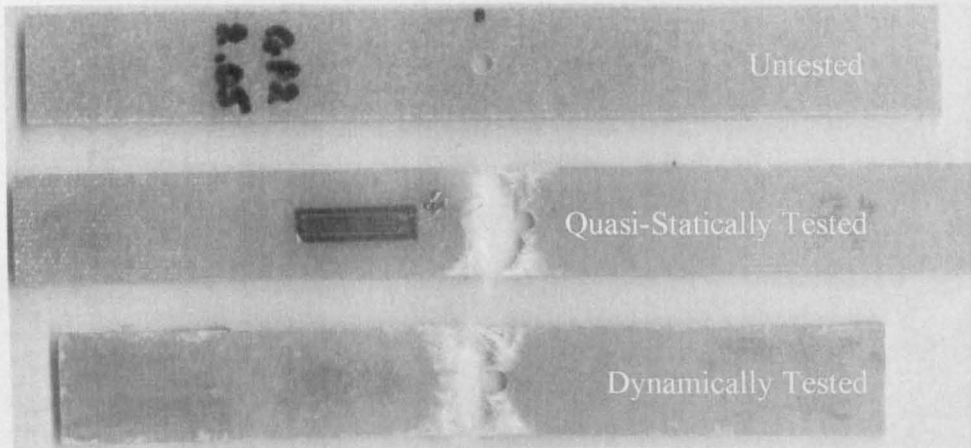


Figure 4-22 – Tensile specimens containing a 5mm hole

### 4.8.3 Tensile Specimens Containing a 10mm Hole

The 10mm hole reduced the failure stress for the static tests by 47% to 85kN and dynamic tests by 78% to 79kN. The imposed reduction in cross-sectional area was 40% and the static tests show a reduction of around that value. Figure 4-23 shows the tensile specimens pre-test and after quasi-static and dynamic testing.
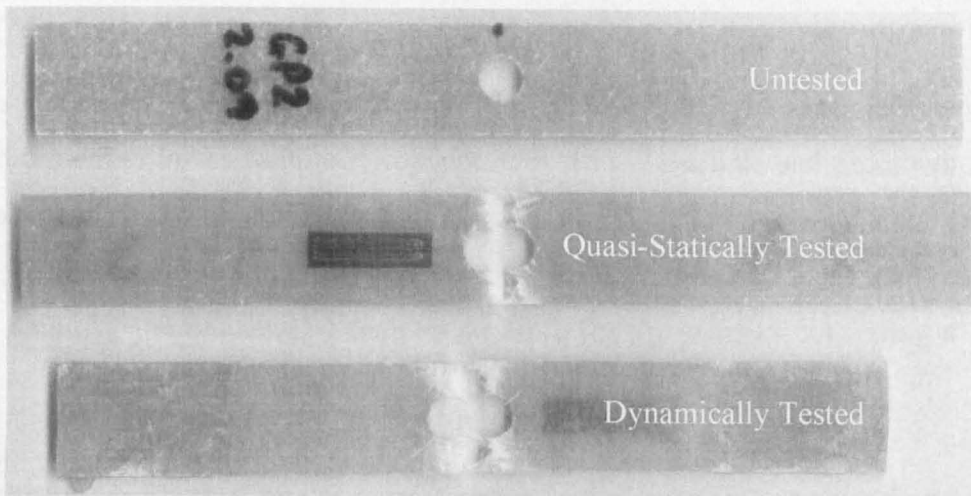
Figure 4-23– Tensile specimens containing a 10mm hole

When considering the overall results of the tensile tests (Figure 4-24) it can be seen that dynamically, the failure load of the undamaged samples was just over double that of the quasi-static tests. When a 5mm hole was added there was still an increase in failure load but of just 60%. The addition of the 10mm hole caused the dynamic failure load to be lower than in the quasi-static sample.
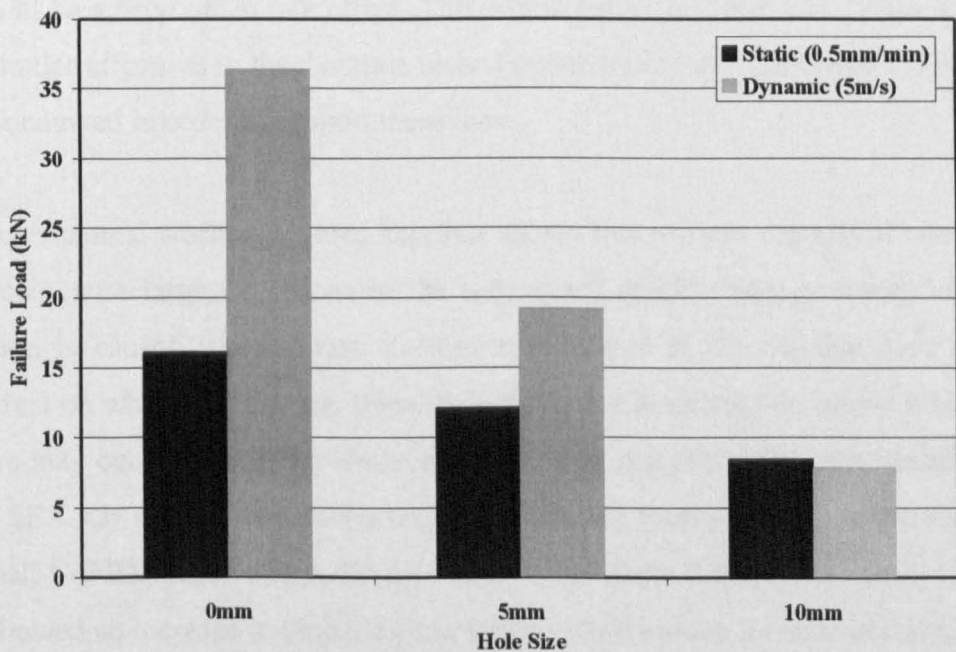


Figure 4-24– Bar chart showing the average failure loads of the quasi-static and dynamic tensile tests containing holes

## 4.9 Conclusions

Stress concentrators cause samples to fail prematurely. As load increases, the maximum stress in the sample is concentrated around the hole and deformation and displacement of the specimens is concentrated in this vicinity. Larger holes produce greater stress concentration; this is shown by the reduction of failure displacements from 4mm for the undamaged samples to 2mm for the samples containing a 10mm hole.

The combined effects of rate and stress concentration factor are explained as follows. Firstly, as the effective test length is reduced by the stress concentrations the rate effects may become negated. This is supported by the results. Since the damage is concentrated in an increasingly smaller volume, the stress concentrator may effectively increase the local strain rate, as a smaller length of specimen is displacing the same amount as the full sample in the same time. The holes are effectively multiplying the strain rate and this increase in rate will be negligible in the quasi-static tests as the original speed is so low. However multiplying the dynamic strain rate will have a significantly greater effect. It is possible that at significantly higher strain rates there will be a drop off in rate effect. This would cause the 5mm and 10mm holes to have similar effects as in the dynamic tests. Further testing at higher rates would need to be conducted in order to support these ideas.

The experimental work conducted here has shown that pre-test damage of composite tubes can cause large reductions to the subsequent specific energy absorption. The reduction is caused when a fast fracture is produced at the damage zone and is dependant on when and how the fracture forms. Damage thresholds, above which fast fracture may occur, have been identified in all tests except the statically tested small tubes. SEA has been shown to increase for the small braided tubes and decrease for the small CoFRM tubes with a change in test speed from 5mm/min to 5m/s. Coupon tests showed an increase to tensile failure stress with the same increase in test rate and this effect was reduced with the addition of stress concentrators. These findings will be examined further in the following chapter.

## 4.10 Chapter 4 References

[1] Farley GL and Jones RM, Crushing Characteristics of Continuous Fibre-Reinforced Composite Tubes, Journal of Composite Materials, Vol.26, No.1, pp37-50, 1992.

[2] Habib FA, A new method for evaluation the residual compression strength of composites after impact, Composite Structures, Vol.53, pp309-316, 2001.

[3] Mamalis AG, Monolakos DE, Demosthenous GA and Ioanndis MB, Crashworthiness of Composite Thin-Walled Structural Components, Technomic Publishing Company Inc., 1998.

[4] Hamada H and Ramakrishna S, Scaling Effects in the Energy Absorption of Carbon-fiber/Peek Composite Tubes, Composites Science and Technology, Vol. 55, pp211-221, 1995.

[5] Chadwick MM and Caliskan AG, Crush mechanisms observed in polymeric composite tubes, unknown source, pp453-462.

[6] Farley GL, Relationship Between Mechanical-Property and Energy-Absorption Trends for Composite Tubes, NASA Technical Paper3284, pp1-13, December 1992.

[7] Abrate S, Impact on Composite Structures, Cambridge University Press, Cambridge, 1998.

[8] Fernie R, PhD Thesis, Loading Rate Effects on the Energy Absorption of Tubular Crash Structures, University of Nottingham, 2002.

[9] Gilat A, Goldberg RK and Roberts GD, Experimental study of strain-rate-dependent behavior of carbon/epoxy composite, Composites Science and Technology, Vol.62, pp1469-1476, 2002.

[10] Okoli OI, The effects of strain rate and failure modes of fibre reinforced composites, Composite Structures, vol.54, pp299-303, 2001.

# 5.0 Discussion

The previous chapter discussed the experimental results of the tubular crush tests and threshold values of damage were found for each tube type, above which tubes crushed unstably with reductions in SEA. It was shown that the damage tolerance of tubes increased with an increase in test rate from 5mm/min to 5m/s (small CoFRM tubes). In an attempt to understand this effect, the following sections discuss the crush modes observed in the static and dynamically tested tubes. By calculating stress concentration factors, the amounts of damage can be generalised with the aim of predicting when and how tubes containing damage will fail unstably.

## 5.1 Examination of Crush Zone

### 5.1.1 Scans and Micrographs of Crush Zone

Scans of potted, statically and dynamically tested small CoFRM tubes are shown in Figure 5-1. The tubes contained no pre-damage and one sample of each test speed was potted and examined. As can be seen from the scans, the fronds in the statically tested tube show that the fibres have remained constrained, within the matrix, and bend with a large radius of curvature. In comparison, those of the dynamically tested tube show that the resin has become fragmented leaving the fibres unconstrained and more compliant. This allows the fronds to bend more easily and remain closer to the tube wall.

The micrographs in Figure 5-2 show an obvious crack in the tube wall of the dynamically tested tube and a smaller one to its side, whereas statically the crack is thinner and less obvious. These are interlaminar cracks that have formed between layers of mat. The fracture toughness would be lower between layers as there are no supporting fibres and cracks can form more easily. The lengths of these wall cracks ($L_c$) were measured and seen to vary on each side of the tube. The statically tested sample had cracks of 7.27mm and 4.9mm whilst the dynamic sample had cracks of 4.36mm and 6mm as shown in Figure 5-1.

The micrographs and scans are only representative of one point around the circumference of the tube. As such, they may not be representative of the entire specimen, with particular reference to the values of $L_c$ that have been measured here.
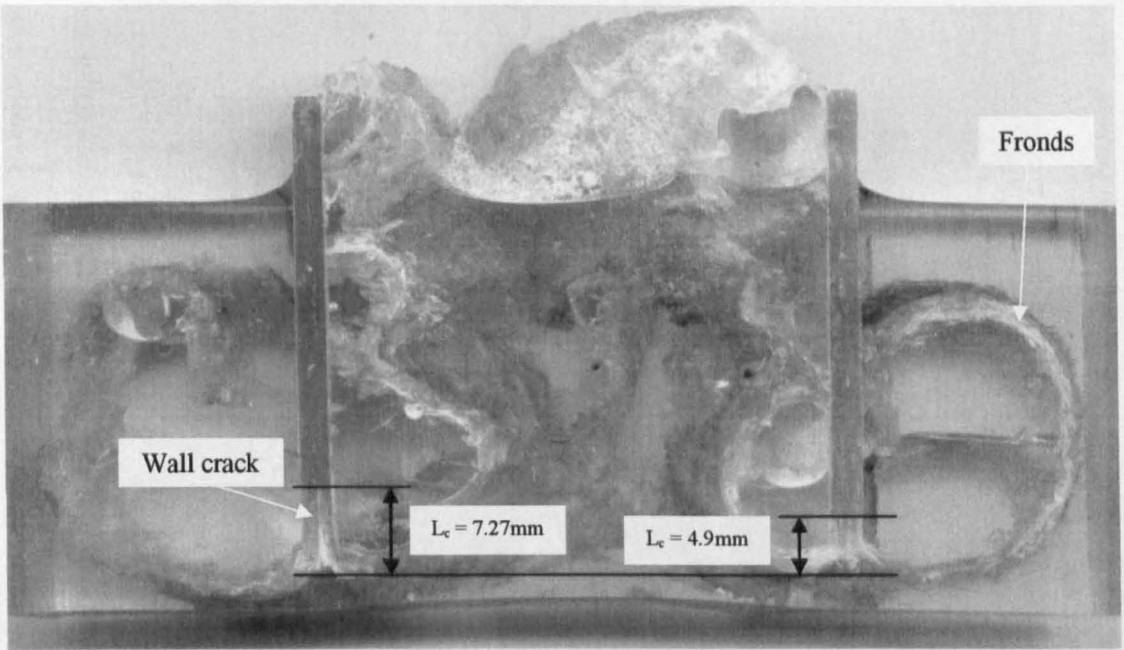
**Statically Tested (5mm/min)**
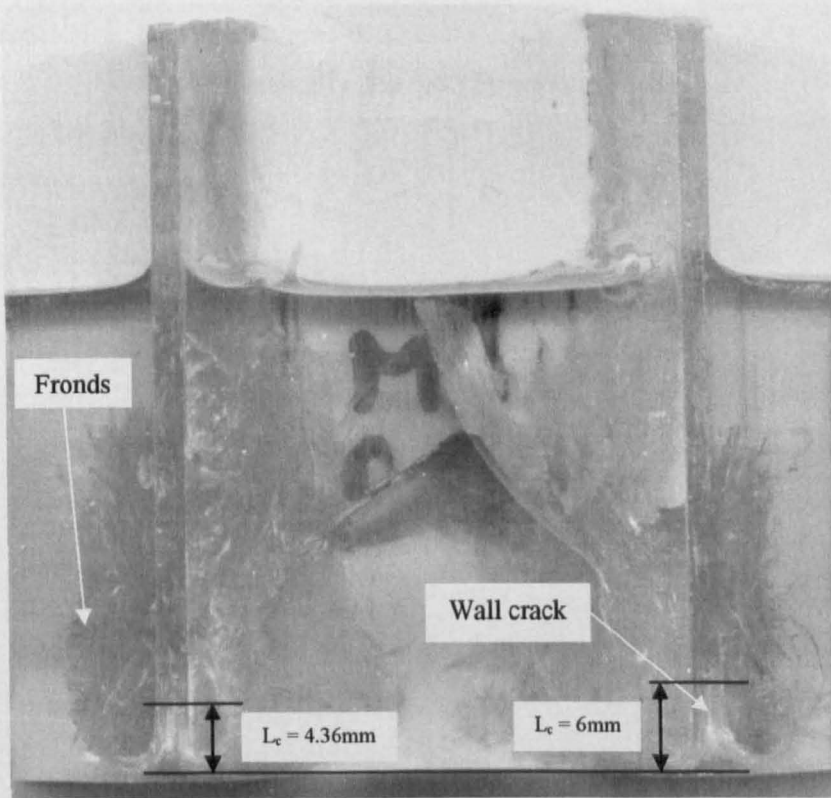


**Dynamically Tested (5m/s)**

**Figure 5-1 – Scans of potted statically and dynamically tested small CoFRM tubes**
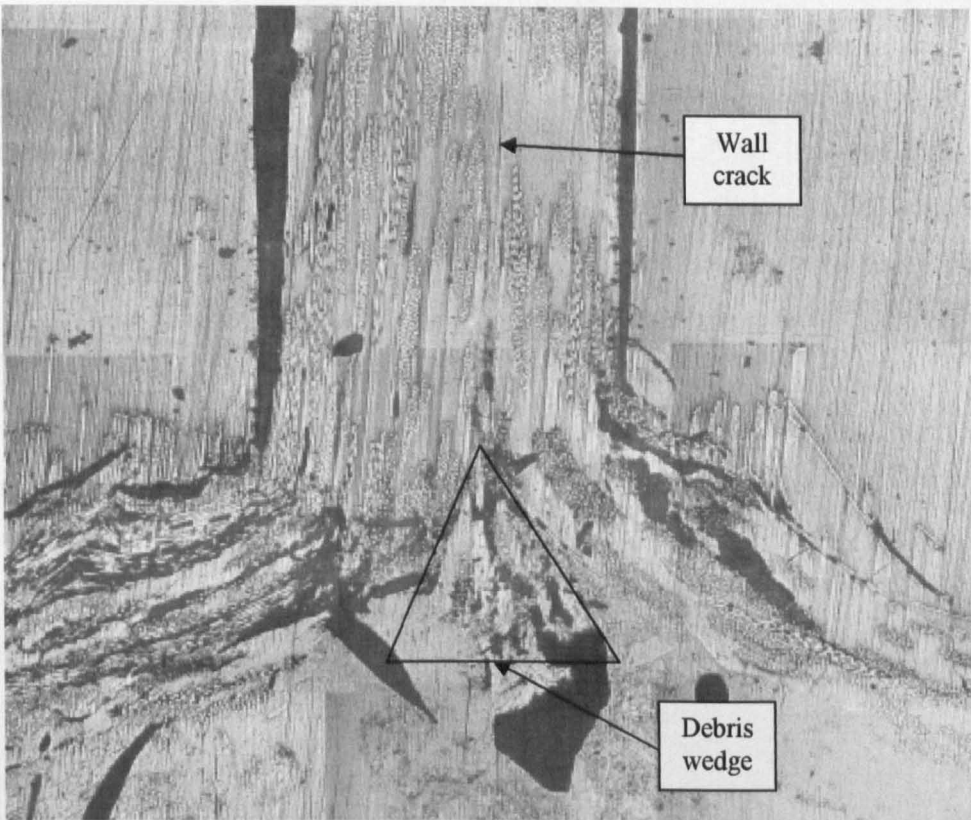
**Statically Tested (5mm/min)**
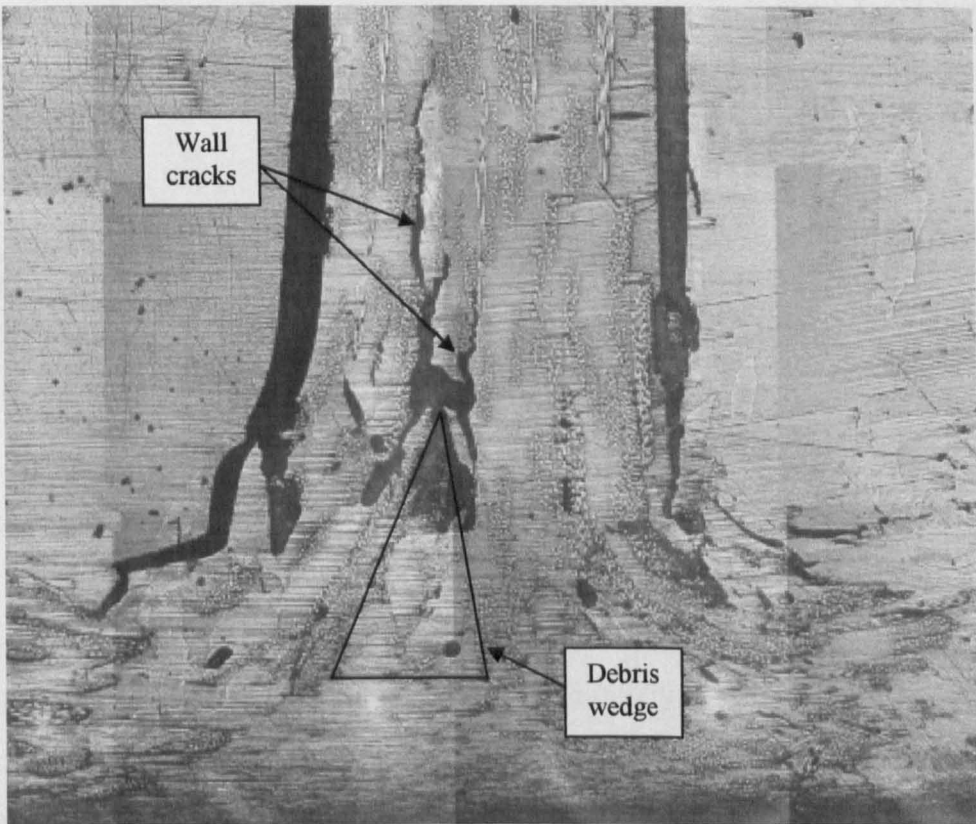
**Dynamically Tested (5m/s)**

**Figure 5-2 – Micrographs of potted statically and dynamically tested small CoFRM tubes**
**(22 times magnification)**

### 5.1.2 SEM Examination of Fronds

Images of the static and dynamic fronds from small CoFRM tubes were taken using an scanning electron microscope (see Section 3.5.3). The images taken at a magnification of 100 times (Figure 5-3) show large pieces of intact resin remaining in the statically tested sample. Large cracks can be seen where the resin has failed and disbonded fibre bundles. The dynamically tested sample shows a greater degree of matrix fragmentation and fibres have become unconstrained. The reduced stiffness of the fronds absorbs less energy than the statically tested samples where flexural failure dominated.



| Static | Dynamic |
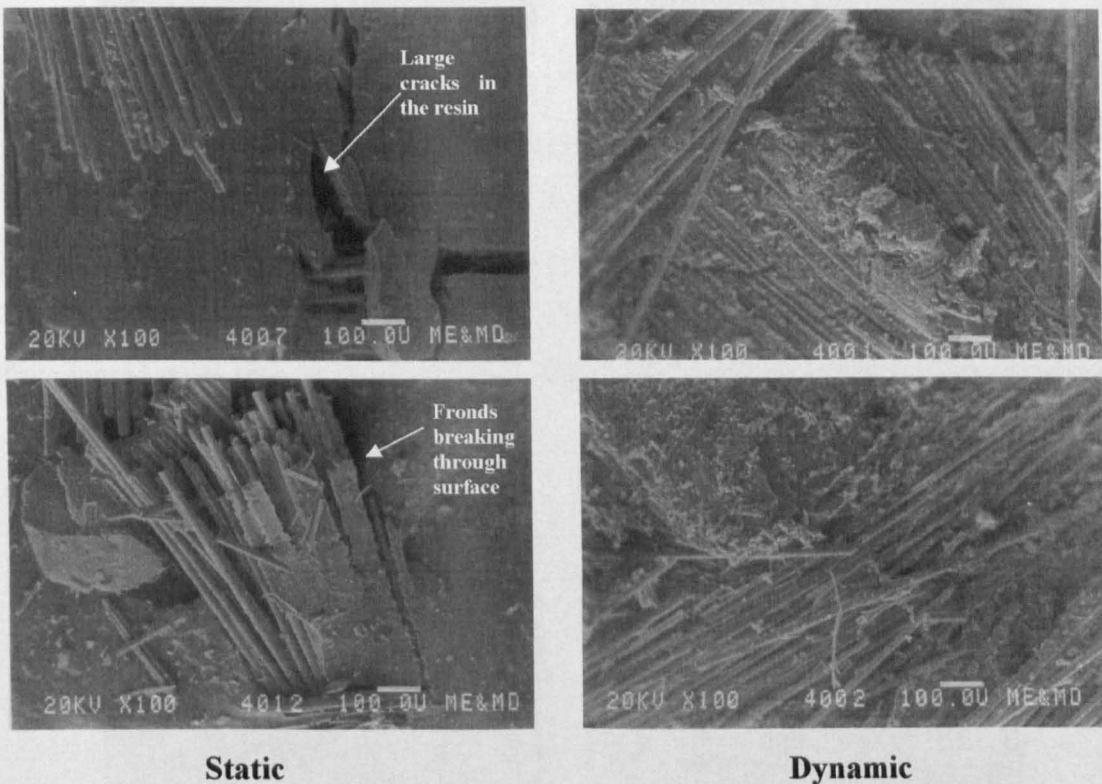
Figure 5-3 – SEM images of fronds from CoFRM small tube tests (100 times magnification)

The images of the fibres taken at a magnification of 500 times (Figure 5-4) confirm the above effects. In the static sample large matrix fragments remain, bonded to the individual fibres. The dynamic samples display wholesale fragmentation of the matrix.

Static               Dynamic
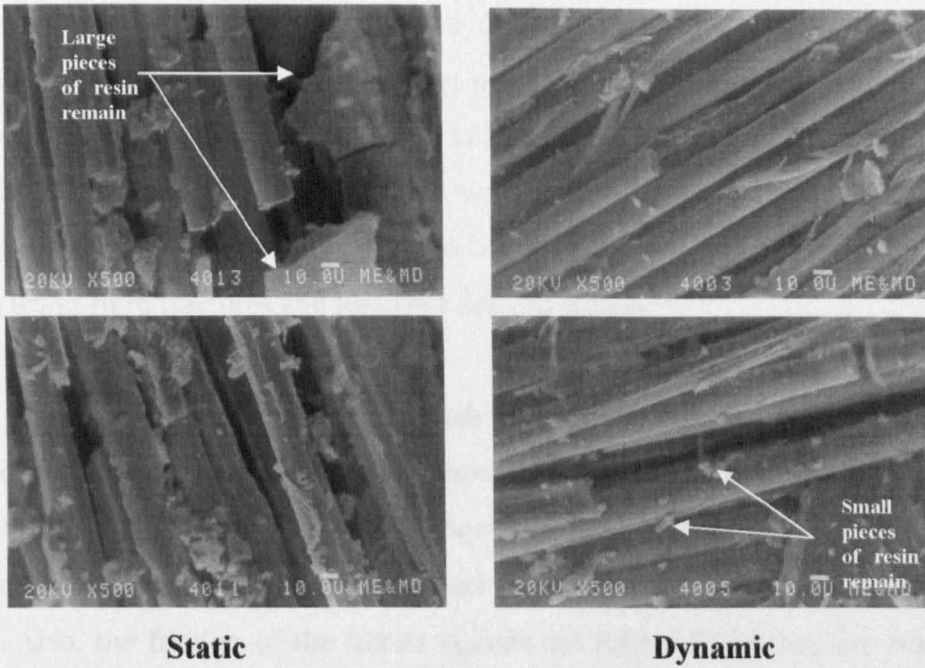
**Figure 5-4 – SEM images of fibres in fronds from CoFRM small tube tests**
**(500 times magnification)**

The final images are taken of the resin and again were at 500 times magnification
(Figure 5-5). Here it is clear to see that the resin in the dynamic sample has been
fragmented more than the static sample, which shows the resin still intact with cracks
starting to develop.
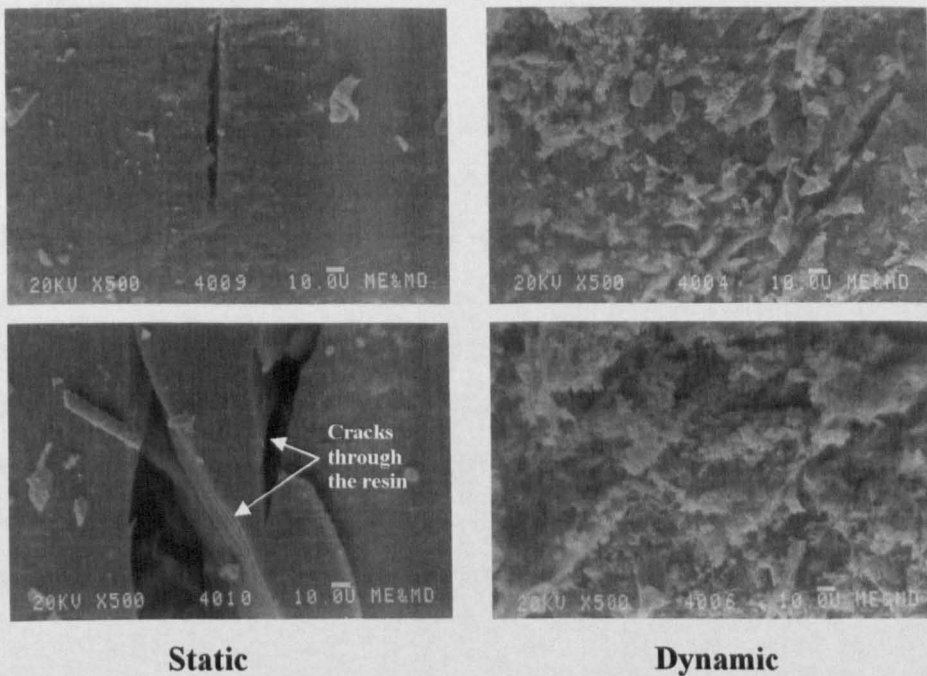


Static               Dynamic

**Figure 5-5 – SEM images of resin in the fronds from CoFRM small tube tests**
**(500 times magnification)**

The crush zones of the quasi-static and dynamically tested small CoFRM tubes suggest that the matrix has rate dependant properties, and has become more brittle at higher strain rates. Greater fragmentation at higher strain rates helps to account for the reduction in dynamic SEA and confirms work by Hamada and Ramakrishna [1][2]. This latter work attributed these effects to larger central wall cracks, a smaller debris wedge, fewer fibre fractures and less well defined fronds.

Hull [3] identified forces acting in the crush zone of a splaying tube and reductions of these could be seen in the dynamically tested tubes. The compressive forces acting at the platen on the fronds and debris wedge would be reduced due to the increased compliance of the fronds and a wider crack resulting in a lower force on the debris wedge. Also, the friction of the fronds against the tube wall as they are bent round would be reduced due to fragmentation of resin and less constrained fibres. Fairfull and Hull [4] determined that the forces of the fronds and debris wedge against the platen were nearly all taken up by the debris wedge, which contributed 67%. A slight reduction in any of these forces or frictional effects would account for the difference in SEA seen between the dynamic and quasi-static tests of the small CoFRM tubes. The frictional effects would be the same regardless of test speed and are directly proportional to the force. As the forces on the debris wedge and fronds reduce, the frictional effects would also be lower.

The change in resin behaviour may also explain the change in failure mode of the braided tubes from buckling to splaying as test rate increased. Statically, samples buckled due to compressive failures in the resin causing the tube walls to buckle. The splaying mode seen in the dynamic tests is due to an increase in compressive strength, which would allow the formation of a stable crush zone before the tube walls had buckled. Fernie [5] showed that the compressive strength of glass CoFRM/polyester increased by 108% at 5m/s and was attributed to the rate sensitivity of the resin. However, an increase of the compressive strength of the fibres at higher strain rates may also account for the change in failure mode reported.

## 5.2 Prediction of Failure Mode

In order to predict whether a tube containing damage will fail stably by progressive crush or unstably producing a crack from the damage point, the amount of damage must first be quantified. Stress concentration factors are a useful way of quantifying and comparing damage levels over samples of varying geometry.

In a structure or component containing a notch or abrupt change in cross-section (or damage in the present context), the maximum stress will often occur at this location. The ratio of this maximum stress ($\sigma_m$) to the nominal stress ($\sigma$) is the stress concentration factor $K_T$, shown in equation (5-1).

$$\frac{\sigma_m}{\sigma} = K_T$$

**(5-1)**

### 5.2.1 Tensile Coupons Containing Holes

Stress concentration factors for a hole in a finite plate are well documented and these values are based on the ratio of hole size to width of plate. For the specimens tested here which were 25mm wide and containing a 5mm or 10mm hole the $K_T$s were 2.512 and 2.216 respectively. The stress along the x-axis of the hole is given by:



**(5-2)**

Where:

$\sigma = applied\ stress\ (Pa)$

$r = radius\ of\ hole\ (mm)$

$x = position\ from\ centre\ of\ hole\ (mm)$

$K_T = Stress\ Concentration\ Factor$

When predicting the strength of a sample containing a stress concentration two methods are commonly used [6], the point stress criterion (PSC) and the average stress criterion (ASC). The PSC assumes that failure occurs when the stress at some distance, $d_c$, from the hole reaches the unnotched tensile failure stress of the material,

$\sigma_F$. The ASC assumes failure to occur when the average stress over a distance from the hole first reaches the failure stress of the material. In this study the PSC has been used to compare theoretical predictions of the failure stress of coupons containing holes to experimental results as initial calculations showed it to be more accurate than the ASC. Static experimental failure stresses for the coupon tests are shown in Table 5-1 below:

| Sample Type | Failure Stress (MPa) | Std.Dev. (%) |
|---|---|---|
| Unnotched | **161.09** | 9.45 |
| 5mm Hole In Centre | **121.31** | 7.51 |
| 10mm Hole in Centre | **84.67** | 12.13 |

Table 5-1 – **Experimentally obtained failure stresses for unnotched tensile samples and containing holes in the centre of the samples tested at 5mm/min**

Equation (5-2) was used to calculate the stress along the x-axis of the hole in the coupons containing a 5mm and 10mm hole to find the value $d_c$ at which the stress equalled the failure stress, $\sigma_F$. Stresses at which the samples failed were used in these calculations. Figure 5-6 shows the stress distribution from the edge of the hole, where maximum stress occurs, to the edge of the sample where the stress has dropped to the nominal stress.
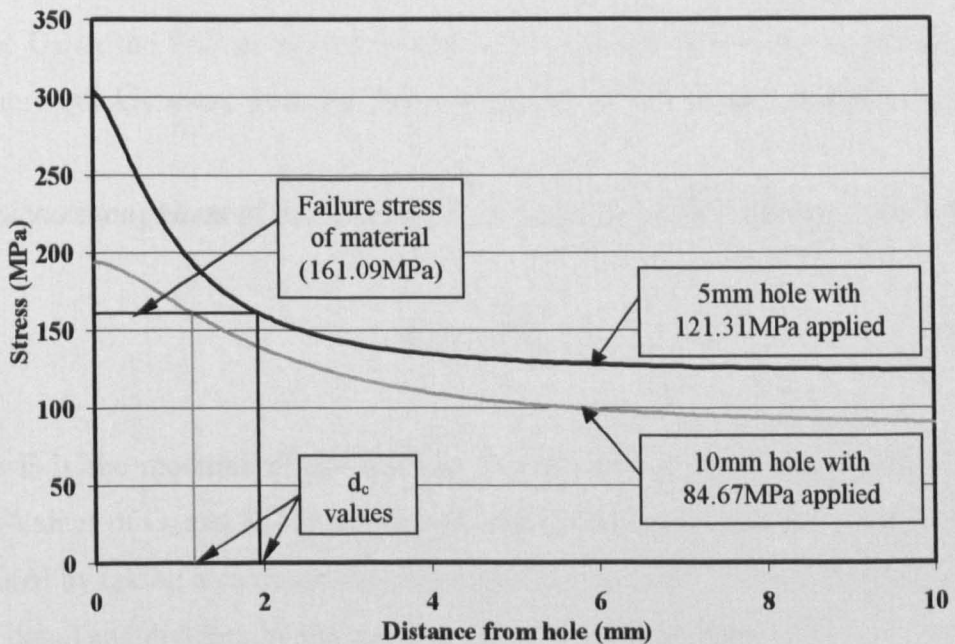


Figure 5-6 – **Stress vs. distance from edge of hole for a CoFRM/polyester coupons containing holes, under tension**

From these calculations, the value $d_c$ was found to be 1.95mm, at which the stress equalled $\sigma_F$ for the material. Substituting this value, $d_c$, back into equation (5-2) using the $K_T$ and hole radius of the 10mm holed sample gave a theoretical critical stress of 92.82MPa at which the sample would fail. The experimental value of this critical stress was found to be 84.67MPa with a standard deviation of 12.13%.

Starting with the experimentally tested 10mm holed sample, a value of 1.47mm was found for $d_c$ using equation (5-2). This led to a theoretical critical stress for the 5mm holed sample of 109.74MPa. The experimental value of this critical stress was found to be 121.31MPa with a standard deviation of 7.51%.

Although the theoretical values for the failure stresses did not match the experimental values exactly the calculation for the 10mm holed sample did fall into the range of results covered by the standard deviation and was close to the experimental range for the 5mm holed sample.

The maximum stress in the sample at failure was calculated for the experimental results by multiplying the failure stress by the $K_T$ value for the sample. The sample containing a 5mm hole failed with a maximum stress of 304.73MPa and the 10mm holed sample 184.63MPa. The higher maximum stress in the 5mm holed sample is due to a larger concentration of the uniform stress near the boundary of the hole due to the smaller radius. However, since a smaller volume of material is subjected to a higher stress the overall strength of the material is higher than in the 10mm holed sample. Using the PSC as described above accounts for this as the maximum stress falls more quickly away from the 5mm hole than the 10mm hole as shown in Figure 5-6.

*The fracture toughness* of the material, $K_c$ is calculated using equation (5-3) below:

$$K_c = \sqrt{EG_c}$$

(5-3)

Where E is the modulus of the material in GPa and $G_c$ the energy release rate in kJ/m$^2$. Values of $G_c$ and $K_c$ for the samples tested here are shown in Table 5-2. $G_c$ was calculated by taking area under the load displacement curve of the unnotched samples (work done) and dividing by the cross-sectional area of the sample [7].

| Test Rate | | |
|-----------|--------|-------|
| 5mm/min | 330.24 | 61.45 |
| 5m/s | 718.49 | 90.64 |

**Table 5-2 – Fracture toughness calculated from tensile tests of unnotched samples conducted at 5mm/min and 5m/s**

As shown, the critical strain energy release rate and hence fracture toughness have increased with increased test rate by 118% and 47% respectively. Geary [8] also showed that fracture toughness increased up to a factor of 3 at increased test rate for GRP samples. This effect may explain why the dynamic tube samples have been more tolerant to damage. As the fracture toughness increases at increased load rate, the stresses required to form a crack in the sample will increase. This leads to the dynamic samples withstanding larger amounts of applied damage before unstable failures occur.

### 5.2.2 Tubular Samples Containing Holes

Savin [9] and Roark [10] have both developed equations for calculating values of $K_T$ for a hole in an isotropic cylinder and are shown below in equations (5-4) to (5-7). Figure 5-7 below shows the cylinder geometry and relevant notation for these equations.
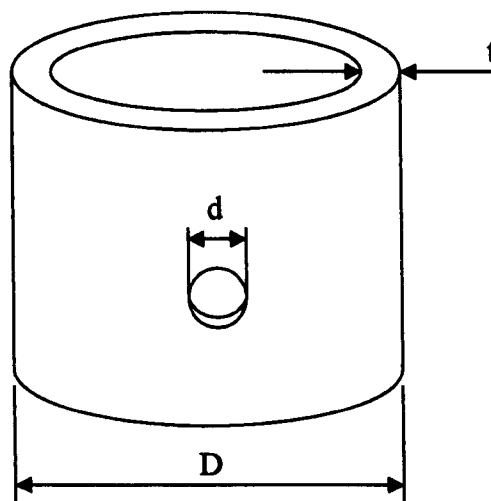


**Figure 5-7 – Geometry of cylinders and notation for $K_T$ formulae**

*Savin's Equation:*

$$K_T = 3 + \sqrt{\frac{3(m^2 - 1)}{m^2}} \frac{\pi}{8} \frac{d^2}{Dt}$$

(5-4)

Where:
$$m = \frac{1}{v}$$

The above expression becomes invalid when:

$$\frac{d}{D} \geq \sqrt{(2t/D)}$$

(5-5)

Expression 5.5 above implies that the if the wall thickness is low compared to the tube diameter or for large hole to tube diameter ratios (i.e. large holes) Savin's expression for $K_T$ is invalid. This could be due to greater wall bending in these situations and suggests that equation 5.4 holds only for membrane stresses.

Table 5-3 lists d/D ratios for the tubes tested in this study to check the validity of the $K_T$ calculation. Values $\geq \sqrt{(2t/D)}$ are used to discuss the results but regarded with caution as Savin believed his expression became invalid outside this limit.

| Tube Geometry | 89.1mm diameter, 4mm wall | 89.1mm diameter, 3.33mm wall | 89.1mm diameter, 2.67mm wall | 38.1mm diameter, 2mm wall |
|---|---|---|---|---|
| $\sqrt{2t/D}$ | 0.300 | 0.274 | 0.245 | 0.324 |
| d/D (5mm hole) | 0.056 | 0.056 | 0.056 | 0.131 |
| d/D (7.5mm hole) | 0.084 | 0.084 | 0.084 | 0.197 |
| d/D (10mm hole) | 0.112 | 0.112 | 0.112 | 0.262 |
| d/D (12.5mm hole) | 0.140 | 0.140 | 0.140 | 0.328 |
| d/D (16mm hole) | 0.180 | 0.180 | 0.180 | 0.420 |
| d/D (20.25mm hole) | 0.227 | 0.227 | 0.227 | - |

**Table 5-3 – Validity of Savin $K_T$ for all tube geometries**

*Roark's Equation:*

$$K_T = C_1 + C_2\left(\frac{d}{D + 2t}\right) + C_3\left(\frac{d}{D + 2t}\right)^2 + C_4\left(\frac{d}{D + 2t}\right)^3$$

(5-6)

Where:    $C_1 = 3$

$$C_2 = 2.773 + 1.529\left(\frac{D}{D+2t}\right) - 4.379\left(\frac{D}{D+2t}\right)^2$$

$$C_3 = -0.421 - 12.782\left(\frac{D}{D+2t}\right) + 22.781\left(\frac{D}{D+2t}\right)^2$$

$$C_4 = 16.841 + 16.67\left(\frac{D}{D+2t}\right) - 40.007\left(\frac{D}{D+2t}\right)^2$$

Valid for:    $\dfrac{D}{D+2t} \le 0.9$    and    $\dfrac{d}{D+2t} \le 0.45$

(5-7)

Roark's lost validity outside the limits presented in equation (5-7). Table 5-4 shows the values for these conditions calculated for the tubes tested in this study. As before the values outside the limits of (5-7) are invalid and this includes all of the tubes tested here. This suggests that equation (5-6) holds only for thick cylinders and will not be used to discuss the results further.

| Tube Geometry | 89.1mm diameter, 4mm wall | 89.1mm diameter, 3.33mm wall | 89.1mm diameter, 2.67mm wall | 38.1mm diameter, 2mm wall |
|---|---|---|---|---|
| D/(D+2t) | 0.918 | 0.930 | 0.943 | 0.905 |
| d/(D+2t) 5mm | 0.051 | 0.052 | 0.053 | 0.119 |
| d/(D+2t) 7.5mm | 0.077 | 0.078 | 0.079 | 0.178 |
| d/(D+2t) 10mm | 0.103 | 0.104 | 0.106 | 0.238 |
| d/(D+2t) 12.5mm | 0.129 | 0.131 | 0.132 | 0.297 |
| d/(D+2t) 16mm | 0.165 | 0.167 | 0.169 | 0.380 |
| d/(D+2t) 20.25mm | 0.209 | - | - | - |

Table 5-4 - Validity of Roark $K_T$ for all tube geometries

Using equation (5-4), $K_T$ values for the CoFRM tubes tested in this study were calculated and are shown in Table 5-5.

| Tube Geometry: | 89.1mm diameter, 4mm wall | 89.1mm diameter, 3.33mm wall | 89.1mm diameter, 2.67mm wall | 38.1mm diameter, 2mm wall |
|---|---|---|---|---|
| Hole Size | $K_T$ Equation 5.4 | $K_T$ Equation 5.4 | $K_T$ Equation 5.4 | $K_T$ Equation 5.4 |
| 5mm | 3.05 (Ts) | 3.05 (Ts) | 3.07 (Ts) | 3.21 (Td) |
| 7.5mm | 3.10 | 3.12 | 3.15 | 3.48 |
| 10mm | 3.18 | 3.22 | 3.27 | 3.85 |
| 12.5mm | 3.28 | 3.34 | 3.43 | 4.33 |
| 16mm | 3.47 | 3.56 | 3.70 | 5.18 |
| 20.25mm | 3.75 | - | - | - |

Ts - Static Threshold Values   Td - Dynamic Threshold Values (small CoFRM)

**Table 5-5 – $K_T$ values calculated for all tubes containing drilled holes from equation 5.4**

Table 5-5 shows that the 5mm hole in the small tubes produced $K_T$ values equivalent to holes between 10mm and 12.5m. This explains why the small tubes containing a 5mm hole produced unstable failures whilst the large tubes were unaffected.

Static threshold values of $K_T$ that allowed tubes to crush stably are identified. Thus, tubes crushed at 5mm/min produced stable failures if:

$$K_T \leq 3.07 \text{ (equation 5.4)}$$

(5-8)

Dynamic threshold values of $K_T$ for the small CoFRM tubes tested dynamically at 5m/s were identified. Therefore, for tubes tested at 5m/s, stable failure occurred if:

$$K_T \leq 3.21 \text{ (equation 5.4)}$$

(5-9)

From the tensile tests it was shown that the maximum stress in the samples containing a 5mm or 10mm hole were not the same when failure occurred. Using the values of $K_T$ from Table 5-5 the maximum stress in each tube when an unstable failure occurred could be calculated. The applied stress was calculated by dividing the load applied by the cross-sectional area of the tube. The load at failure was taken from the raw data obtained during testing and the respective stress multiplied by the $K_T$ value to give maximum stress in the sample. For samples that failed stably, the maximum load applied to the sample before the hole was reached by the crush zone were obtained.

Table 5-6 (a) shows the maximum stresses in the small CoFRM tubes tested statically at 5mm/min.

| Hole Size and Position (mm) | Sample 1 | | | Sample 2 | | | Sample 3 | | |
|---|---|---|---|---|---|---|---|---|---|
| | $\sigma_m$ | | Disp.(mm) | $\sigma_m$ | | Disp.(mm) | $\sigma_m$ | | Disp.(mm) |
| 16 @ 30mm | 321.32 | (U1) | 1.48 | 296.22 | (U1) | 1.81 | 317.86 | (U1) | 1.48 |
| 12.5 @ 30mm | 270.80 | (U1) | 2.64 | 307.89 | (U1) | 1.98 | 311.50 | (U1) | 3.30 |
| 10 @ 15mm | 309.39 | (U2) | 3.21 | 334.81 | (U2) | 4.20 | 358.14 | (U2) | 3.13 |
| 10 @ 30mm | 323.55 | (U2) | 2.88 | 372.46 | (U2) | 3.79 | 374.39 | (U2) | 5.85 |
| 10 @ 45mm | 398.68 | (U2) | 3.95 | 392.89 | (U2) | 8.48 | 403.51 | (U2) | 4.53 |
| 7.5 @ 30mm | 332.07 | (U2) | 10.88 | 318.70 | (U2) | 18.29 | 374.22 | (U2) | 14.00 |
| 5 @ 30mm | 317.81 | (U2) | 5.39 | 335.66 | | stable | 349.08 | | stable |

(a) Small CoFRM tubes tested at 5mm/min

| Hole Size and Position (mm) | Sample 1 | | | Sample 2 | | | Sample 3 | | |
|---|---|---|---|---|---|---|---|---|---|
| | $\sigma_m$ | | Disp.(mm) | $\sigma_m$ | | Disp.(mm) | $\sigma_m$ | | Disp.(mm) |
| 16 @ 30mm | 400.51 | (U1) | 1.75 | 346.42 | (U1) | 1.75 | 339.28 | (U1) | 1.75 |
| 12.5 @ 30mm | 299.38 | (U1) | 2.61 | 338.64 | (U1) | 1.99 | 325.61 | (U2) | 4.41 |
| 10 @ 15mm | 334.33 | (U2) | 7.39 | 325.96 | | stable | 370.20 | (U2) | 5.31 |
| 10 @ 30mm | 336.90 | (U2) | 19.47 | 357.49 | | stable | 315.66 | (U2) | 18.95 |
| 10 @ 45mm | 341.73 | | stable | 359.43 | | stable | 346.88 | | stable |
| 7.5 @ 30mm | 293.71 | | stable | 312.60 | | stable | 294.00 | (U2) | 19.44 |
| 5 @ 30mm | 292.58 | | stable | 288.42 | | stable | 307.75 | | stable |

(b) Small CoFRM tubes tested at 5m/sec

U1 – unstable failure before crush zone formation
U2 – unstable failure after crush zone formation

**Table 5-6 – Maximum Stresses (MPa) in the small (38.1mm diameter, 2mm wall) CoFRM tubes containing holes, tested at 5mm/min and 5m/s**

U1 indicates samples where unstable failure occurred before the stable crush zone had been achieved, whilst the initial load was still rising. These would be similar to testing an unchamfered tube as the debris wedge and hence, interlaminar wall crack had not formed. It is believed that samples containing a 16mm or 12.5mm hole would fail unstably regardless of where the hole was situated. U2 indicates samples that failed after the formation of the crush zone. Once a debris wedge had formed, the tube wall is split and the fronds curve inwards and outwards.

The failure stresses in the samples containing a 10mm hole increase as the distance of the hole from the chamfer increases. Failures occurred while the crush zone was forming and have caused the samples with a hole closer to the chamfer to fail at lower applied stresses. A 10mm hole, or SCF of 3.85, seems to be the threshold level of damage where failure occurs during the formation of the crush zone. A slightly lower SCF would allow a region of stable crush before the crush zone reaches the damage

area and a slightly higher SCF would produce a failure before the crush zone had started to form.

When a 7.5mm hole, or SCF of 3.48 was added, failures occurred at much higher displacements than had been seen for the larger holes (between 10.88 and 18.29mm). This implies that failures had been caused by increased stresses added from the effect of the crush zone.

From the results seen here it can be said that if a tube sample contains a hole it will produce an unstable failure regardless of hole position if:

$$K_T \geq 4.33 \text{ (equation 5.4)}$$

**(5-10)**

Appendix 7.7 shows the maximum stresses at failure for the large CoFRM tubes. None of the samples failed before the crush zone had formed and this follows the condition set in equation (5-10), as the maximum $K_T$ value was 3.75 for the large CoFRM/Crystic tubes containing a 20.25mm hole.

Table 5-6 (b) shows the maximum stresses in the small CoFRM tubes tested dynamically at 5m/s. Failures that occurred without the formation of the crush zone are shown in red. A threshold hole size of 12.5mm was found where failures occurred during the formation of the crush zone. For hole sizes of 10mm or lower samples only failed when the damage zone reached the crush zone or failed stably. From the dynamic tests it can be said that a small CoFRM tube will fail unstably, regardless of hole position if:

$$K_T \geq 5.18 \text{ (equation 5.4)}$$

**(5-11)**

The maximum stresses before the crush zone reached the damage area are shown for samples that failed stably in bold in Table 5-6. No trends were found in these values and for samples that had both stable and unstable failures the maximum stresses were often higher in the samples failing stably than the failure stresses in those failing unstably. This indicates that, for hole sizes between those which produce stable failures and unstable failures regardless of hole position, the failure prediction becomes difficult.

### 5.2.3 Tubular Samples Containing Impacts

Taking the equivalent hole diameters from Section 4.7.4 and applying equation (5-4), the $K_T$ values for the impacted CoFRM tubes were calculated (Table 5-7).

| Tube Geometry | 89.1mm diameter, 4mm wall | 89.1mm diameter, 3.33mm wall | 89.1mm diameter, 2.67mm wall | 38.1mm diameter, 2mm wall |
|---|---|---|---|---|
| Impact | $K_T$ (equation 5.4) | $K_T$ (equation 5.4) | $K_T$ (equation 5.4) | $K_T$ (equation 5.4) |
| 1.5J | 3.01 (Ts) | 3.03 (Ts) | 3.06 (Ts) | 3.59 (Td) |
| 3J | 3.10 (Ts) | 3.14 | 3.21 | 4.08 |
| 6J | 3.22 | 3.30 | 3.44 | 4.98 |
| 9J | 3.32 | 3.47 | 3.65 | 5.13 |

Ts - Static Threshold Values    Td - Dynamic Threshold Values (Small CoFRM)

**Table 5-7 - $K_T$ values calculated for all tubes containing impact damage from equation 5.4**

The static threshold values, shown in red, indicate that for a pre-impacted sample to fail stably the $K_T$ value must be equal to or less than 3.1. This is slightly higher than the value found for samples containing holes, (3.07), but show that a good estimation of damage amount can be obtained by using the width of the damage area to approximate the equivalent hole diameter. The dynamic threshold values were also overestimated but by a larger amount. It is believed that this method of quantifying the impact damage amount as a hole of diameter equal to the width of the damage area is more accurate for smaller impacts and the estimation loses accuracy as impacts increase. Further investigation would be required to confirm these results.

For the samples containing simulated delamination it was found that delamination was not a principle cause of failure. Even when a 50.8mm diameter delamination was introduced into a 38.1mm tube, SEA reduction was still very small and could not be approximated by an equivalent hole.

For the small CoFRM tubes tested in this study, damage tolerance has shown to increase as test rate increased. The main factor in this increase is believed to be an increased compressive strength attributed to rate dependant properties of the resin used in manufacture. Combined with a lower crush load, this increased strength means that samples can withstand larger amounts of damage before unstable failures occur and significant reduction in SEA is seen. From the tensile coupon tests conducted it was also shown that the fracture toughness of the CoFRM/polyester

material used in the majority of the tube tests increased with increased test rate and would also imply that larger amounts of damage would be required for cracks, and hence, unstable failures to occur.

## 5.3 Chapter 5 References

[1] Ramakrishna S, Energy Absorption Characteristics of Knitted Fabric Reinforced Epoxy Composite Tubes, Journal of Reinforced Plastics and Composites, Vol. 14, pp1121-1141, 1995.

[2] Hamada H and Ramakrishna S, Comparison of Static and Impact Energy Absorption of Carbon Fiber/PEEK Composite Tubes, Composite Materials: Testing and Design, Vol.12, ASTM STP 1274, R.B.Deo and C.R.Saff, Eds., American Society for Testing and Materials, pp182-197, 1996.

[3] Hull D, A Unified Approach to Progressive Crushing of Fibre-Reinforced Composite Tubes, Composites Science and Technology, Vol.40, pp377-421, 1991.

[4] Fairfull AH and Hull D, Energy Absorption of Polymer Matrix Composite Structures: Frictional Effects, Symposium on Structural Failure, Chapter 8, pp255-279, June 1988.

[5] Fernie R, PhD Thesis, Loading Rate Effects on the Energy Absorption of Tubular Crash Structures, University of Nottingham, 2002.

[6] Bull JW, Numerical Analysis and Modelling of Composite Materials, Blackie Academic and Professional, 1996.

[7] Hull D and Clyne TW, An Introduction to Composite Materials, Second Edition, Cambridge University Press, Cambridge, p211, 1996.

[8] Geary W, Dutton J and Shuter DM, The influence of size effects and dynamic loading on the fracture toughness of commercial GRP materials, Composites Science and Technology, Vol.60, pp633-638, 2000.

[9] Savin GN, Stress concentration around holes, Pergamon Press, Oxford 1961.

[10] Young WC, Roark's Formulas for Stress and Strain, 7th Edition, McGraw-Hill Professional, 2001.

# 6.0 Conclusions

The aim of this work was to consider the effect of pre-existing damage on the energy absorption potential of composite tubes under axial loading. Simulated damage was added by drilled holes, PET inserts to mimic delamination and impact damage applied using a dropped mass. Specimen geometries, strain rates and material type have been varied to investigate their respective effects on overall energy absorption and damage tolerance.

Based on the quasi-static tests it has been shown that circular section CoFRM/polyester tubes with t/D ratios of between 0.03 and 0.0525 can provide reproducible energy absorption levels within ±15%. A linear increase in SEA was noted as the t/D ratio increased. This effect could be attributed to a more stable crush zone in the thicker walled tubes, allowing a larger debris wedge and thicker fronds to form.

Tests on undamaged small CoFRM tubes revealed a reduction in SEA of around 9% when increasing crush rate from 5mm/min to 5m/s. The mode of failure was unchanged, but due to the rate dependency of the resin, greater fragmentation in the dynamic samples caused the fibres to become unconstrained, bend more easily and with fewer fibre fractures. The scope of this test matrix was rather limited and more work is needed to understand this effect fully.

Equivalent tests on braided tubes showed that ±45° braids produced increased SEA when crushed at higher load rates. This was due to a change in failure mode when the load rate increased from a buckling mode quasi-statically to a splaying mode dynamically. The buckling was attributed to the absence of axial fibres and therefore reduced axial strength. This caused the walls of the tube to collapse inwards and reduced the energy absorbed due to the lack of central wall crack. The dynamic tests produced a splaying failure as the speed of the test caused an apparent increase in compressive strength allowing formation of a stable crush zone before buckling of the walls occurred.

The coupon tests showed that the tensile failure stress of a CoFRM/polyester composite increased significantly with increasing test speed (by125% over the range of rates tested here). As stress concentrators were added this effect was reduced and for a sample containing a 10mm hole the failure load was comparable for the statically and dynamically tested specimens. This was attributed to the smaller area available for absorbing damage with the stress concentrators added, which negates the rate effect.

Damage thresholds in the case of drilled holes and preliminary impacts have been found for each tube type. *The values in brackets indicate the t/D ratio of the tube:*

- **Large CoFRM/Crystic Tubes (0.0449)**          **5mm hole**
- **Large CoFRM/Norpol 4mm Walled Tubes (0.0449)**    **5mm hole / 3J impact**
- **Large CoFRM/Norpol 3.33mm Walled Tubes (0.0374)**   **5mm hole / 1.5J impact**
- **Large CoFRM/Norpol 2.67mm Walled Tubes (0.0300)**   **5mm hole / 1.5J impact**
- **Small CoFRM/Norpol Tubes (0.0525) Static – 5mm/min**    **None found**
- **Small CoFRM/Norpol Tubes (0.0525) Dynamic – 5m/s**     **5mm hole / 1.5J impact**
- **Small Braided/Norpol Tubes (0.0525) Static – 5mm/min**   **None found**
- **Small Braided/Norpol Tubes (0.0525) Dynamic – 5m/s**    **10mm hole / 3J impact**

No damage thresholds were found for the small tubes tested statically or the CoFRM tubes containing delamination as none of the tests undertaken produced an unstable failure. Smaller amounts of damage would need to be applied in order to find these thresholds.

Stress concentration factors were calculated for holes in a cylinder, with a view to determining critical values for CoFRM/polyester circular tubes:

*At 5mm/min:*

For stable failure:

$$K_T \leq 3.07 \text{ (equation 5.4)}$$

For unstable failure, regardless of hole position:

$$K_T \geq 4.33 \text{ (equation 5.4)}$$

*and at 5m/s:*

For stable failure:

$$K_T \leq 3.21 \text{ (equation 5.4)}$$

For unstable failure, regardless of hole position:

$$K_T \geq 5.18 \text{ (equation 5.4)}$$

For $K_T$ values below these thresholds for stable crush, behaviour was unaffected and tubes crushed progressively. When the thresholds are exceeded the tubes may still crush progressively but there is a significant chance of unstable failures with consequent reduction in energy absorption. Samples containing damage that failed progressively often had a local drop in load as the crush zone passed through the damage area caused by the loss or damage of material in that area, hence reducing the load required to crush the samples at that point.

It has been shown that damage tolerance increases with an increase in test speed and more damage could be introduced without a change in failure mode. This was attributed to an increase in compressive strength and fracture toughness, and reduction in crush load as test speed increased.

Impact damage was quantified by estimating the equivalent hole diameter as the width of damage zone produced by the impact. This was found to be a reasonable, but slight over estimation of the damage level and the threshold values were higher than those found for the samples containing holes.

The tubes with a thicker wall were more tolerant to applied impact damage. Visible damage areas were shown to be smaller and larger amounts of impact damage were required to produce unstable failures.

Relatively small holes (5mm) and impacts (1.5J) can significantly reduce the SEA of CoFRM or braided/polyester composite tubes. Tests were conducted on relatively small samples and to incorporate the results into the design of an automotive structure would require further testing on larger specimens. The damage tolerance has shown to increase with strain rate but higher speeds would need to be investigated to see if this trend continued in high velocity impact situations.

# 7.0 Appendices

## 7.1 Specific Energy Absorption Calculation

Mass per unit lengths were taken from the weight of unchamfered tubes divided by their length and an average value was used for all tubes.

Specific Energy Absorption for undamaged small CoFRM/Norpol tube - sample 1:
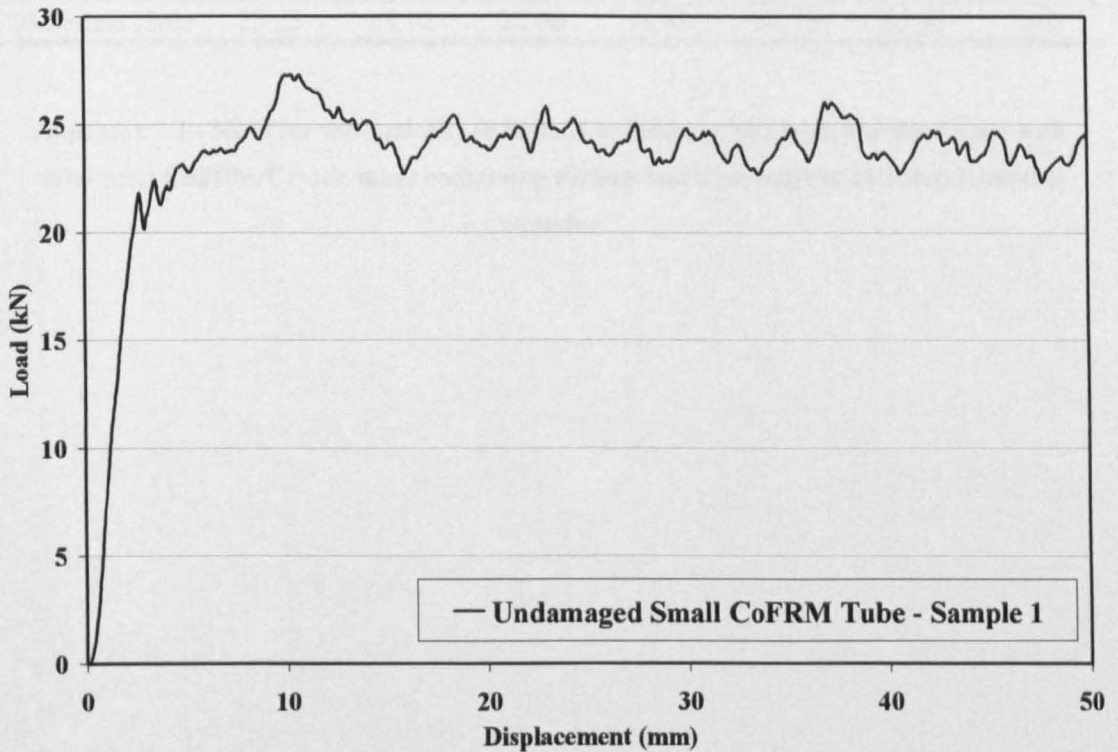


Area under curve, from 5mm displacement (using trapezium rule)    = 1098.598 Nm

= 1.098598 kJ

Mass of tube crushed    = Mass/unit length of tube × length of tube crushed

= 0.3375g/mm ×45.07mm

= 15.21g

= 0.01521kg

Specific Energy Absorption (SEA) = Area under curve/mass of tube crushed

= 1.098598/0.01521

= 72.23 kJ/kg

## 7.2 Large CoFRM/Crystic Tube Tests

| Damage Type | Specific Energy Absorption (kJ/kg) | | | | | | Std. Dev. |
| --- | --- | --- | --- | --- | --- | --- | --- |
| | Sample 1 | Sample 2 | Sample 3 | Sample 4 | Sample 5 | Average | (%) |
| Undamaged | 72.24 | 66.47 | 64.88 | 62.49 | 67.10 | **66.64** | 5.40 |
| 5mm Hole | 70.93 | 69.61 | 69.66 | 67.27 | 74.52 | **70.40** | 3.77 |
| 10mm Hole | 64.79 | 62.48 | 64.47 | 57.98 | 32.52 | **56.45** | 24.18 |
| 12.5mm Hole | 37.24 | 51.17 | 52.07 | 26.86 | 54.07 | **44.28** | 26.65 |
| 16mm Hole | 55.02 | 27.21 | 18.58 | 31.14 | 56.80 | **37.75** | 45.57 |
| 20.25mm Hole | 25.23 | 23.92 | 22.00 | 19.49 | 23.73 | **22.87** | 9.68 |

Appendix 7-1– SEAs for the statically (0.5mm/s) tested large (89.1mm diameter/4mm wall thickness) CoFRM/Crystic tubes containing various hole sizes centred at 30mm from the chamfer
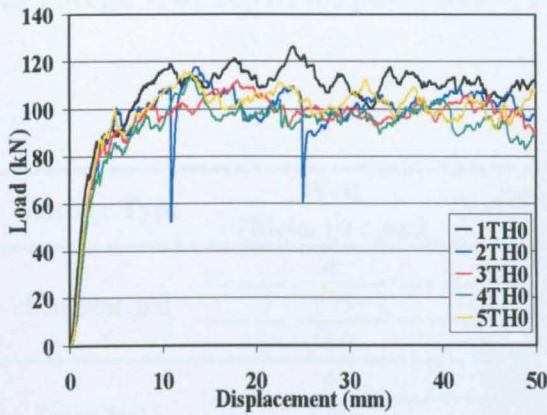
Undamaged Tubes
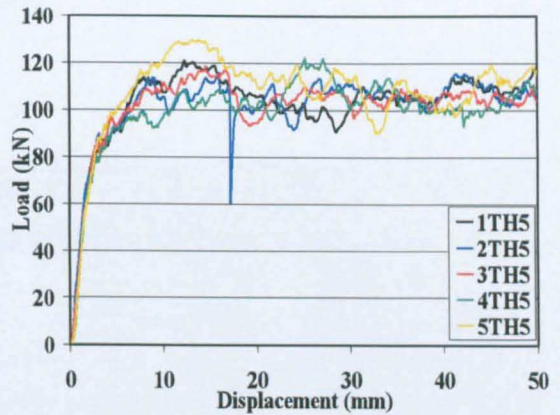
Tubes Containing a 5mm Hole
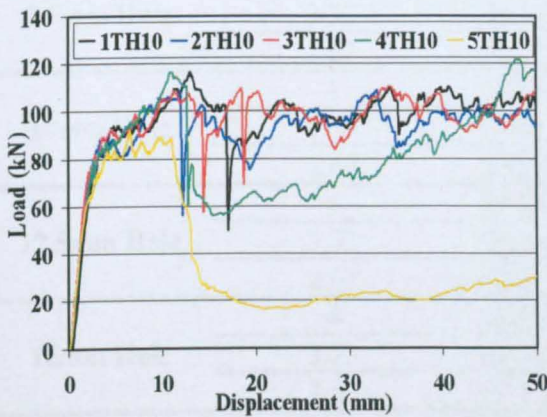
Tubes Containing a 10mm Hole
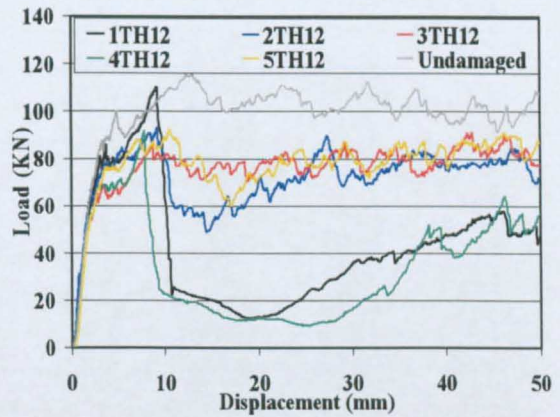
Tubes Containing a 12.5mm Hole
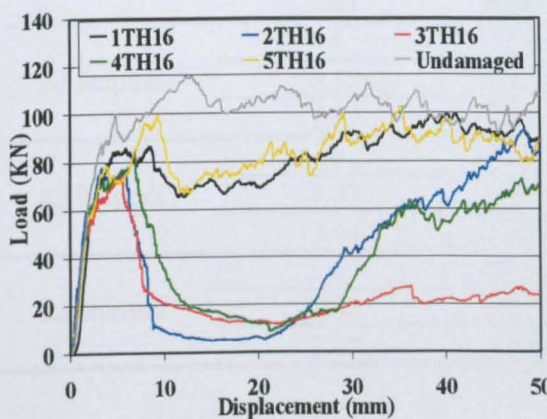
Tubes Containing a 16mm Hole
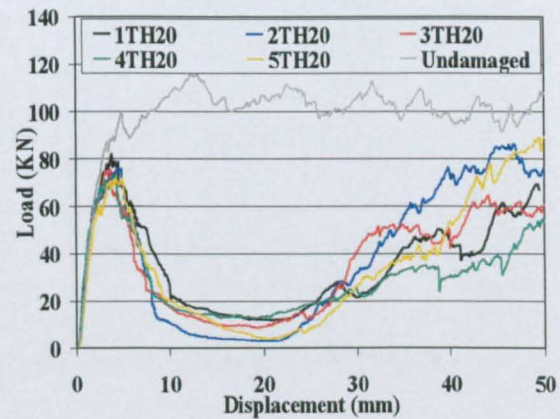
Tubes Containing a 20.25mm Hole

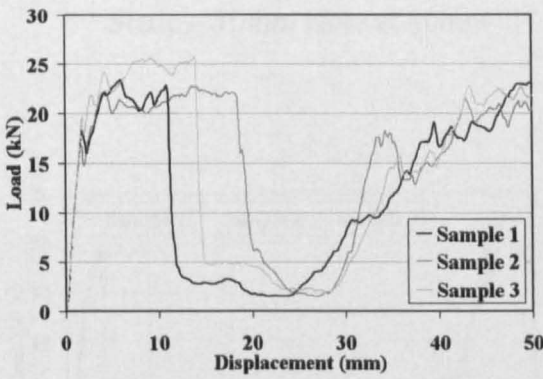**Appendix 7-2 – Load-displacement curves for the statically (0.5mm/s) tested large (89.1mm diameter/4mm wall thickness) CoFRM/Crystic tubes containing various hole sizes centred at 30mm from the chamfer**

## 7.3 Large CoFRM/Norpol Tube Tests

| Damage Type | Wall Thickness (mm) | Specific Energy Absorption (kJ/kg) | | | | Std. Dev. (%) |
|---|---|---|---|---|---|---|
| | | Sample 1 | Sample 2 | Sample 3 | Average | |
| Undamaged | 4 | 68.47 | 70.63 | 72.94 | **70.68** | 3.16 |
| | 3.33 | 65.39 | 68.32 | 67.21 | **66.97** | 2.21 |
| | 2.67 | 60.16 | 65.22 | 63.74 | **63.04** | 4.13 |
| 5mm Hole | 4 | 72.90 | 70.19 | 73.44 | **72.18** | 2.41 |
| | 3.33 | 72.04 | 69.03 | 69.07 | **70.05** | 2.46 |
| | 2.67 | 58.83 | 64.66 | 67.23 | **63.57** | 6.77 |
| 7.5mm Hole | 4 | 46.14 | 37.19 | 33.38 | **38.90** | 16.84 |
| | 3.33 | 66.80 | 63.07 | 55.24 | **61.70** | 9.56 |
| | 2.67 | 34.53 | 60.06 | 34.75 | **43.11** | 34.04 |
| 10mm Hole | 4 | 32.35 | 36.78 | 33.04 | **34.06** | 7.00 |
| | 3.33 | 65.41 | 34.14 | 40.44 | **46.66** | 35.44 |
| | 2.67 | 27.59 | 35.07 | 41.37 | **34.68** | 19.89 |
| 12.5mm Hole | 4 | 27.95 | 35.07 | 28.21 | **30.41** | 13.28 |
| | 3.33 | 26.82 | 37.11 | 36.10 | **33.34** | 17.01 |
| | 2.67 | 23.97 | 24.96 | 32.33 | **27.09** | 16.86 |
| 16mm Hole | 4 | 36.63 | 36.03 | 24.52 | **32.39** | 21.07 |
| | 3.33 | 26.81 | 44.36 | 20.08 | **30.42** | 41.21 |
| | 2.67 | 17.67 | 22.04 | 21.83 | **20.51** | 12.01 |
| 1.5J Impact | 4 | 70.77 | 71.23 | 67.72 | **69.91** | 2.73 |
| | 3.33 | 65.97 | 67.85 | 68.52 | **67.45** | 1.96 |
| | 2.67 | 62.40 | 67.72 | 64.22 | **64.78** | 4.17 |
| 3J Impact | 4 | 71.62 | 67.22 | 71.73 | **70.19** | 3.67 |
| | 3.33 | 34.75 | 66.00 | 67.93 | **56.23** | 33.12 |
| | 2.67 | 20.84 | 60.80 | 60.77 | **47.47** | 48.58 |
| 6J Impact | 4 | 34.13 | 67.03 | 66.10 | **55.75** | 33.60 |
| | 3.33 | 27.06 | 63.96 | 20.70 | **37.24** | 62.72 |
| | 2.67 | 63.81 | 62.89 | 17.06 | **47.92** | 55.78 |
| 9J Impact | 4 | 23.91 | 34.54 | 72.36 | **43.60** | 58.40 |
| | 3.33 | 27.55 | 21.94 | 28.55 | **26.01** | 13.70 |
| | 2.67 | 20.97 | 32.69 | 20.10 | **24.59** | 28.60 |

**Appendix 7-3 – SEAs for the large (89.1mm diameter) CoFRM/Norpol tubes of varying wall thickness and damage type, tested at 5mm/min**
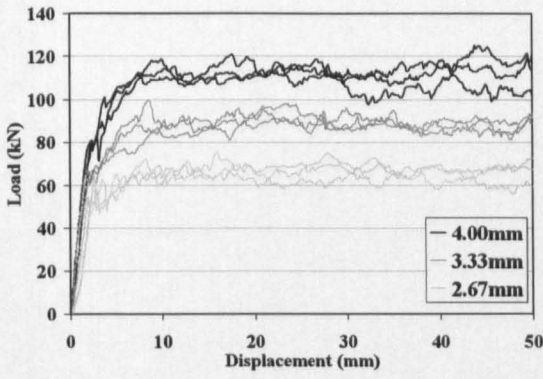
Undamaged
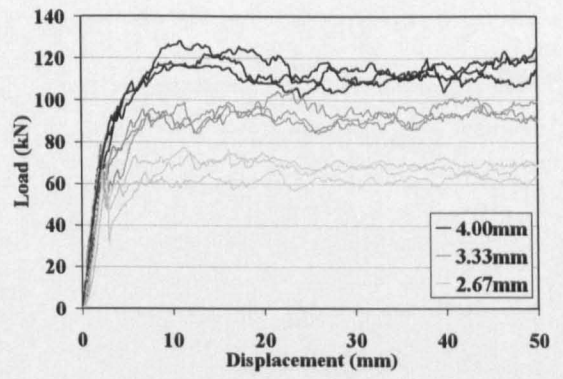

5mm Hole
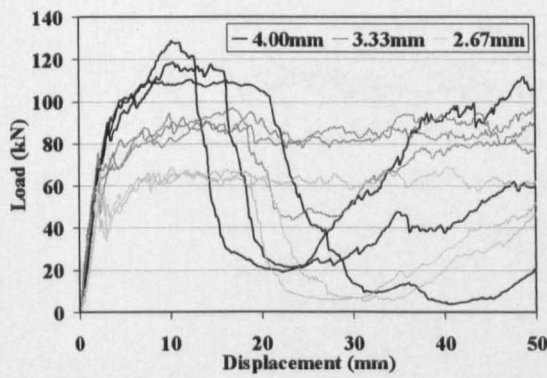

7.5mm Hole
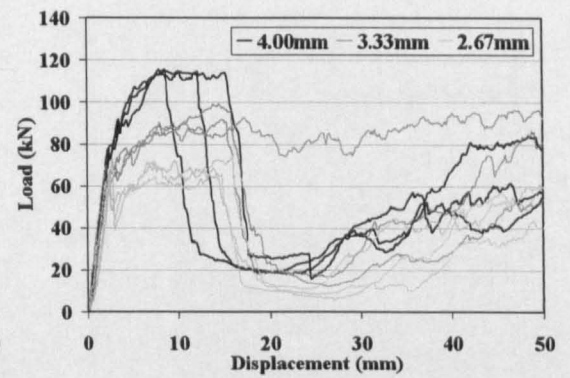

10mm Hole
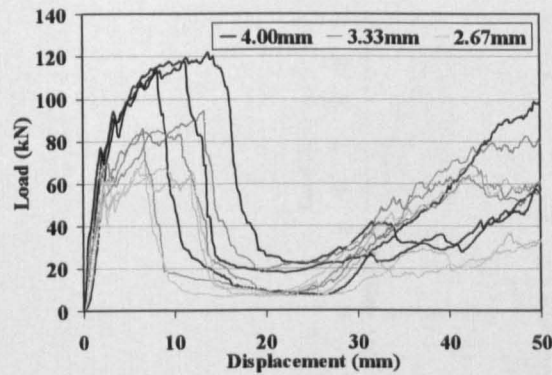

12.5mm Hole
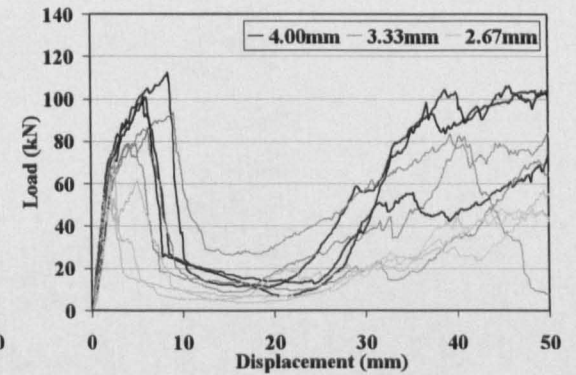

16mm Hole

**Appendix 7-4 – Load-displacement curves for the statically (0.5mm/s) tested large (89.1mm diameter/4mm wall thickness) CoFRM/Norpol tubes containing various hole sizes centred at 30mm from the chamfer (Dimensions on graphs indicate wall thickness)**
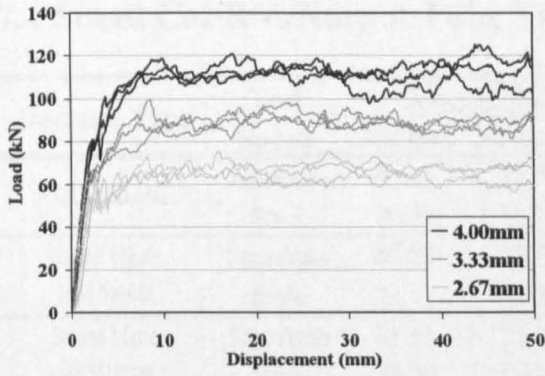
Undamaged
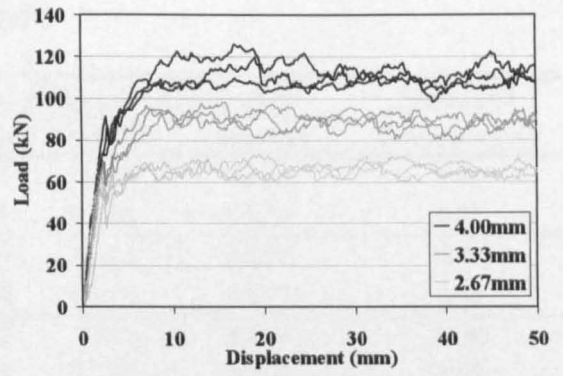


1.5J Impact
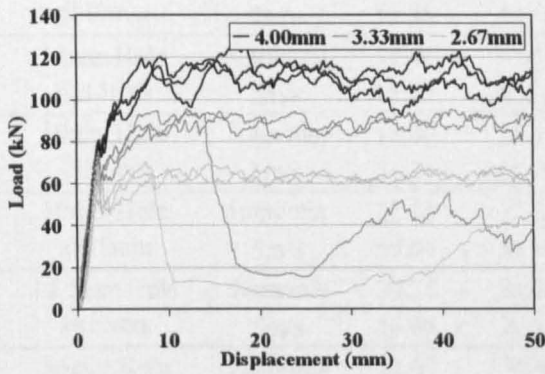


3J Impact
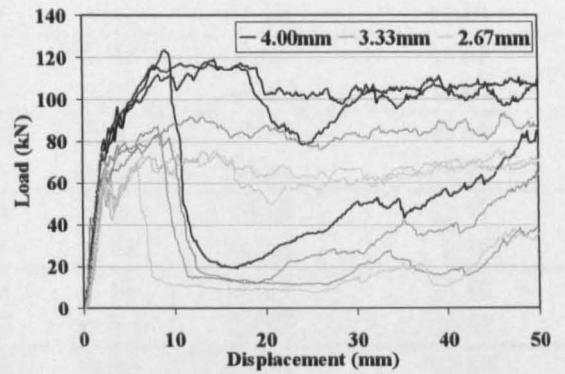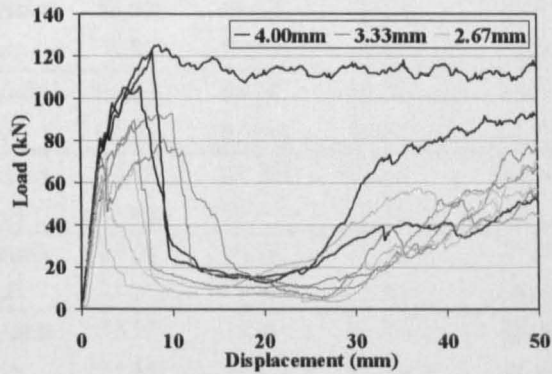


6J Impact
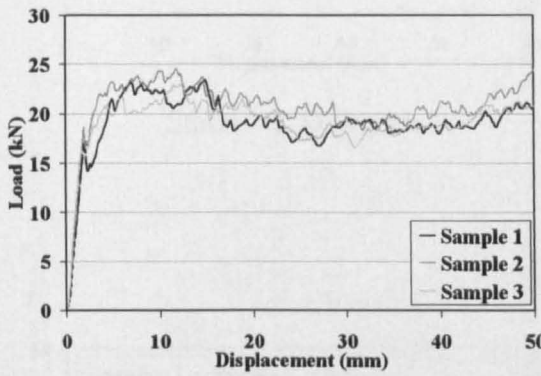


9J Impact

**Appendix 7-5 - Load-displacement curves for the statically (0.5mm/s) tested CoFRM/Norpol large (89.1mm diameter/4mm wall thickness) tubes containing various impacts centred at 30mm from the chamfer (Dimensions on graphs indicate wall thickness)**

## 7.4 Small CoFRM/Norpol Tube Tests

| Damage Type | Test Speed | Specific Energy Absorption (kJ/kg) | | | | Standard Deviation (%) |
|---|---|---|---|---|---|---|
| | | Sample1 | Sample2 | Sample3 | Average | |
| Undamaged | 5mm/min | 72.23 | 73.77 | 77.65 | **74.55** | 3.75 |
| | 5m/s | 70.59 | 65.15 | 67.80 | **67.85** | 4.01 |
| 5mm Hole @15mm | 5mm/min | 57.85 | 74.70 | 67.62 | **66.72** | 12.68 |
| | 5m/s | 71.73 | 64.86 | 63.71 | **66.77** | 6.50 |
| 5mm Hole @30mm | 5mm/min | 31.55 | 71.10 | 72.44 | **58.36** | 39.80 |
| | 5m/s | 59.20 | 58.98 | 61.88 | **60.02** | 2.69 |
| 2x5mm Hole @30mm | 5mm/min | 44.55 | 18.16 | 51.93 | **38.21** | 46.46 |
| | 5m/s | 58.33 | 57.01 | 59.69 | **58.34** | 2.30 |
| 7.5mm Hole @30mm | 5mm/min | 35.28 | 45.31 | 41.41 | **40.67** | 12.42 |
| | 5m/s | 53.95 | 56.55 | 44.84 | **51.78** | 11.88 |
| 10mm Hole @15mm | 5mm/min | 39.46 | 51.60 | 55.04 | **48.70** | 16.81 |
| | 5m/s | 45.95 | 55.37 | 38.05 | **46.46** | 18.66 |
| 10mm Hole @30mm | 5mm/min | 19.80 | 28.14 | 17.98 | **21.97** | 24.65 |
| | 5m/s | 54.21 | 60.06 | 48.72 | **54.33** | 10.44 |
| 10mm Hole @45mm | 5mm/min | 22.24 | 27.31 | 29.24 | **26.26** | 13.77 |
| | 5m/s | 59.04 | 58.96 | 60.96 | **59.65** | 1.90 |
| 12.5mm Hole @30mm | 5mm/min | 30.74 | 22.66 | 23.64 | **25.68** | 17.18 |
| | 5m/s | 16.65 | 20.17 | 23.40 | **20.07** | 16.82 |
| 16mm Hole @30mm | 5mm/min | 13.67 | 35.68 | 17.60 | **22.32** | 52.59 |
| | 5m/s | 16.78 | 15.22 | 25.30 | **19.10** | 28.41 |
| 32mm PET Insert | 5mm/min | 70.81 | 70.81 | 70.38 | **70.67** | 0.35 |
| | 5m/s | 62.74 | 65.63 | 64.94 | **64.44** | 2.34 |
| 2x32mm PET Insert | 5mm/min | 58.62 | 63.12 | 58.22 | **59.99** | 4.54 |
| | 5m/s | 56.01 | 59.47 | 61.63 | **59.04** | 4.80 |
| 50.8mm PET Insert | 5mm/min | 66.82 | 68.38 | 55.70 | **63.63** | 10.87 |
| | 5m/s | 62.81 | 61.00 | 59.68 | **61.16** | 2.57 |
| 1.5J Impact | 5mm/min | 72.12 | 29.28 | 38.10 | **46.50** | 48.65 |
| | 5m/s | 60.61 | 64.72 | 67.51 | **64.28** | 5.40 |
| 3J Impact | 5mm/min | 39.21 | 22.05 | 27.26 | **29.51** | 29.82 |
| | 5m/s | 33.29 | 57.29 | 31.23 | **40.60** | 35.68 |
| 6J Impact | 5mm/min | 32.93 | 28.20 | 26.79 | **29.31** | 10.97 |
| | 5m/s | 31.14 | 28.55 | 34.59 | **31.43** | 9.64 |
| 9J Impact | 5mm/min | 29.81 | 19.42 | 16.46 | **21.90** | 32.02 |
| | 5m/s | 34.70 | 33.99 | 40.40 | **36.36** | 9.66 |

**Appendix 7-6 - SEAs for the small (38.1mm diameter) CoFRM/Norpol tubes containing various damage types**
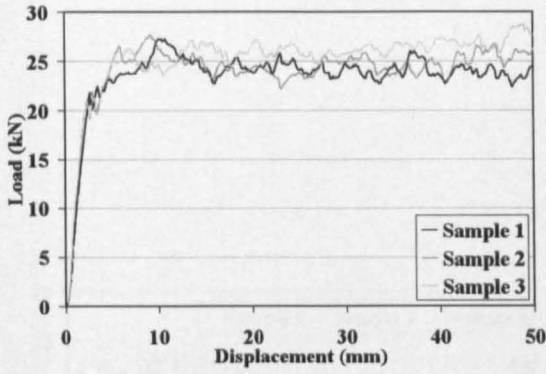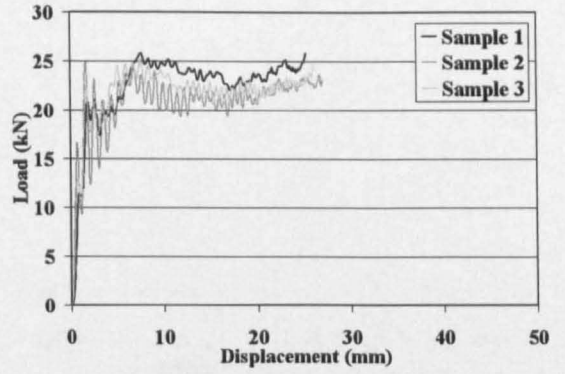
Static – Undamaged



Dynamic - Undamaged
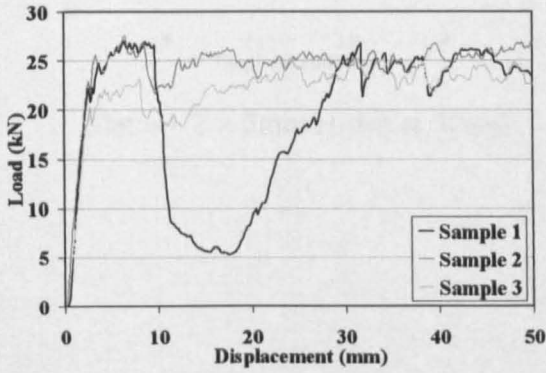


Static – 5mm Hole at 15mm
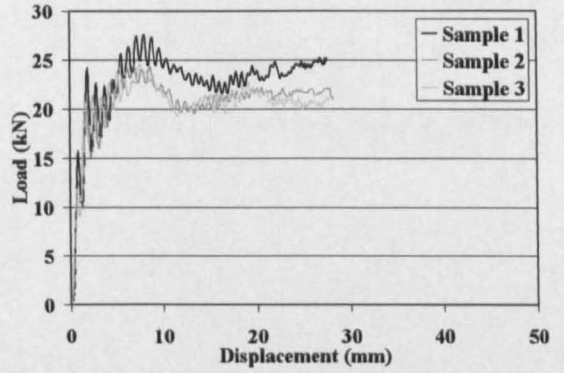


Dynamic – 5mm Hole at 15mm
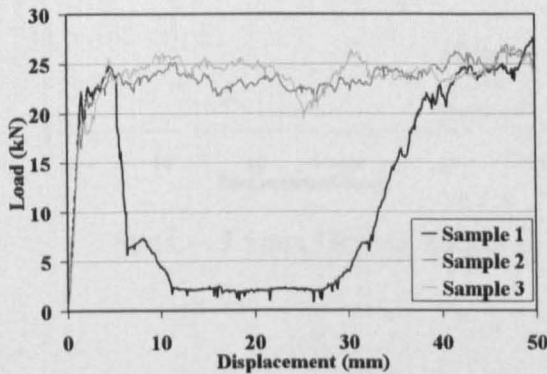


Static – 5mm Hole at 30mm
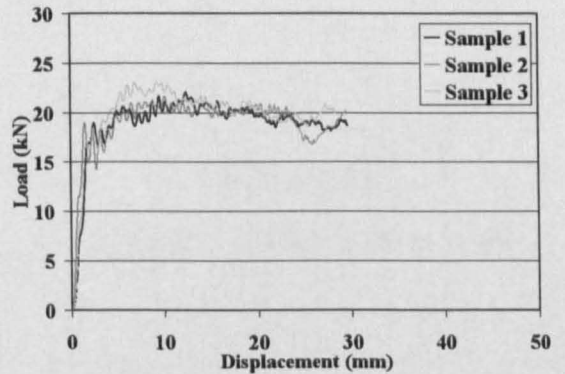


Dynamic – 5mm Hole at 30mm

Appendix 7-7 - Load-displacement curves for the statically (0.5mm/s) and dynamically (5m/s) tested small (38.1mm diameter/2mm wall thickness) CoFRM/Norpol tubes undamaged and containing a 5mm hole centred at 15mm and 30mm from the chamfer
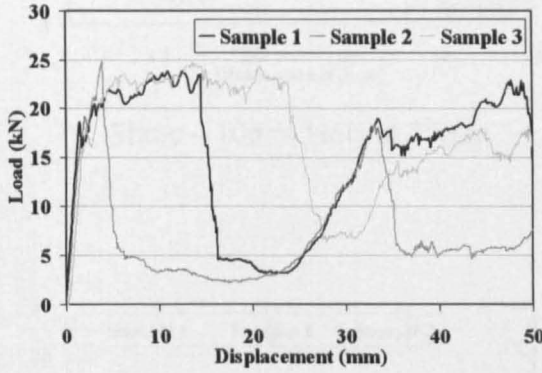
Static – 2 × 5mm Holes at 30mm
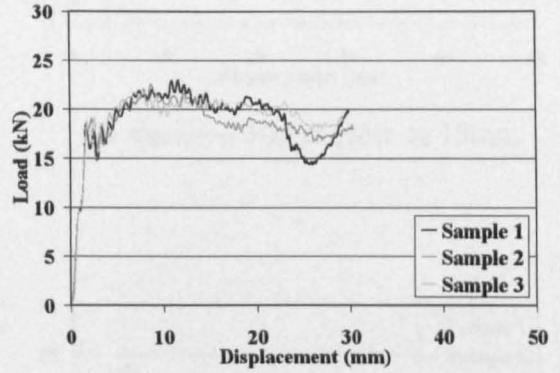
Dynamic – 2 × 5mm Holes at 30mm

Static – 7.5mm Hole at 30mm
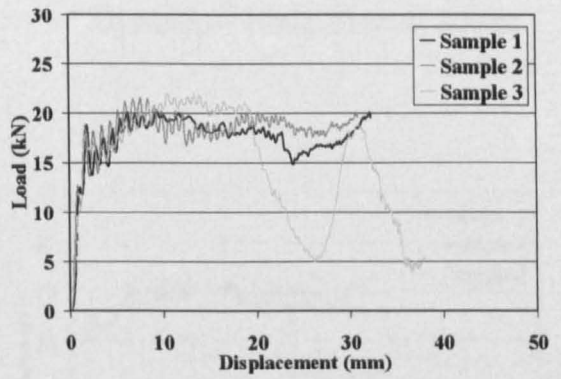
Dynamic – 7.5mm Hole at 30mm

**Appendix 7-8 - Load-displacement curves for the statically (0.5mm/s) and dynamically (5m/s) tested small (38.1mm diameter/2mm wall thickness) CoFRM/Norpol tubes containing holes centred at 30mm from the chamfer**
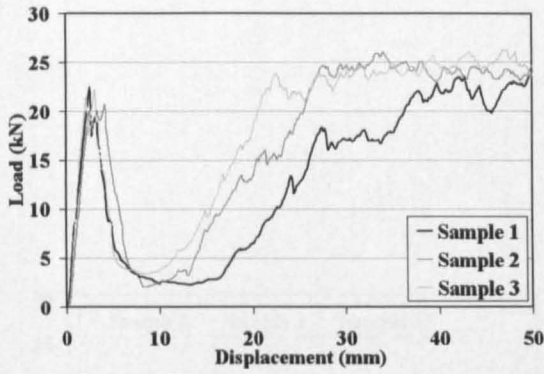
Static – 10mm Hole at 15mm
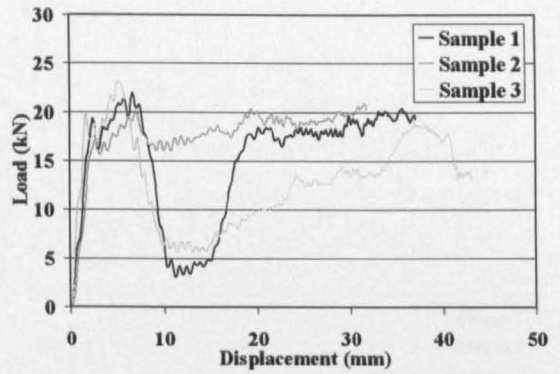


Dynamic – 10mm Hole at 15mm
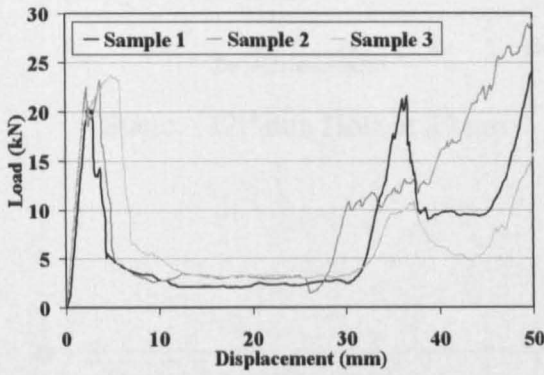


Static – 10mm Hole at 30mm
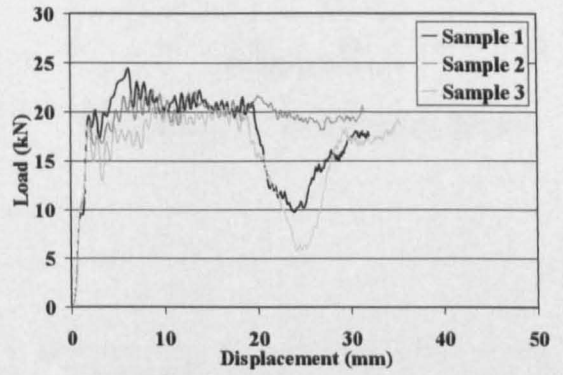


Dynamic – 10mm Hole at 30mm
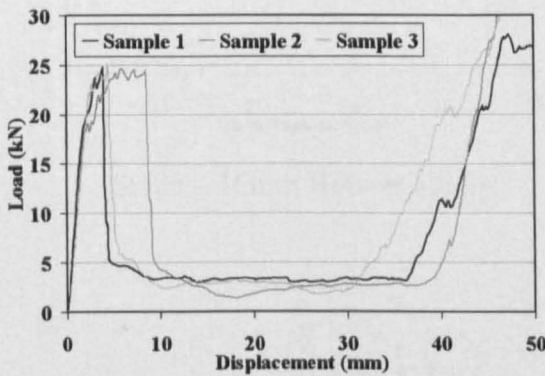


Static – 10mm Hole at 45mm
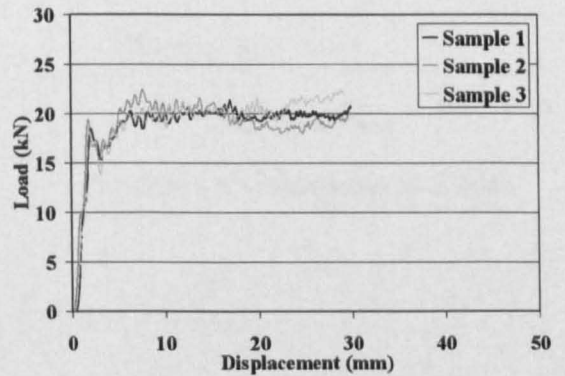


Dynamic – 10mm Hole at 45mm

**Appendix 7-9 - Load-displacement curves for the statically (0.5mm/s) and dynamically (5m/s) tested small (38.1mm diameter/2mm wall thickness) CoFRM/Norpol tubes containing 10mm holes centred various distances from the chamfer**
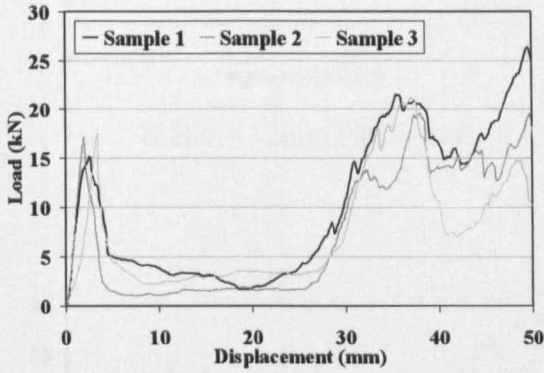
Static – 12.5mm Hole at 30mm
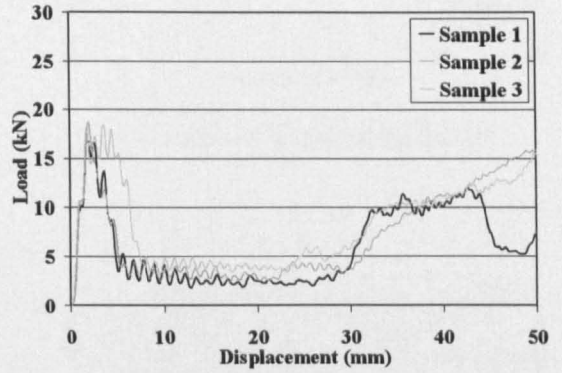


Dynamic – 12.5mm Hole at 30mm
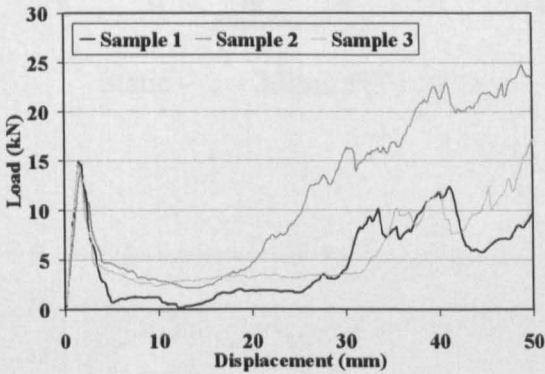


Static – 16mm Hole at 30mm
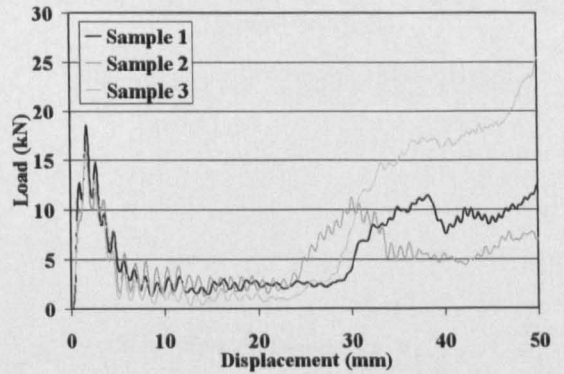


Dynamic – 16mm Hole at 30mm

**Appendix 7-10 - Load-displacement curves for the statically (0.5mm/s) and dynamically (5m/s) tested small (38.1mm diameter/2mm wall thickness) CoFRM/Norpol tubes containing holes centred at 30mm from the chamfer**
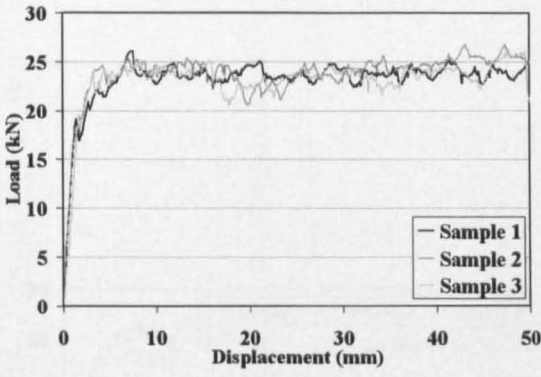
Static – 32mm PET insert
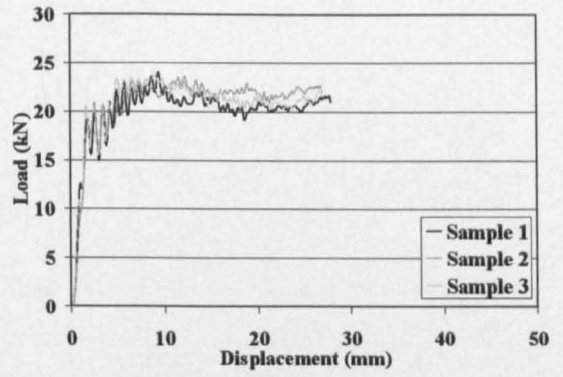


Dynamic – 32mm PET insert



Static – 2 × 32mm PET inserts
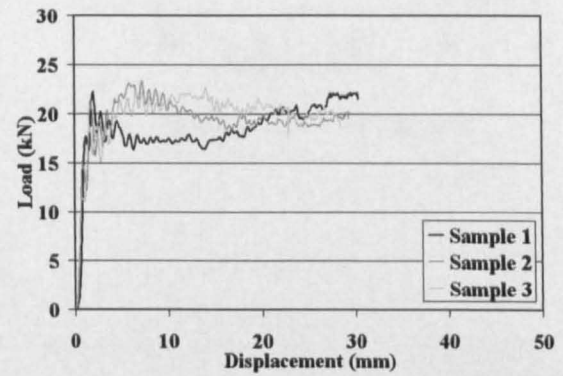


Dynamic – 2 × 32mm PET inserts
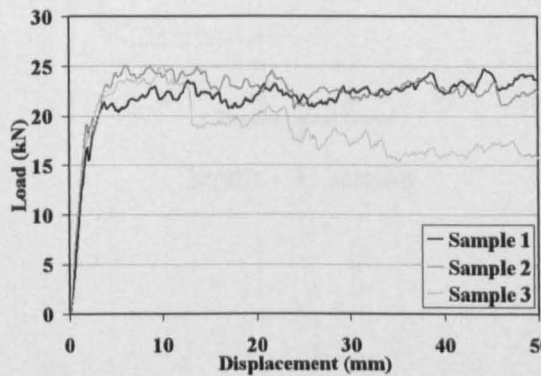


Static – 50mm PET insert
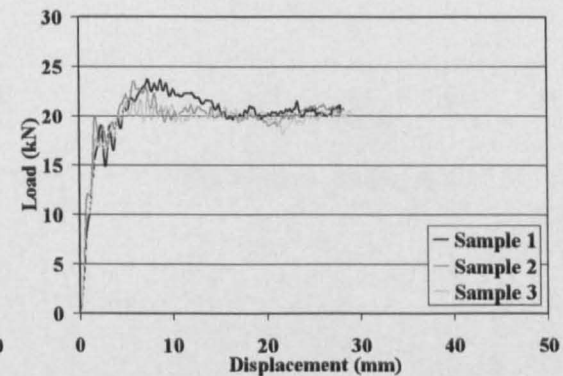


Dynamic – 50mm PET insert

Appendix 7-11 - Load-displacement curves for the statically (0.5mm/s) and dynamically (5m/s) tested small (38.1mm diameter/2mm wall thickness) CoFRM/Norpol tubes containing PET inserts centred at 30mm from the chamfer
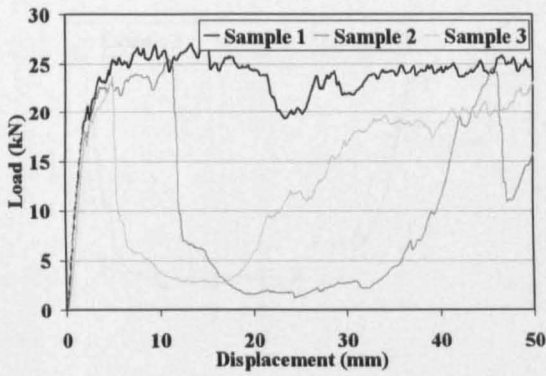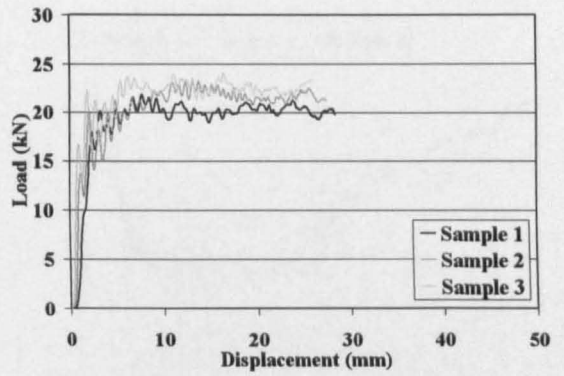
Static – 1.5J impact
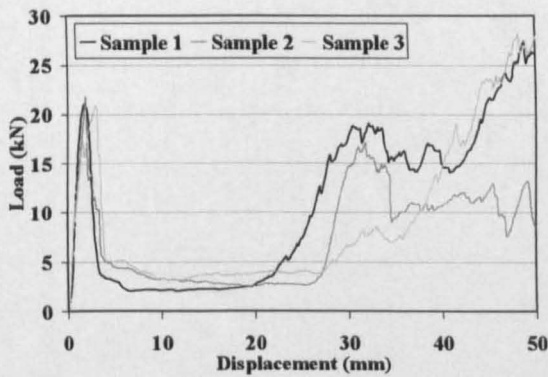


Dynamic – 1.5J Impact
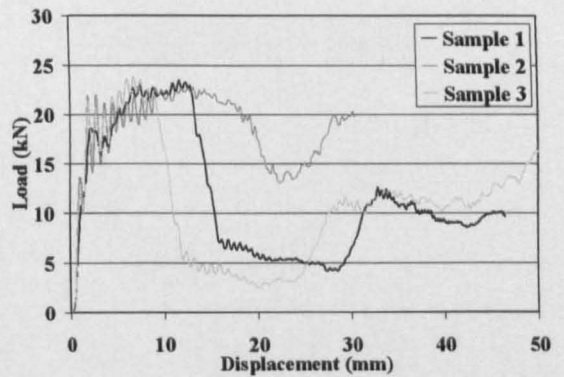


Static – 3J impact



Dynamic – 3J Impact

**Appendix 7-12 - Load-displacement curves for the statically (0.5mm/s) and dynamically (5m/s) tested small (38.1mm diameter/2mm wall thickness) CoFRM/Norpol tubes containing impact damage centred at 30mm from the chamfer**
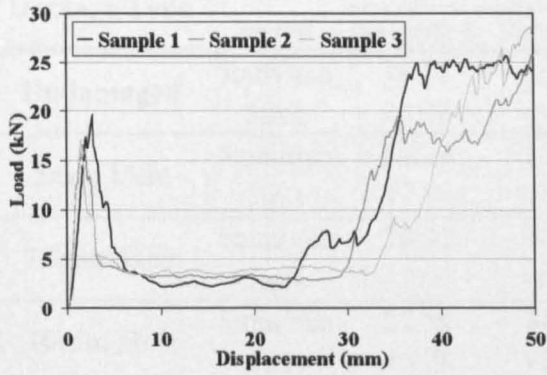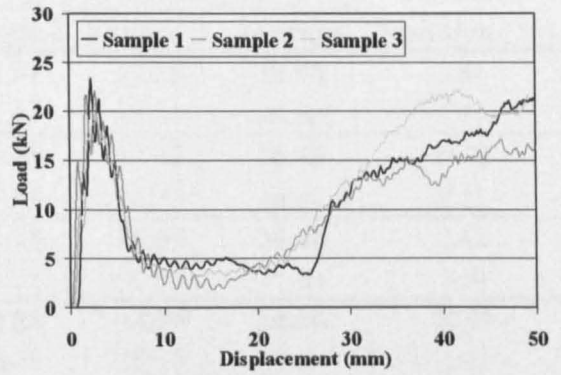
Static – 6J impact
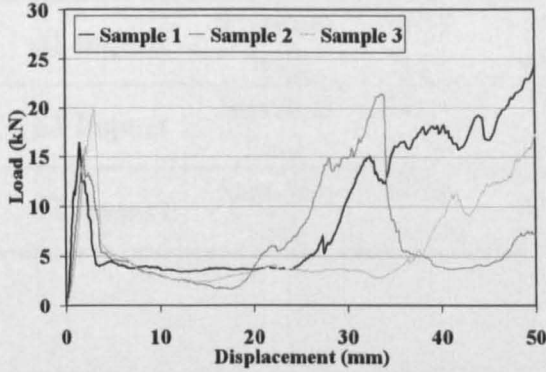


Dynamic – 6J Impact
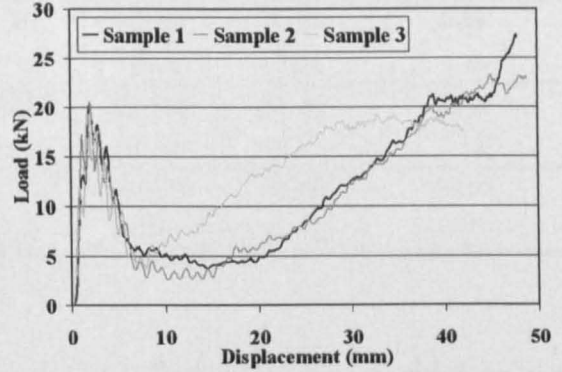


Static – 9J impact



Dynamic – 9J Impact

**Appendix 7-13- Load-displacement curves for the statically (0.5mm/s) and dynamically (5m/s) tested small (38.1mm diameter/2mm wall thickness) CoFRM/Norpol tubes containing impact damage centred at 30mm from the chamfer**

## 7.5 Small Braided/Norpol Tube Tests

| Damage Type | Test Speed | Specific Energy Absorption (kJ/kg) | | | | Standard Deviation (%) |
|---|---|---|---|---|---|---|
| | | Sample 1 | Sample 2 | Sample 3 | Average | |
| Undamaged | 5mm/min | 38.12 | 40.51 | 37.78 | **38.80** | 3.84 |
| | 5m/s | 47.78 | 49.12 | 48.23 | 48.38 | 1.41 |
| 5mm Hole | 5mm/min | 26.29 | 15.53 | 37.62 | **26.48** | 41.72 |
| | 5m/s | 47.56 | 48.44 | 44.75 | 46.92 | 4.11 |
| 7.5mm Hole | 5mm/min | 38.02 | 36.15 | 35.64 | **36.60** | 3.42 |
| | 5m/s | 47.66 | 46.92 | 46.55 | 47.04 | 1.20 |
| 10mm Hole | 5mm/min | 22.59 | 30.88 | 34.59 | **29.35** | 20.93 |
| | 5m/s | 46.78 | 46.79 | 43.65 | 45.74 | 3.96 |
| 12.5mm Hole | 5mm/min | 33.26 | 34.51 | 36.28 | **34.68** | 4.37 |
| | 5m/s | 34.81 | 41.42 | 34.52 | 36.92 | 10.57 |
| 16mm Hole | 5mm/min | 32.23 | 23.04 | 26.59 | **27.29** | 16.99 |
| | 5m/s | 31.65 | 31.95 | 31.18 | 31.59 | 1.23 |
| 1.5J Impact | 5mm/min | 42.75 | 30.17 | 24.86 | **32.59** | 28.18 |
| | 5m/s | 44.05 | 50.63 | 44.69 | 46.46 | 7.81 |
| 3J Impact | 5mm/min | 38.38 | 31.81 | 33.30 | **34.50** | 9.99 |
| | 5m/s | 48.28 | 48.53 | 46.78 | 47.86 | 1.98 |
| 6J Impact | 5mm/min | 29.14 | 23.39 | 29.94 | **27.49** | 12.99 |
| | 5m/s | 42.36 | 35.69 | 38.74 | 38.93 | 8.58 |
| 9J Impact | 5mm/min | 37.36 | 22.94 | 23.70 | **28.00** | 28.99 |
| | 5m/s | 31.09 | 42.08 | 44.85 | 39.34 | 18.50 |

Appendix 7-14 - SEAs for the small (38.1mm diameter) braided/Norpol tubes containing various damage types
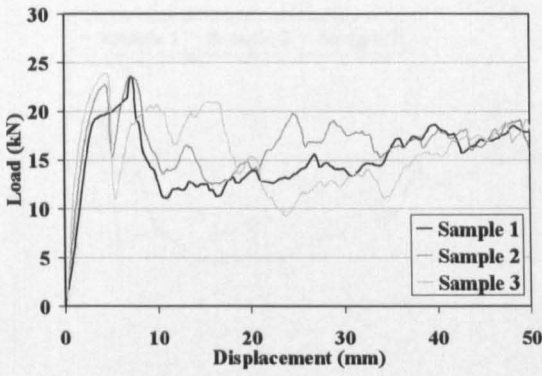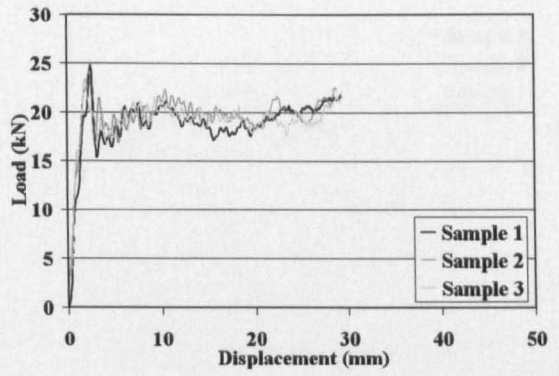
Static – Undamaged



Dynamic - Undamaged
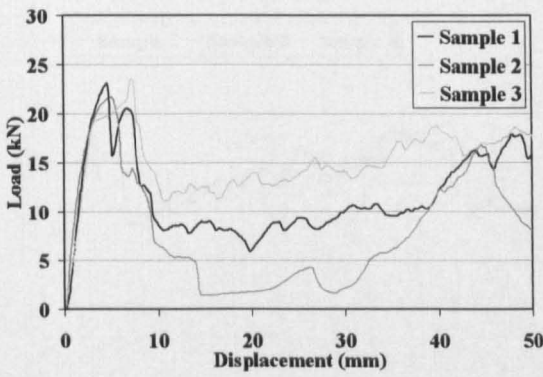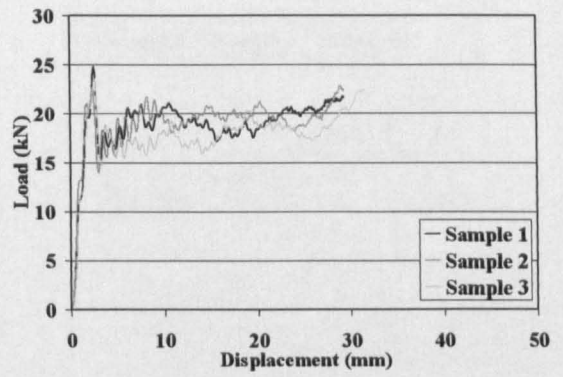
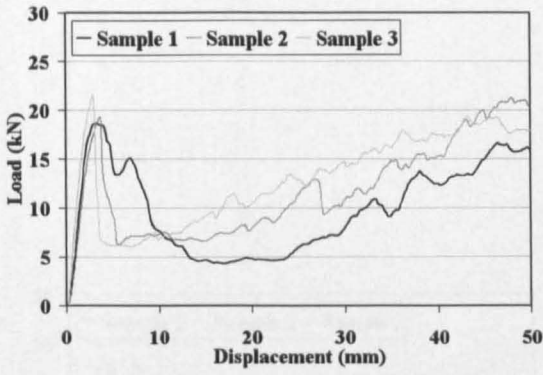

Static – 5mm Hole



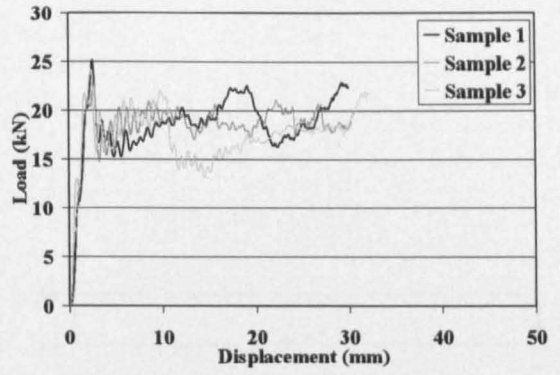Dynamic – 5mm Hole
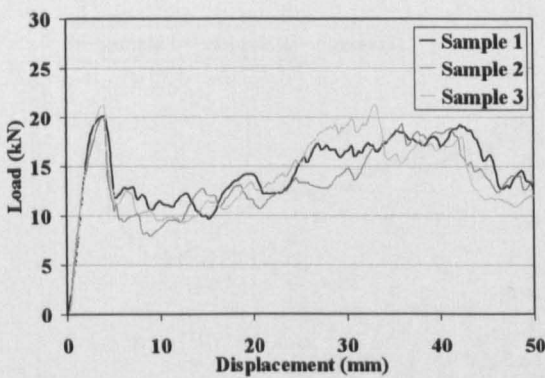


Static – 7.5mm Hole
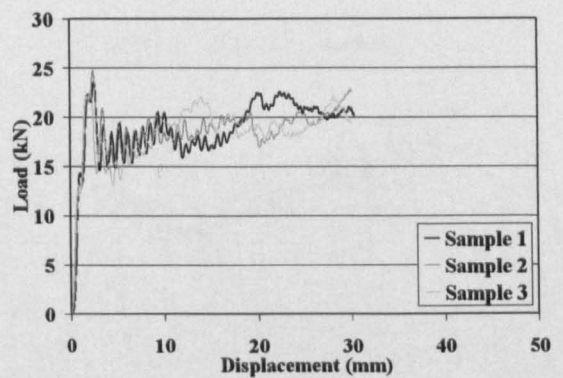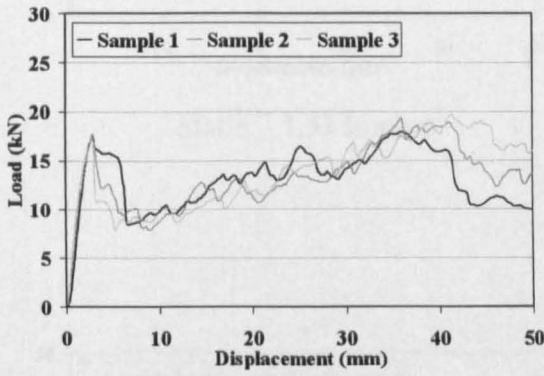


Dynamic – 7.5mm Hole

**Appendix 7-15 - Load-displacement curves for the statically (0.5mm/s) and dynamically (5m/s) tested Braided/Norpol small (38.1mm diameter/2mm wall thickness) tubes containing holes centred at 30mm from the chamfer**
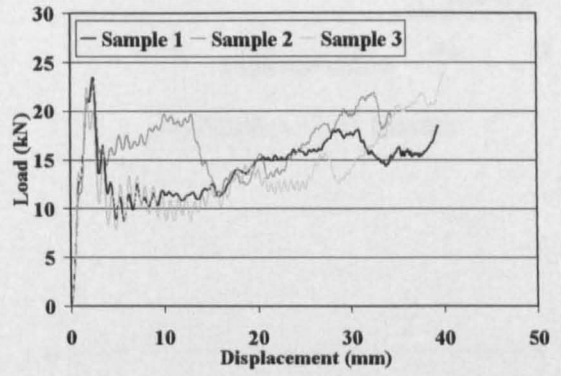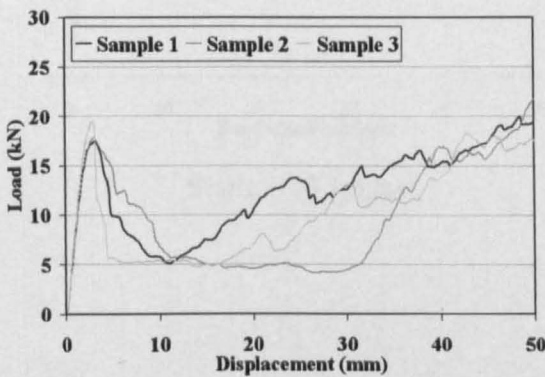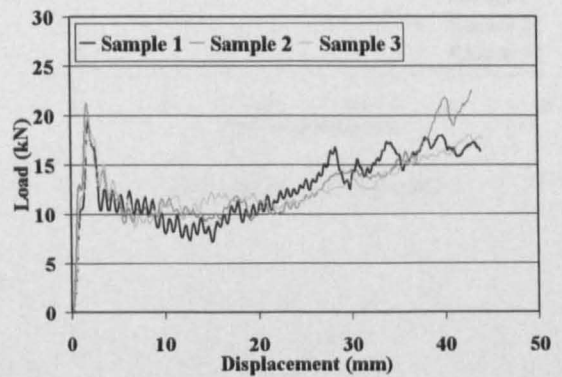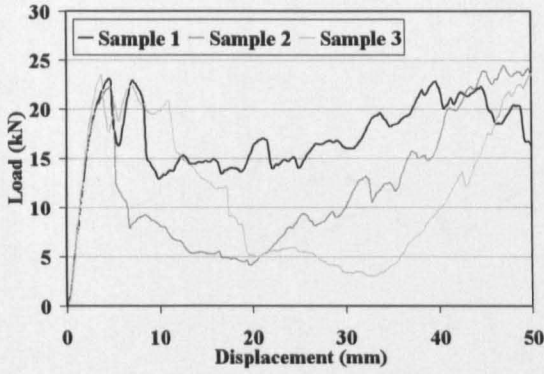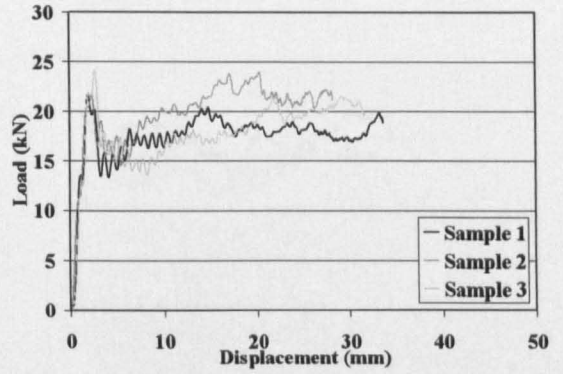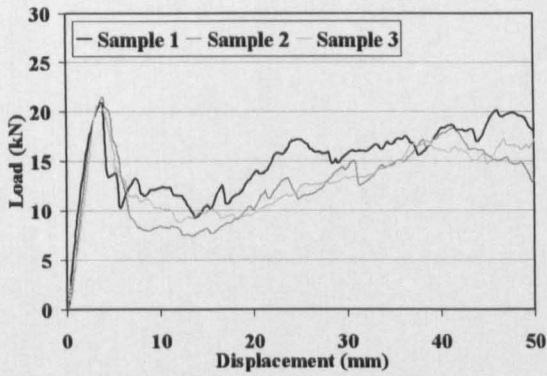
Static – 10mm Hole



Dynamic – 10mm Hole



Static – 12.5mm Hole



Dynamic – 12.5mm Hole



Static – 16mm Hole



Dynamic – 16mm Hole

**Appendix 7-16 - Load-displacement curves for the statically (0.5mm/s) and dynamically (5m/s) tested Braided/Norpol small (38.1mm diameter/2mm wall thickness) tubes containing holes centred at 30mm from the chamfer**
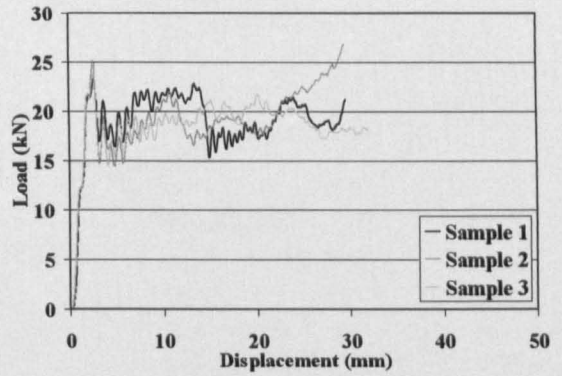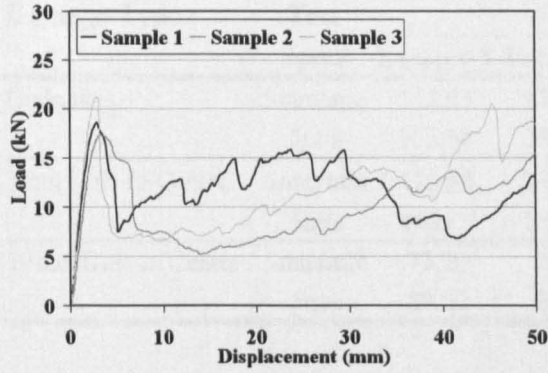
Static – 1.5J Impact
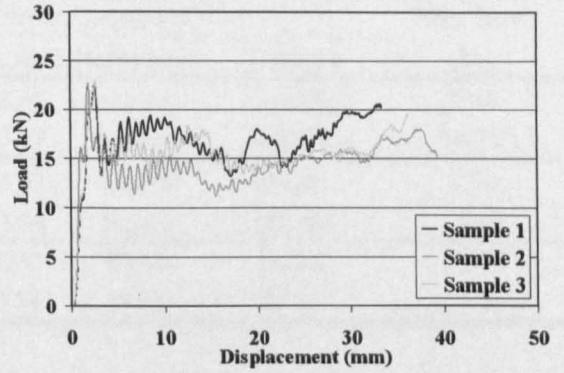


Dynamic – 1.5J Impact



Static – 3J Impact



Dynamic – 3J Impact

**Appendix 7-17 - Load-displacement curves for the statically (0.5mm/s) and dynamically (5m/s) tested Braided/Norpol small (38.1mm diameter/2mm wall thickness) tubes containing impact damage centred at 30mm from the chamfer**

Static – 6J Impact

Dynamic – 6J Impact



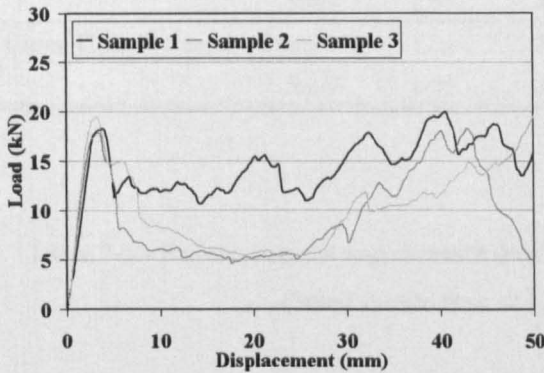Static – 9J Impact

Dynamic – 9J Impact

**Appendix 7-18 - Load-displacement curves for the statically (0.5mm/s) and dynamically (5m/s) tested Braided/Norpol small (38.1mm diameter/2mm wall thickness) tubes containing impact damage centred at 30mm from the chamfer**
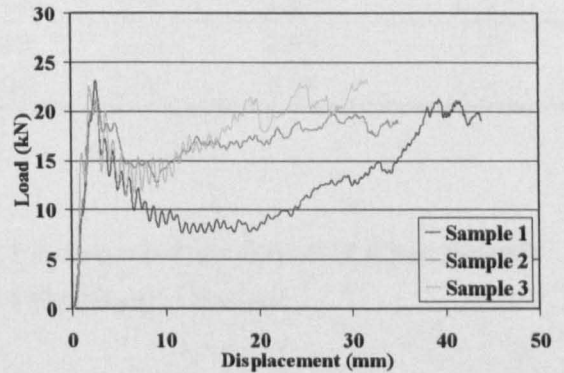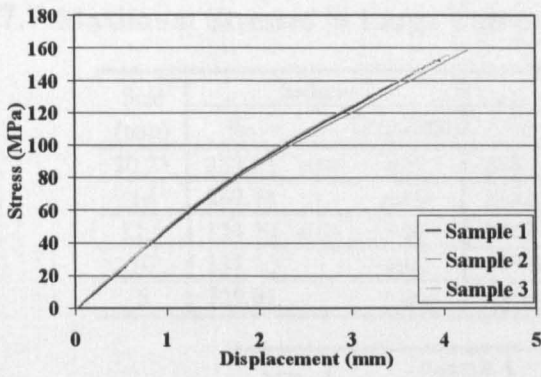
## 7.6 Tensile Coupon Tests

Tensile Coupon Tests - Failure Loads

| Damage Type | Test | Failure Load (kN) | | | | Std. Dev. |
|---|---|---|---|---|---|---|
| | Speed | Sample 1 | Sample 2 | Sample 3 | Average | (%) |
| Undamaged | 5mm/min | 152.05 | 178.68 | 152.55 | **161.09** | 9.45 |
| | 5m/s | 322.65 | 393.49 | 375.24 | **363.79** | 10.11 |
| 5mm Hole In Centre | 5mm/min | 115.68 | 131.82 | 116.44 | **121.31** | 7.51 |
| | 5m/s | 165.67 | 223.94 | 186.23 | **191.95** | 15.40 |
| 10mm Hole in Centre | 5mm/min | 73.20 | 93.00 | 87.80 | **84.67** | 12.13 |
| | 5m/s | 89.09 | 78.34 | 68.40 | **78.61** | 13.16 |

Tensile Coupon Tests - Failure Displacements

| Damage Type | Test | Failure Displacement (mm) | | | | Std. Dev. |
|---|---|---|---|---|---|---|
| | Speed | Sample 1 | Sample 2 | Sample 3 | Average | (%) |
| Undamaged | 5mm/min | 3.96 | 4.27 | 4.07 | **4.10** | 3.83 |
| | 5m/s | 3.46 | 4.20 | 4.19 | **3.95** | 10.74 |
| 5mm Hole In Centre | 5mm/min | 2.88 | 3.05 | 2.70 | **2.88** | 6.08 |
| | 5m/s | 2.98 | 3.00 | 3.00 | **2.99** | 0.39 |
| 10mm Hole in Centre | 5mm/min | 1.74 | 2.23 | 2.13 | **2.03** | 12.73 |
| | 5m/s | 1.99 | 2.25 | 2.00 | **2.08** | 7.08 |

**Table 7-1 - Failure stresses and displacements for the quasi-static (0.5mm/min) and dynamic (5m/s) tensile tests of CoFRM/Polyester coupons**
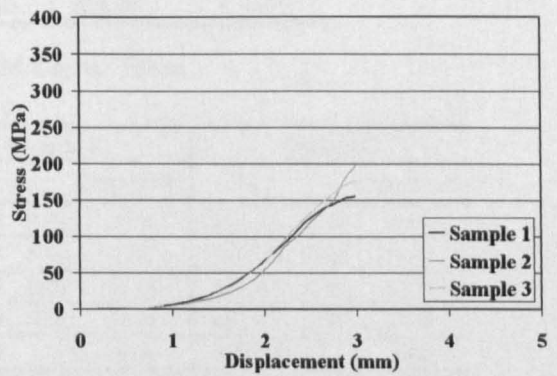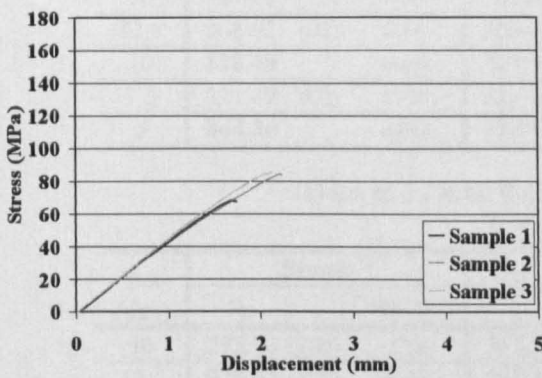
Static - Undamaged
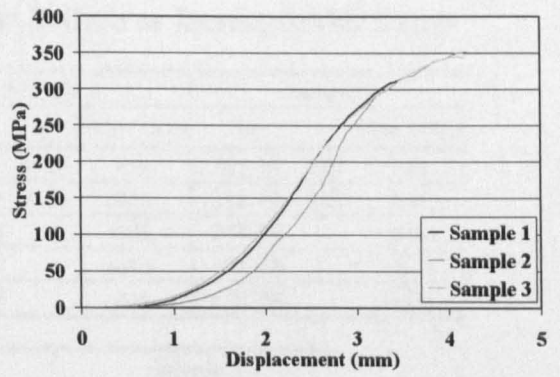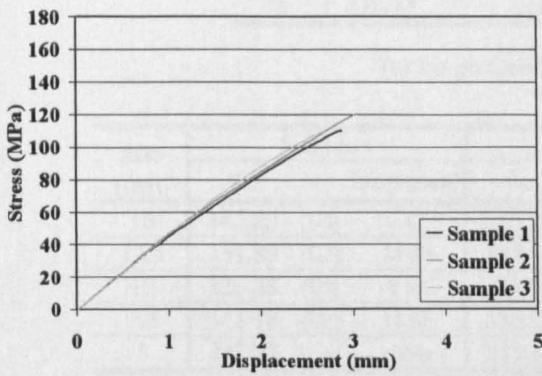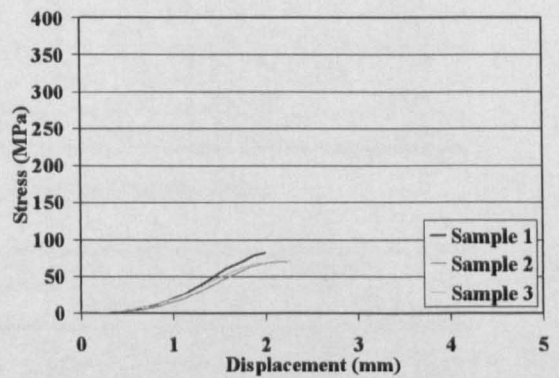
Dynamic – Undamaged

Static – 5mm Drilled Hole

Dynamic – 5mm Drilled Hole

Static – 10mm Drilled Hole

Dynamic – 10mm Drilled Hole

**Appendix 7-19 – Stress-displacement curves for the static (0.5mm/s) and dynamic (5m/s) tensile coupon tests of undamaged CoFRM/polyester specimens and those containing 5mm and 10mm drilled holes**

## 7.7 Maximum Stresses in Large Tubes at Failure or During Stable Crush

| Size | Sample 1 | | Sample 2 | | Sample 3 | |
|---|---|---|---|---|---|---|
| (mm) | $\sigma_m$ | Disp.(mm) | $\sigma_m$ | Disp.(mm) | $\sigma_m$ | Disp.(mm) |
| 20.25 | 263.21 (U2) | 4.47 | 254.71 (U2) | 4.84 | 251.50 (U2) | 3.66 |
| 16 | **267.71** | stable | 234.34 (U2) | 6.01 | 228.43 (U2) | 5.63 |
| 12.5 | 324.20 (U2) | 9.20 | **250.93** | stable | **273.98** | stable |
| 10 | 331.20 | stable | **308.92** | stable | **311.94** | stable |
| 5 | **329.01** | stable | **314.65** | stable | **322.95** | stable |

| Size | Sample 4 | | Sample 5 | |
|---|---|---|---|---|
| (mm) | $\sigma_m$ | Disp.(mm) | $\sigma_m$ | Disp.(mm) |
| 20.25 | 244.13 (U2) | 4.22 | 240.62 (U2) | 4.93 |
| 16 | 264.89 (U2) | 6.93 | **307.95** | stable |
| 12.5 | 270.05 (U2) | 7.84 | **271.40** | stable |
| 10 | 315.15 (U2) | 12.64 | 251.94 (U2) | 11.00 |
| 5 | **332.33** | stable | **354.09** | stable |

(a) Large CoFRM/Crystic Tubes

| Size | Sample 1 | | Sample 2 | | Sample 3 | |
|---|---|---|---|---|---|---|
| (mm) | $\sigma_m$ | Disp.(mm) | $\sigma_m$ | Disp.(mm) | $\sigma_m$ | Disp.(mm) |
| 16 | 347.89 (U2) | 8.47 | 316.96 (U2) | 5.78 | 311.61 (U2) | 6.14 |
| 12.5 | 351.89 (U2) | 14.30 | 337.14 (U2) | 7.97 | 344.09 (U2) | 11.30 |
| 10 | 326.83 (U2) | 8.63 | 324.13 (U2) | 15.14 | 325.43 (U2) | 12.14 |
| 7.5 | 315.18 (U2) | 15.81 | 336.99 (U2) | 12.64 | 295.43 (U2) | 19.47 |
| 5 | **347.37** | stable | **341.47** | stable | **319.28** | stable |

(b) Large 4mm walled CoFRM/Norpol Tubes

| Size | Sample 1 | | Sample 2 | | Sample 3 | |
|---|---|---|---|---|---|---|
| (mm) | $\sigma_m$ | Disp.(mm) | $\sigma_m$ | Disp.(mm) | $\sigma_m$ | Disp.(mm) |
| 16 | 327.45 (U2) | 6.30 | 300.87 (U2) | 4.97 | 357.31 (U2) | 9.13 |
| 12.5 | 308.92 (U2) | 6.64 | 305.30 (U2) | 10.80 | 337.50 (U2) | 13.31 |
| 10 | **318.48** | stable | 329.53 (U2) | 15.79 | 312.47 (U2) | 15.30 |
| 7.5 | 321.47 (U2) | 17.29 | **317.12** | stable | **302.88** | stable |
| 5 | **344.36** | stable | **317.03** | stable | **316.57** | stable |

(c) Large 3.33mm walled CoFRM/Norpol Tubes

| Size | Sample 1 | | Sample 2 | | Sample 3 | |
|---|---|---|---|---|---|---|
| (mm) | $\sigma_m$ | Disp.(mm) | $\sigma_m$ | Disp.(mm) | $\sigma_m$ | Disp.(mm) |
| 16 | 293.73 (U2) | 2.14 | 357.22 (U2) | 2.65 | 233.71 (U2) | 2.15 |
| 12.5 | 324.61 (U2) | 6.64 | 298.43 (U2) | 12.13 | 296.19 (U2) | 11.80 |
| 10 | 287.22 (U2) | 14.80 | 296.76 (U2) | 13.97 | 323.61 (U2) | 15.97 |
| 7.5 | 271.18 (U2) | 20.15 | 278.35 | stable | 278.90 (U2) | 18.64 |
| 5 | **312.62** | stable | **284.99** | stable | **317.91** | stable |

(d) Large 2.67mm walled CoFRM/Norpol Tubes

**(U2) - Unstable failure occurred after crush zone formed**

**Table 7-2 – Maximum Stresses (MPa) in the large (89.1mm diameter) tubes containing holes**